1-1-2013

Environmental Effects on Mechanical and Thermal Behaviors of Zinc Oxide Nanobelts and Dispersion of Carbon Nanostructures

Yingchao Yang
University of South Carolina - Columbia

Recommended Citation

Yang, Y.(2013). *Environmental Effects on Mechanical and Thermal Behaviors of Zinc Oxide Nanobelts and Dispersion of Carbon Nanostructures.* (Doctoral dissertation). Retrieved from http://scholarcommons.sc.edu/etd/2563

ENVIRONMENTAL EFFECTS ON MECHANICAL AND THERMAL BEHAVIORS OF
ZINC OXIDE NANOBELTS AND DISPERSION OF CARBON NANOSTRUCTURES

by

Yingchao Yang

Bachelor of Materials Science and Engineering
Wuhan University of Science and Technology, 2004

Master of Materials Science and Engineering
Harbin Institute of Technology, 2006

_____

Submitted in Partial Fulfillment of the Requirements

For the Degree of Doctor of Philosophy in

Mechanical Engineering

College of Engineering and Computing

University of South Carolina

2013

Accepted by:

Xiaodong (Chris) Li, Major Professor

Djamel Kaoumi, Committee Member

Kevin Huang, Committee Member

Xiao-Dong Zhou, Committee Member

Lacy Ford, Vice Provost and Dean of Graduate Studies

DEDICATION

To my loved wife Ning and daughter Sarah

ABSTRACT

One-dimensional (1-D) nanostructures, such as nanowires, nanobelts, and nanotubes of different materials, have significant applications as nanoscale interconnects and active/functional components of electronic and optoelectronic devices, sensors, actuators, nanoelectromechanical systems (NEMS), and energy generation/conversion systems. The thermal and mechanical stabilities of those nanodevices and nanoenabled energy systems have both theoretical and practical interests. Thermodynamic properties of nanomaterials differ from those of bulk materials. As the size of a solid particle reduces to the nanometer scale, the surface-to-volume ratio increases and the melting temperature may remarkably decrease. The functionality and/or reliability of those nanodevices and nanoenabled energy systems are also determined by the elastic properties of individual 1-D nanostructures. When the environment changes, such as, humidity level, temperature, ultraviolet radiation, the mechanical behaviors of nanomaterials could simultaneously change as well. However, the mechanisms for how the mechanical and thermal behaviors of 1-D nanostructures depend on their surface conditions, size and surface structures are barely understood. ZnO nanostructure, one of the spotlights of current nanoscience and nanotechnology, will be employed to study the environmental effects on the thermal and mechanical behaviors of nanomaterials, respectively.

The exceptional mechanical, superior thermal and electrical properties of carbon nanotubes (CNTs) and graphene make them promising for many engineering

applications, such as composite reinforcements, scanning probe tips, field emission

sources, hydrogen storage systems, super-capacitors, quantum devices, and biosensors. A

significant challenge for both fundamental research and practical applications of CNTs

and graphene is to disperse CNTs and graphene sheets into certain media, such as

ethanol, water, or polymers. Because CNTs and graphene are insoluble and tend to form

bundles due to their strong hydrophobicity and van der Waals attractions, considerable

effort has been invested to develop efficient and low-cost approaches to realize full

dispersion of CNTs and graphene sheets. The environmental effect on dispersion of

CNTs and graphene sheets will also be discussed.

TABLE OF CONTENTS

LIST OF FIGURES

LIST OF SYMBOLS

b Width of nanobelt

c Speed of light

d Displacement

d_c Deflection of cantilever

d_n Deflection of a nanostructure

d_t Total deflection

f Frequency of electromagnetic wave

h Height of nanobelt

$\hbar$ Reduced Plank constant

k_n Spring constant of a nanostructure

l_f Length of graphene sheet

n Number of graphene layers

r Radius of nanowire

s Slope of the energy-atom distance curve

t_f Thickness of graphene sheet

α_f Aspect ratio of graphene sheet

σ_f Fracture strength

ω_G G band Raman shift

λ de Broglie Wavelength

Δx Atom distance change

Δy	Atom energy change
Ω	Tilt angle
A_B	Corss-sectional areas of bulk
A_S	Corss-sectional areas of surface
A_{Tot}	Corss-sectional areas of a nanostructure
E	Elastic modulus
E_c	Predicted elastic modulus of composite
E_e	Energy of a charged atomic oscillator
E_f	Elastic modulus of fiber
E_m	Elastic modulus of matrix
E_n	Elastic modulus of nanobelt
F	Applied load
G	Gibbs free energy
I	Moment of inertia
L	Suspended length of nanobelt
P	Pressure
S	System entropy
T	Absolute temperature
T_b	Bulk melting point
T_s	Shell melting point
U	Internal energy
V	System volume
V_f	Volume fraction of fiber

W_f Fracture energy

Y_B Elastic modulus of bulk

Y_N Elastic modulus of nanostructure

Y_S Elastic modulus of surface

LIST OF ABBREVIATIONS

1-D .... One Dimensional

2-D ....Two Dimensional

3-D ....Three Dimensional

CNTs..Carbon Nanotubes

VLS ....Vapor-Liquid-Solid

VPT .... Vapor-Phase Transport

UV .... Ultraviolet

EBI ....Electron Beam Irradiation

EBID .... Electron Beam Induced Deposition

ZTO...Zinc Tin Oxide

NPH...Isobaric-Isoenthalpic

MWCNTs...Multi-Walled Carbon Nanotubes

NEMS .... Nanoelectromechanical Systems

DFT ....First Principles Density Functional Theory

SEM ....Scanning Electron Microscopy

EDX .... Energy Dispersive X-Ray

TEM .... Transmission Electron Microscopy

HRTEM..High-Resolution Transmission Electron Microscopy

AFM... Atomic Force Microscopy

FFT.. Fast Fourier Transform

RH...Relative Humidity

CHAPTER 1

INTRODUCTION

One-dimensional (1-D) nanostructures have attracted a great deal of research interest in recent years, because of their importance in fundamental low-dimensional physics research as well as in technological application.[1-4] ZnO nanostructures have been the research focus as functional and structural nanobuilding blocks in nanoelectronics and nanooptoelectronic devices in last decade.[5-8] The exceptional mechanical, superior thermal and electrical properties of carbon nanotubes (CNTs) and graphene have made them promising for many engineering applications, such as composite reinforcements.[9-11] This section will address the synthesis, mechanical and thermal stabilities of ZnO nanostructures, dispersion of CNTs and graphene sheets, and nanocomposites reinforced by CNTs and graphene.

1.1 Synthesis and Mechanical Properties of ZnO Nanostructures

1.1.1 Synthesis of ZnO Nanostructures

Wurtzite zinc oxide has a hexagonal structure (space group C6mc) with lattice parameters a=0.3296 and c=0.5265 nm. The structure of ZnO can be described as a number of alternating planes composed of tetrahedral coordinated O^{2-} and Zn^{2+} ions, stacked alternately along the c-axis.[12] The three most commonly observed faces for ZnO are $\{2\bar{1}\bar{1}0\}$ and $\{01\bar{1}0\}$, and $\{0001\}$. $\{0001\}$ is a polar surface, which is at forefront of

research in surface physics. $\{2\bar{1}\bar{1}0\}$ and $\{01\bar{1}0\}$ are non-polar surfaces and have lower energy compared to $\{0001\}$ faces.[13] An assortment of ZnO nanostructures, such as nanobelts, nanowires, nanotubes, nanorods, nanorings etc. have been grown via a variety of methods including chemical vapor deposition, thermal evaporation, hydrothermal, and electrodeposition.
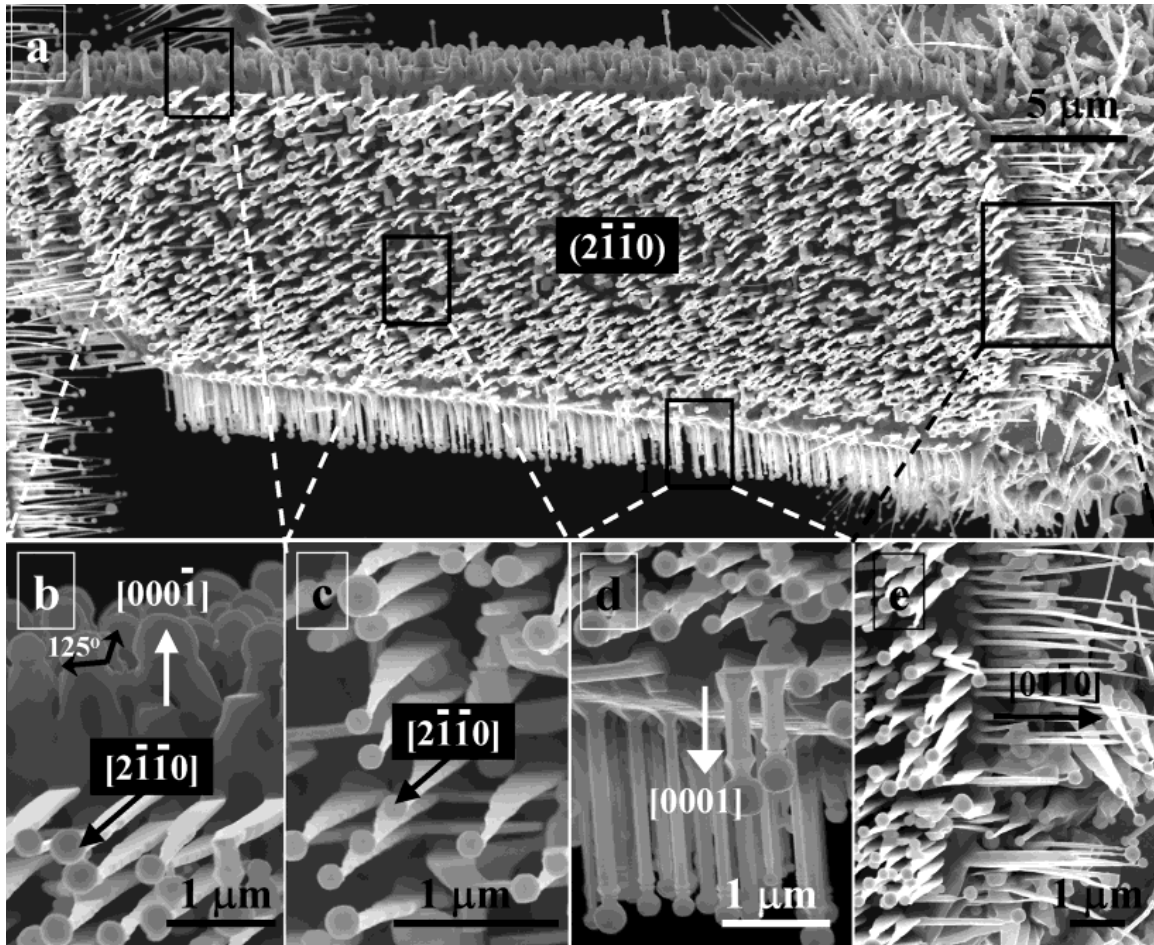
Figure 1.1 SEM images of the as-synthesized ZnO nanostructures growing out of the five surface of a ZnO substrate. (reprinted from Gao *et al*. *J. Phys. Chem. B* **2004**, *108*, 7534-7537)[14]

The vapor-liquid-solid method (VLS), one of chemical vapor deposition methods, is a mechanism for the growth of one-dimensional nanostructures. The growth of crystals through direct adsorption of a gas phase on to a solid surface is generally very slow. The

VLS mechanism can overcome the low-efficiency crystal growth by introducing a catalytic liquid alloy phase that can rapidly adsorb a vapor to supersaturation levels. Crystal growth can subsequently occur from nucleated seeds at the liquid-solid interface. The physical characteristics of nanowires grown in this manner depend upon the size and physical properties of the liquid alloy. This technique becomes a common technique for nanostructure fabrication, particularly for oxide materials. For ZnO nanostructures, different kinds of catalysts have been used to synthesize ZnO nanowires and nanorods, such as Au,[15-19] Cu,[20] Sn,[14,21] Zn,[22] and SnO_2[23] etc. Figure 1.1 shows SEM images of the as-synthesized ZnO nanostructures growing out of the five surfaces of a ZnO substrate using Sn as catalyst.
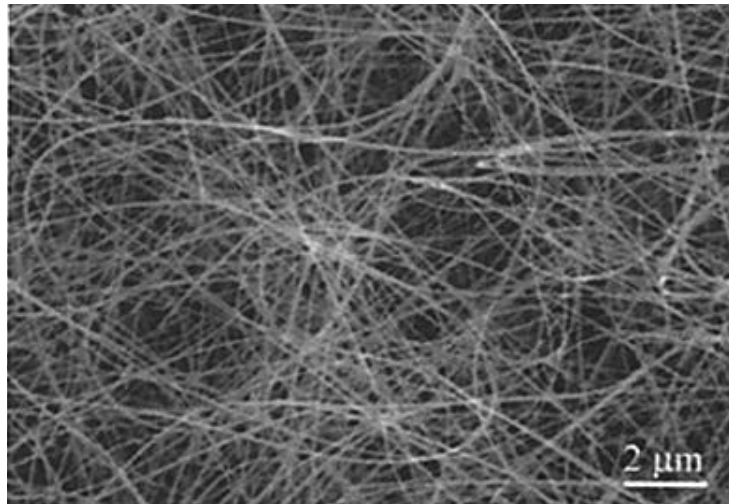
Figure 1.2 Ultralong nanobelt structure of ZnO. (reprinted from Pan *et al*. *Science*, **2001**, *291*, 1947-1949)[24]

The vapor-solid (VS) method has been employed to synthesize ZnO nanostructures.[25-30] The difference between VLS and VS is that there is no catalyst to assist nanostructure growth for VS. This technique can be carried out in a relatively simple setup composed of a dual-zone or a three-zone vacuum furnace. Most processes

3

put the powder source materials at the hot end of the furnace and vaporize them at high temperature. The resultant vapors condense under certain conditions to form the desired product. Temperature, pressure, carrier gas, substrate and evaporation time period are the most important processing parameters, which need to be selected and controlled before and/or during the thermal vaporization. The thermal evaporation process is also very sensitive to the concentration of oxygen in the growth system. Oxygen influences not only the volatility of the source material and the stoichiometry of the vapor phase, but also the formation of the product.[12] Umar *et al.* used zinc powder and oxygen gas as source materials for zinc and oxygen to achieve a large quantity of ZnO nanorods.[28] The diameter of such nanostructures was between 150-250 nm and the length was up to 10 µm. Zn powder and graphite with a weight ratio of 1:1 have been employed to synthesized ultralong ZnO nanobelts. The ultralong nanobelt structure of ZnO with wurtzite crystal structure is shown in Figure 1.2.
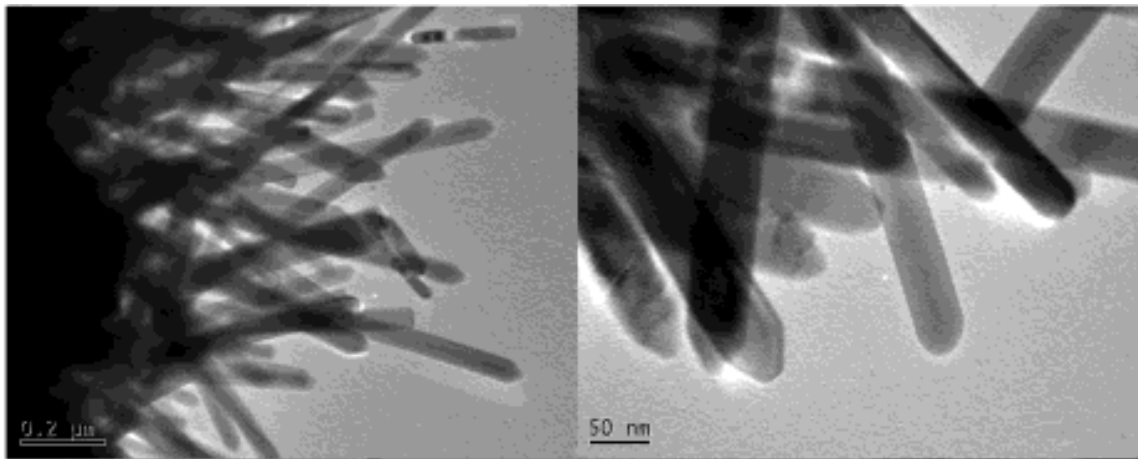
Figure 1.3 TEM images of ZnO nanorods obtained by hydrothermal method. (reprint from Liu *et al*. *J. Am. Chem. Soc.* **2003**, *125*, 4430-4431)[31]

Hydrothermal synthesis is a method of synthesis of single crystals that depends on the solubility of minerals in hot water under high pressure. The crystal growth is

performed in an apparatus consisting of a steel pressure vessel called autoclave, in which source materials are supplied along with water.[32-35] Compared to the facilities used in high-temperature growth techniques such as vapor-liquid-solid (VLS) growth and vapor-phase transport (VPT), the facilities required in the hydrothermal method are cheap and easy to operate. The materials that have a high vapor pressure near their melting points can be grown by the hydrothermal method. The method is also particularly suitable for the growth of large good-quality crystals with desired composition. Several parameters can be controlled during synthesizing ZnO nanostructures, such precursors and temperature, and these significantly influence the final structures. In a typical procedure, a solution of zinc acetate dehydrate in methanol, ethanol, and a solution of sodium hydroxide in methanol, ethanol with different concentrations were prepared first. 10 mL of 0.1 M of zinc acetate stock solution in methanol was mixed with 20 mL of 0.5 M NaOH solution in methanol to produce a clear solution which was transferred to a Teflon-lined stainless steel autoclave and heated at 150 °C for 24 hours.[36] A white precipitate was collected, washed with water and ethanol several times, and dried in air at room temperature. As reported in Figure 1.3, the ZnO nanorods (in 100% morphological yield) were arranged in the form of a bushlike assembly with the well-faced <0001> ends projecting out.[31]

The process used in electroplating is called electrodeposition, in which metal ions in a solution are moved by an electric field to coat an electrode. The anode is made of the metal to be plated onto the part. Both components are immersed in an electrolyte solution containing one or more dissolved metal salts as well as other ions that facilitate the flow of electricity. A power supply supplies a direct current to the anode, oxidizing its metal

atoms and allowing them to dissolve in the solution. The dissolved metal ions are reduced at the interface between the solution and cathode, and they "plate out" onto the cathode. The rate at which the anode is dissolved equals the rate at which the cathode is plated. The process uses electrical current to reduce cations of a desired material from a solution and coat a conductive object with a thin layer of the material, such as a metal.
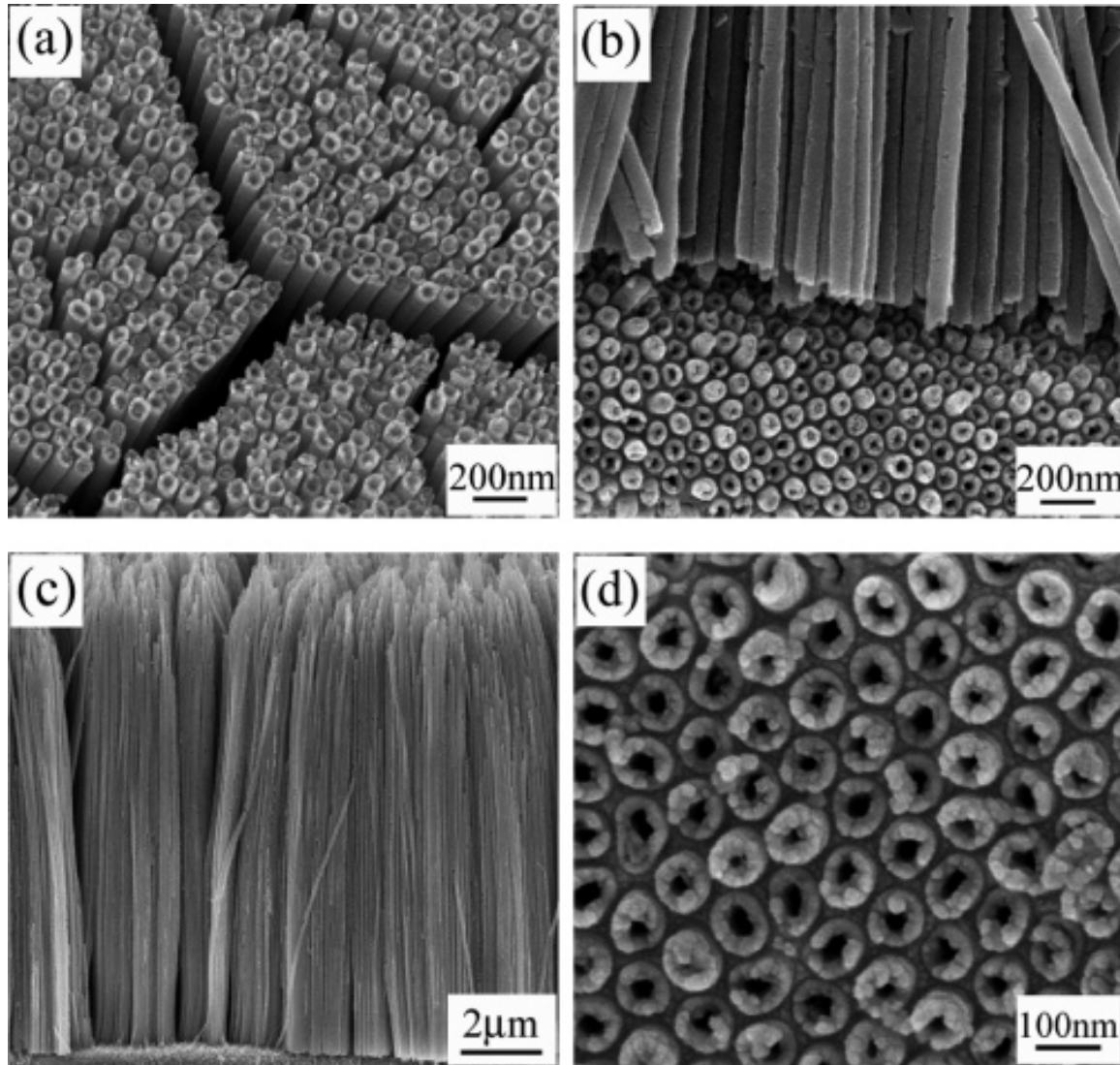
Figure 1.4 SEM images of ZnO nanotube arrays obtained by electrodeposition method. (reprint from Li *et al*. *J. Phys. Chem. C* **2007**, *111*, 7288-7291)[37]

Table 1.1 List of different ZnO nanostructures using various fabrication methods

Nanostructures	Fabrication method	Ref.
Nanorods	VLS	42
	Elecrodeposition	41
	Hydrothermal	31,33,36,43
	VS	25,26
Nanobelts	VS	24,44,45
	VLS	23
	Electrochemical deposition	46
Nanowires	VLS	15,47-51
	VS	45,52-54
	Hydrothermal	55-57
Nanotubes	Elecrodeposition	37,38
Nanosprings	VS	13,58
Nanorings	VS	59,60
Nanocombs	VS	61-63
Nanosheets	Elecrodeposition	40
Nanosaws	VS	61-64
Nanodisk	Hydrothermal	65
	VS	66,67
Nanopropeller	VS	68
	Elecrodeposition	39
Nanotetrapods	VS	69,70
Nanoflowers	Hydrothermal	32,34,35
Nanoporous structures	Electrochemical deposition	71
Nanocastles	VS	72
Nanonails	VS	73

Electroplating is primarily used for depositing a layer of material to bestow a desired property to a surface. This method has been used recently to synthesize many nanostructures. Electrodeposition of different ZnO nanostructures has been demonstrated by several groups.[37-41] Novel well-defined ZnO nano-/microstructures such as hexagonal nanotapers, hexagonal platelets, and rhombohedral rods can be achieved by using simple amine and inorganic ions to control the growth behavior of the crystal. Figure 1.4 shows a representative ZnO nanotube obtained by electrodeposition.

1.1.2 Family of ZnO Nanostructures

The family of ZnO nanostructures is big, which includes nanorods, nanobelts, nanowires, nanotubes etc. successfully grown via a variety of methods. The list of different ZnO nanostructures is shown in Table 1.1. Figures 1.5-1.16 show SEM and TEM images of ZnO nanorods, nanobelts, nanowires, nanopropellers, nanorings, nanosprings, nanotubes, nanodisks, and nanocastles.
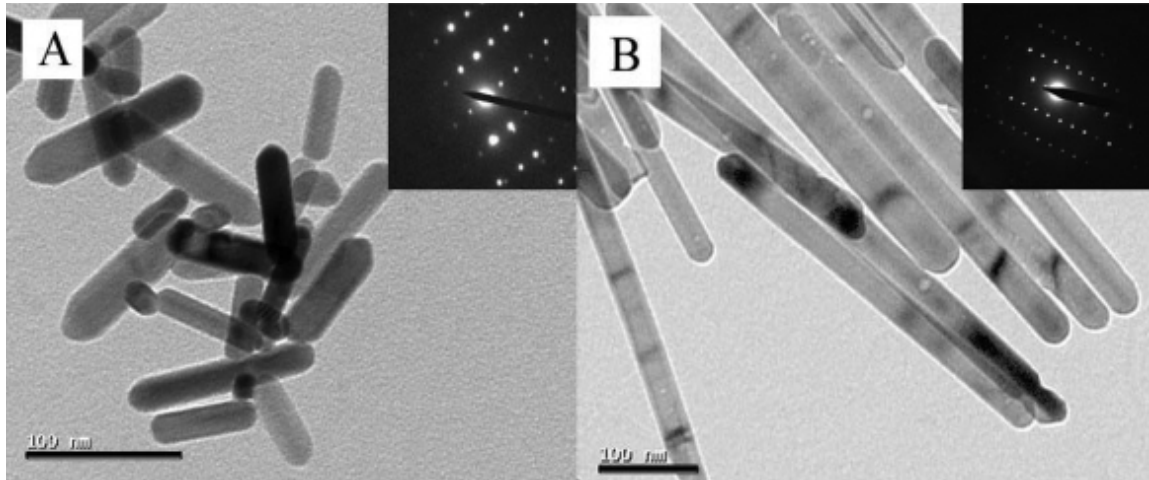
Figure 1.5 TEM images of ZnO nanorods. (reprint from Cheng *et al*. *Chem. Comm.* **2004**, 986-987)[36]
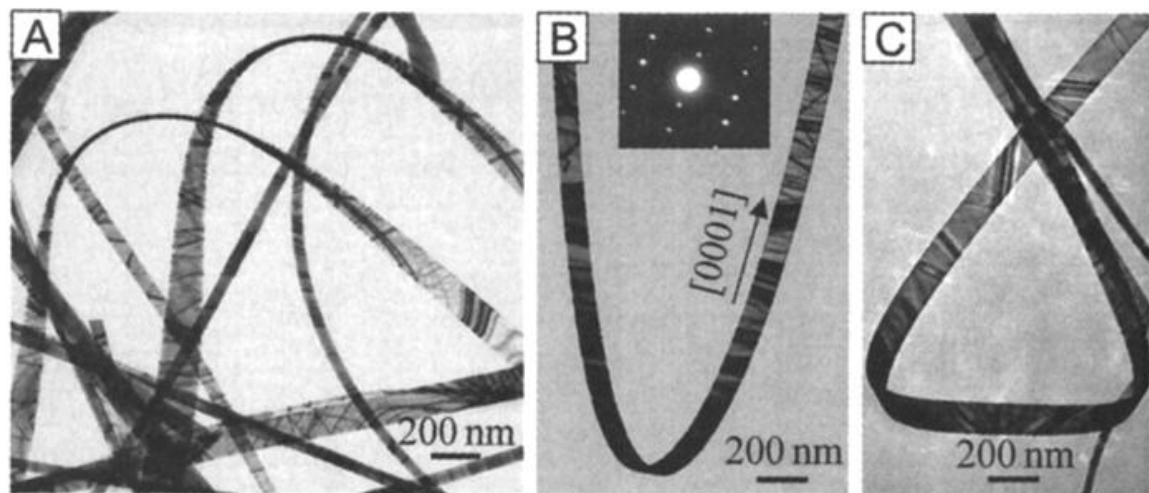
Figure 1.6 TEM images of ZnO nanobelts. (reprinted from Pan *et al*. *Science*, **2001**, *291*, 1947-1949)[24]
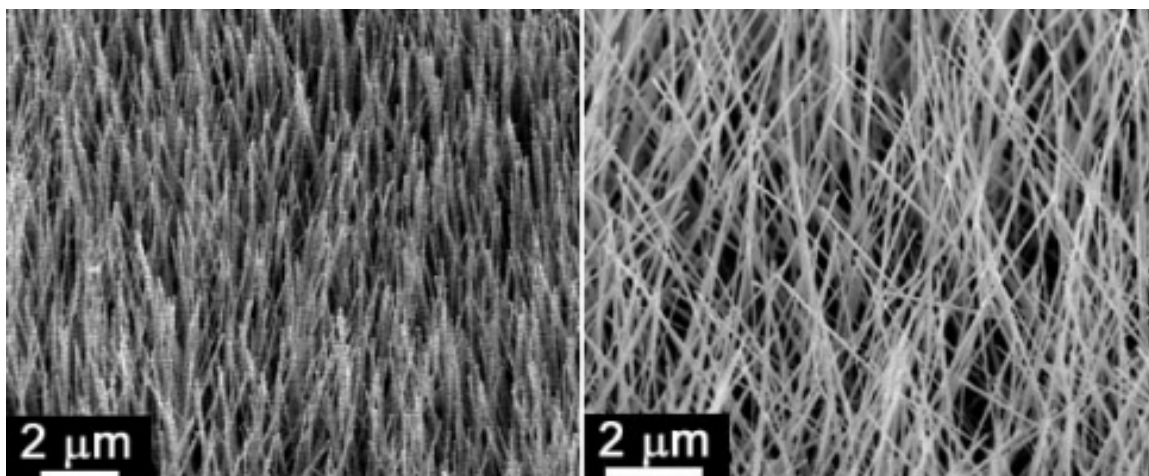
Figure 1.7 SEM images of tilted undoped ZnO nanowires. (reprint from Bae *et al*. *J. Phys. Chem. B* **2005**, *109*, 2526-2531)[54]
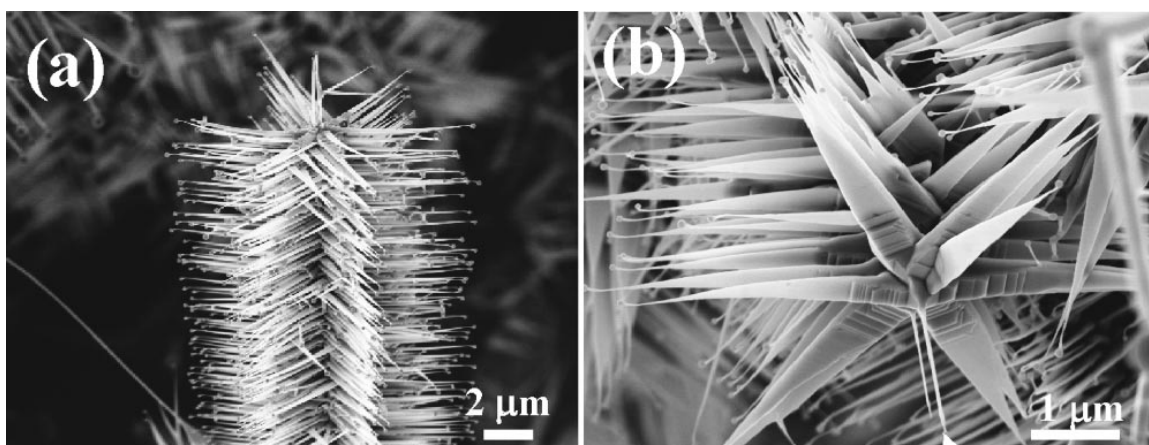
Figure 1.8 SEM images of ZnO nanopropeller arrays. (reprint from Gao *et al*. *Appl. Phys. Lett.* **2004**, *84*, 2883-2885)[68]
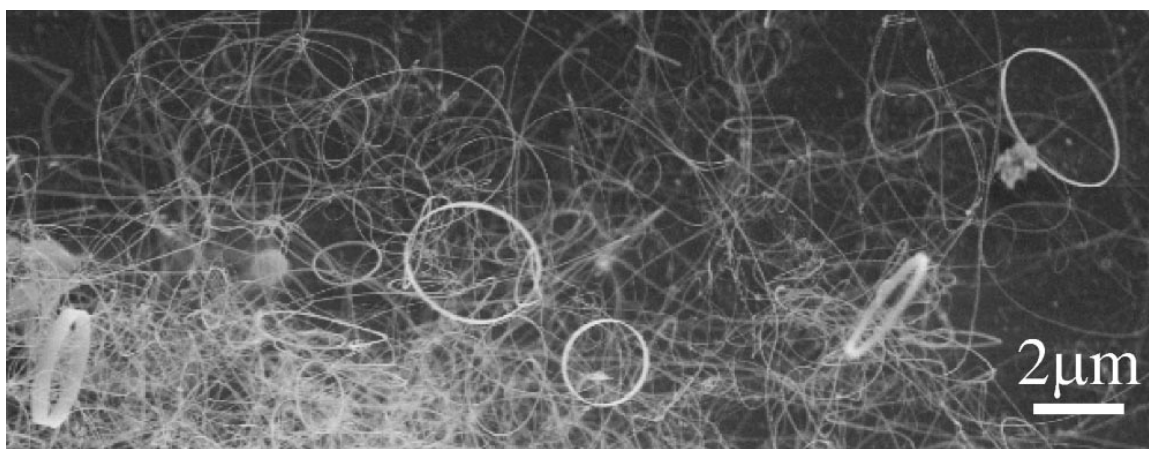
Figure 1.9 SEM image of ZnO nanobelts and nanorings. (reprint from Ding *et al*. *Phys. Rev. B* **2004**, *70*, 235408)[59]
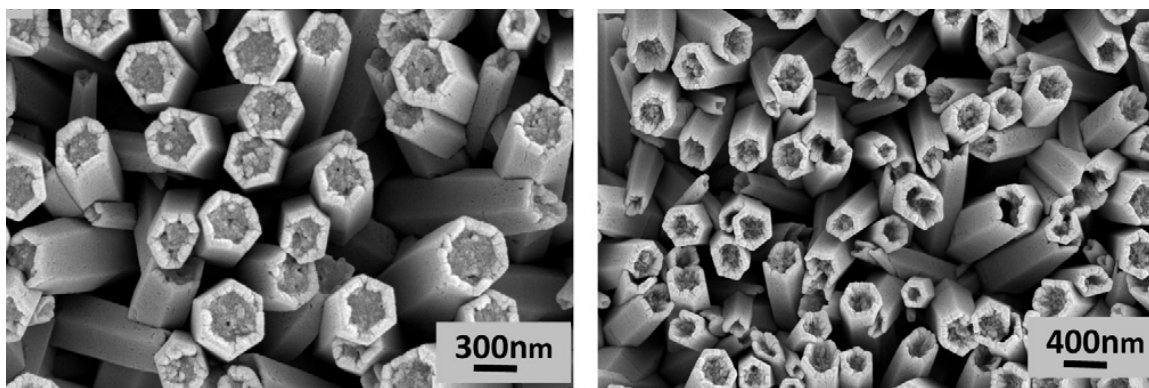
Figure 1.10 SEM images of the ZnO nanotube arrays. (reprint from Yang *et al*. *Ceram. Int.* **2012**, *38*, 4555-4559)[74]
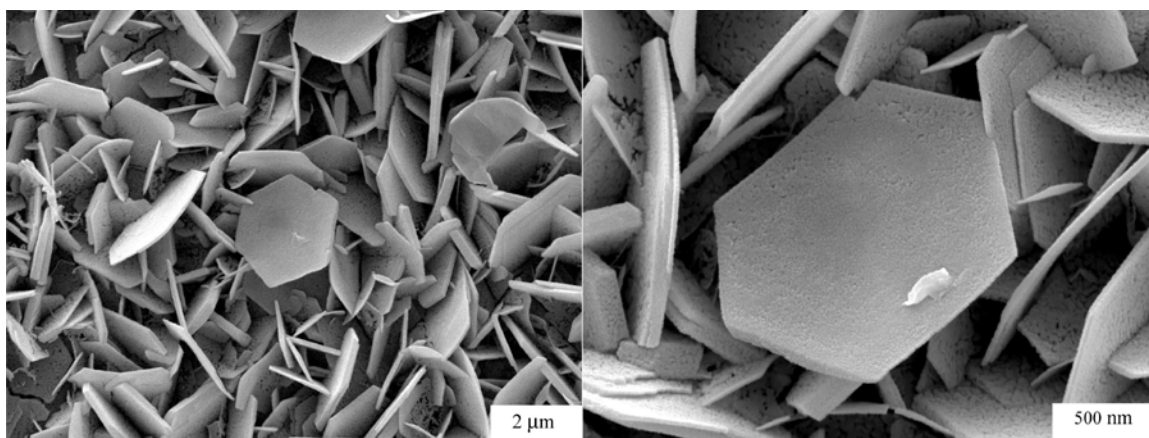
Figure 1.11 SEM images of ZnO nanodisks. (reprint from Deng *et al*. *Anal. Chem.* **2008**, *80*, 5839-5846)[75]
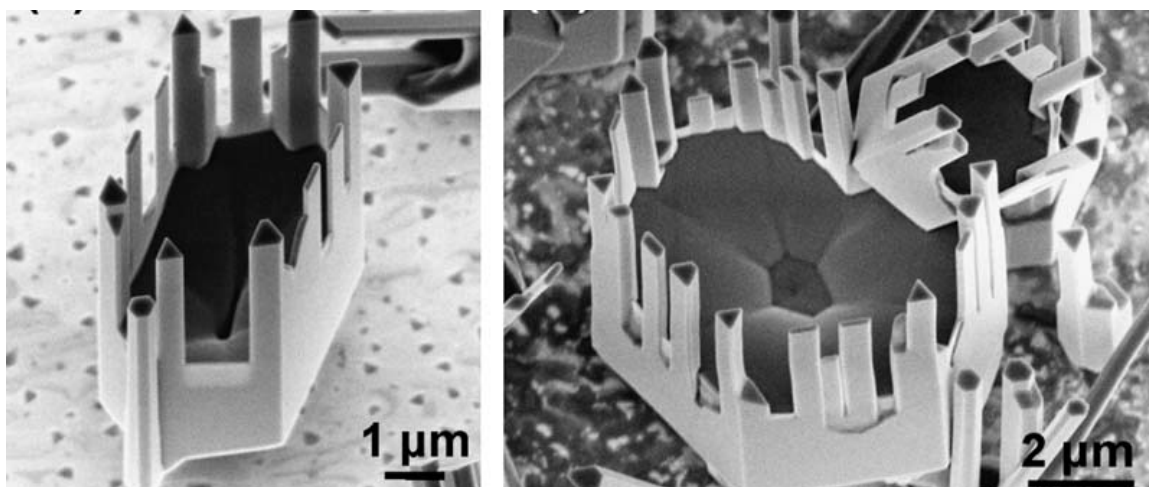
Figure 1.12 SEM images of ZnO nanocastles. (reprint from Wang *et al*. *Chem. Phys. Lett.* **2006**, *424*, 86-90)[72]
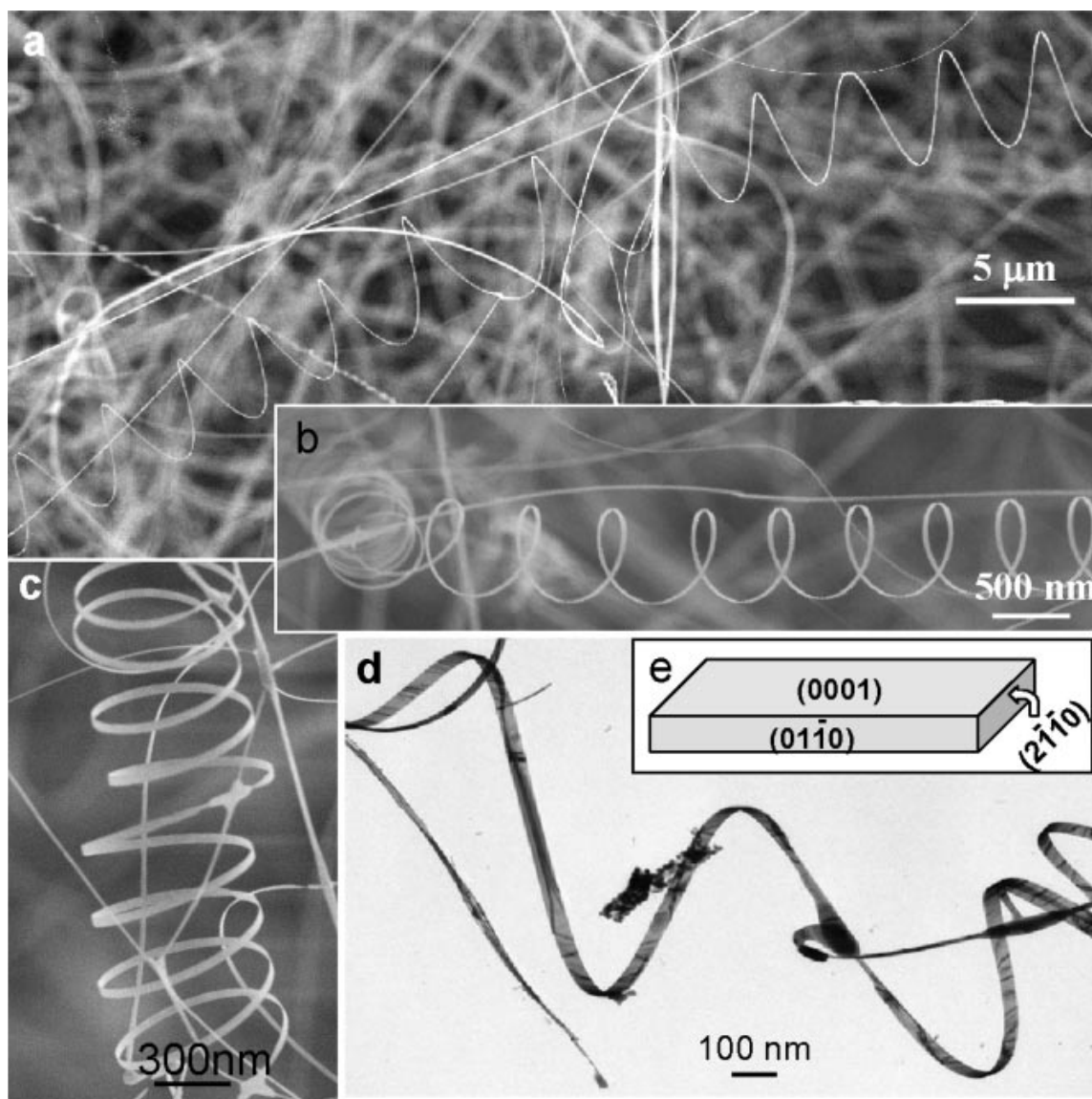
Figure 1.13 SEM and TEM images of ZnO nanosprings. (reprint from Z.L.Wang, *Annu. Rev. Phys. Chem.* **2004**, *55*, 159-196)[13]

1.1.3 Mechanical Properties of ZnO Nanostructures

ZnO nanostructures hold tremendous promise for novel and versatile devices due to their intrinsic semiconducting and piezoelectric properties, such as ultraviolet photodetectors,[76-80] sensors6,[6,81,82] field effect transistors,[83] intramolecular p-n junction diodes,[84] schottky diodes,[85] and light emitting device arrays.[86] The reliability and stability

of these devices with predictable and reproducible performance depend on the

mechanical properties of ZnO nanostructures.

Table 1.2 Elastic moduli of ZnO nanostructures characterized by various techniques.

Nanotructure	Size (nm)	Method	E (GPa)	Ref.
Nanowire	25.5	Quantifying the lateral force using AFM	198.0	87
	46.0		111.5	87
	80.0		102.6	87
	134.4		104.3	87
	45		29 ± 8	4
Nanobelt	Width-to-thickness:5-50	Nanoindentation	40 ± 5	88
	Thickness:50-140 Width: 70-700	3-point-bending using AFM	38.2 ± 5	89
	Thickness:50-140 Width:270-700	Nanoindentation	31.1 ± 1.3	89
	Thickness:115 Width:125	Fitting the elastic bending shape obtained by AFM	162 ± 12	90
	Width:31 Thickness:20	Mechanical resonance in TEM	56.3 ± 0.9	3
	3 with growth direction $[2\bar{1}\bar{1}0]$	MD simulations	210.31	91
	3 with growth direction $[01\bar{1}0]$		219.89	91
	3 with growth direction: [0001]		140.37	91
	1 with growth direction $[2\bar{1}\bar{1}0]$		307.4	91
	1 with growth direction $[01\bar{1}0]$		325.75	91
	1 with growth direction [0001]		339.76	91
	2	Density-functional-theory (DFT)	220	92
	1.6		105	92
nanowire	17	Electric-field-induced resonance method	220	93

The mechanical properties of materials involve various concepts such as hardness,

stiffness, and piezoelectric constants, Young's and bulk moduli, and yield strength. The

small dimension of different nanostructures raises serious challenges for experimental measurements of mechanical properties relevant to device applications. An example is that there are conflicting reports of the elastic modulus depending on the dimensions of ZnO nanostructures. Elastic modulus reported so far spans the range 30 GPa to 350 GPa. Table 1.2 summaries the elastic modulus of ZnO nanostructures with different size obtained by various characterization methods.

1.1.4 Mechanical stability of ZnO Nanostructures

ZnO as the star of nanostructures have been paid a great deal of attention. The reliability and/or functionality of ZnO nanostructures are heavily dependent on the mechanical properties of individual nanostructures. When ZnO nanostructures are exposed to air, UV light, or an electron beam, their mechanical properties can change accordingly.

The remarkable photoinduced stiffening in a single ZnO nanobelt using nanoindentation and atomic force microscopy has been reported by Zhao *et al.*[94] The apparent elastic modulus of a ZnO nanobelt exposed to illumination with photo energy greater than the band gap becomes much larger than that under darkness. For instance, the elastic modulus of the ZnO nanobelt in darkness and 550 nm high pass illumination is 15 ± 3 GPa and 22 ± 4 GPa, respectively, while it is 70 ± 14 GPa under 360 nm UV illumination. The physical mechanism for the observed phenomena is analyzed in terms of the surface effect and the electric strain induced by the photogeneration of free carriers in a ZnO nanobelt.

Zang *et al.*[95] have reported a remarkable phenomenon that electron beam irradiation (EBI) increases the Young's modulus of zinc tin oxide (ZTO) nanowires as much as 40% compared with the pristine nanowires. An *in-situ* uniaxial buckling test on individual nanowires was conducted using a nanomanipulator in a scanning electron microscope. Zang *et al.* propose that EBI results in substantial atomic bond contraction in ZTO nanowires, accounting for the observed mechanical stiffening. The observation of remarkable electrical self-healing in mechanically damaged ZnO nanobelts has also been reported by Zang *et al.*[96] Nanoindentation into intrinsically defect-free ZnO nanobelts induces deformation and crack damage, causing a dramatic electrical signal decrease. Two self-healing regimes in the nanoindented ZnO nanobelts are revealed. The physical mechanism for the observed phenomena is analyzed in terms of the nanoindentation-induced dislocations, the short range atomic diffusion in nanostructures, and the local heating of the dislocation zone in the electrical measurement.

1.2 Thermal Stability of ZnO Nanostructures

The thermal stability of nanostructures in nanodevices and nanoenabled energy systems has both theoretical and practical interests, because the stability during heating is a major concern for the application of nanomaterials, and the melting behavior of the nanomaterials is an attractive aspect for fundamental research. Thermodynamic properties of nanomaterials are different from those of bulk materials. The surface-to-volume ratio increases and the melting temperature may remarkably decrease when the size of a solid particle reduces to the nanometer scale.

1.2.1 Melting Depression in Nanostructures

Melting depression in one and zero-dimensional nanostructures has attracted a great deal of research interest in recent years, because of its importance in fundamental low-dimensional physics research as well as in technological application. The thermodynamic properties of nanostructures are quite different from those of the bulk materials and depend on the structure size. Surface tension, vapor pressure, melting point, and heating capacity etc. vary drastically as size decreases. The size dependence of thermodynamic properties may also result from surface effects because the most atoms in nanostructures occupy the surface. Surface atoms will be less stable than inside atoms due to their lower coordination number.[97] To lower the surface energy, nanostructures tend to decrease their surface area. As the size decreases beyond a critical value, due to the increase in the surface-to-volume ratio, the melting temperature deviates from the bulk value and becomes a size-dependent property.

Al particles exhibit many thermo-physical features, distinct from those found at micro-size. Molecular-dynamics were performed using isobaric-isoenthalpic (NPH) ensembles to predict the melting of nanosized aluminum particles and to investigate the effect of surface charge development on the melting. The melting temperature of an aluminum nanoparticle increases monotonically with increasing size, from 473 K at 2 nm to a bulk value of 937 K at approximately 8 nm.[98] Eckert *et al.*[99] synthesized nanocrystalline aluminum powders by mechanical attrition in argon, hydrogen, and oxygen atmospheres and observed similar phenomena. The melting point of a 40 nm or larger particle decreases from 940 K to 840 K when the particle size is reduced to 13 nm. In addition, Alavi *et al.*[100] performed molecular-dynamics simulations for clusters of aluminum atoms using the Streitz-Mintmire potential and canonical (NVT) ensembles.

The aluminum nanoparticles with the atoms less than 850 show dynamic coexistence melting where solid and liquid phases are stable over a range of temperatures. The temperature range of bistability becomes narrower and shifts to higher temperatures as the size of the nanoparticle increases.

The melting point of Ge and Zr bulk materials is 930 °C and 1852 °C. However, Ge nanowires from 10-100 nm in diameter and Zr nanowires of 1.43 nm in diameter melt at 650 °C and 627 °C, respectively.[101,102] Iron grains of submicron-size recently have been observed to melt partially at 650 °C, which is much lower than that of the bulk Fe of 1536 °C.[103] Qi et al.[104-106] studied the thermodynamic properties of nanoparticles, such as Mo and W using a generalized bond energy model to account for the size dependent cohesive energy and melting temperature of nanocrystals. The depression of cohesive energy of nanocrystals was predicted, which is consistent with the experimental values of Mo and W nanoparticles. The melting depression has been studied experimentally on nanosized tin by Wronski et al. using transmission electron diffraction.[107] The apparatus consists of an evaporator attached to a small furnace, and 5-10 nm particles are produced by evaporating a tin pellet from the surface and then condensing it on a thin carbon or silicon monoxide substrate. The melting points agree reasonably well with the predictions based on classical theories, which show a nonlinear relationship with the reciprocal of the particle size. The melting temperature of tin becomes size-dependent for particles smaller than 10 nm, decreasing from a bulk value of 505 to 425 K for a 5 nm particle.

1.2.2 Melting Depression in ZnO Nanostructures

ZnO nanostructures have been the research focus as functional and structural nanobuilding blocks in nanoelectronics and nanooptoelectronic devices in the last decade.

The thermal stability of ZnO nanostructures has to be carefully considered because of their extremely fine size and high surface areas. It was found that the size effect on the melting temperature of ZnO was quite strong from thermodynamic simulation.
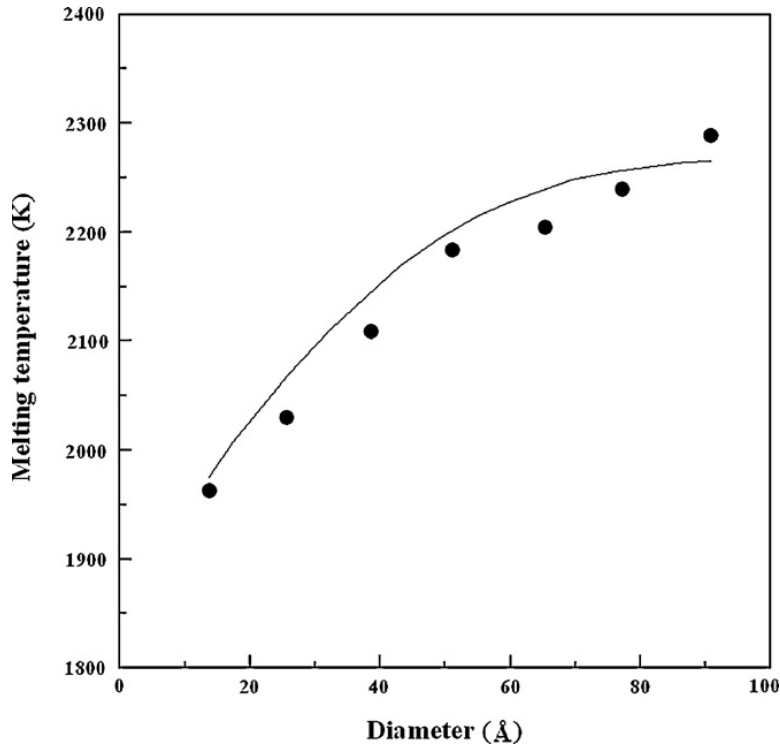
Figure 1.14 Melting temperature of hexagonal ZnO nanowire as function of nanowire diameter. (reprint from Su *et al. Mater. Res. Bull.* **2011**, *45*, 1686-1691)[109]

Guisbiers et al.[108] adopted the top-down approach using classical thermodynamics to investigate the size and shape effects on the melting temperature of ZnO nanostructures. They found that a spherical ZnO nanoparticle with a radius of 5 nm could melt at ∼1220 °C. Based on melting point estimations as a function of size and shape, certain ZnO nanostructures, such as nanotube with size less than 10 nm, may not be viable for nanoelectronics or nanophotonic devices, because melting point is too close to, or in some cases even below, room temperature. Su *et al.*[109] studied the structural

17

stability, orientation effect and melting characteristics of ZnO nanowires using the molecular dynamics with many-body tightbinding potential. The structural stability is affected by the geometric shape of the cross section of a nanowire. Hexagonal nanowire is more stable than that with other shapes, namely, rectangular, triangular, rhombohedra, octagonal, and circular. The structural stability and melting temperature of a nanowire is affected by its diameter because of the surface energy and unfavorable coordination. It was observed that hexagonal ZnO nanowires transform to metastable circular-type structures at temperatures lower than their melting point. Figure 1.14 shows the melting temperature of hexagonal ZnO nanowire as function of nanowire diameter.[109]

1.3 Dispersion of CNTs and Graphene Sheets

Exceptional physical properties, high aspect ratio and low density of graphene have made CNTs and graphene ideal candidate for developing the next generation of polymer composites. CNTs and graphene, as the strongest materials ever measured, are known to have a Young's modulus of 1 TPa and an intrinsic strength of 130 GPa. Such values are 5 and 20 times greater than those for steel, respectively, at just 1/6 the weight. CNTs and graphene sheets, therefore, are expected to serve as mechanical reinforcements for lightweight composite systems.

1.3.1 Dispersion of CNTs

The exceptional mechanical, thermal and electrical properties of carbon nanotubes (CNTs) make them promising for many engineering applications, such as composite reinforcements, scanning probe tips, field emission sources, hydrogen storage systems,

super-capacitors, quantum devices, and biosensors. Depending on the type of nanotubes, single-walled or multi-walled CNTs and their post-treatment, CNTs can be used as supercapacitor electrodes with the specific capacitance ranging from 4 to 135 F/g.[110] CNTs, moreover, can be either metallic or semiconductive depending on the chirality of their structure.

A critical step for both fundamental research and practical applications of CNTs is to disperse CNTs into certain media, such as ethanol, water, or polymers. Because CNTs are insoluble and have the propensity to form bundles due to their strong hydrophobicity and van der Waals attractions, a great deal of effort has been invested to develop efficient and low-cost approaches to realize full dispersion of CNTs. These approaches can be divided into two categories, namely mechanical dispersion and surface modification. Mechanical methods, such as ultrasonication, high shear mixing, and ball milling, have been commonly employed to disperse one kind of material into another, including CNTs. The shear mixing approach uses a shear force produced by air flow in conjunction with a rapidly moving fluid to disperse and align CNTs. The torque produced by the shear force can make CNTs aligned and straightened along the axial direction.[111] Although the shear mixing method is faster in aligning CNTs, a large proportion of CNTs were often not completely separated. Ultrasonication and ball milling can also be used to disperse CNTs in solutions or polymers. These two methods are easy to operate but usually take long time to disperse CNTs with low-efficiency. During ultrasonication and ball milling, CNT fracture failure often occurs, which destroys the integrity of the dispersed CNTs. Surface modification can be either chemical or physical. Chemical surface modification enables the CNT surface to be functionalized through reactions with atoms or molecules such as

fluorine, alkanes, or by ionic modification to improve their chemical compatibility.

Wetting or adhesion characteristics of CNTs can be altered through functionalization to

reduce their tendency to agglomerate. For example, an amine group or dangling amine

moieties can easily form amide bonds by interacting with carboxylic groups located at the

ends, sidewalls, and defect sites of the oxidized CNTs and further induce the formation of

salt.[112,113] This method has been proven to be effective in terms of making a CNT

solution stable and preventing them from aggregating in the solution state. Such

dispersed CNTs, however, tend to clump together after drying. Physical surface

modification is the noncovalent stabilization of CNTs by interaction with certain

solvents, such as surfactants, polymers, and biomolecules.[114] For instance, sodium

dodecylbenzene sulfonate was used as surfactant to assist the dispersion of CNTs. A

major drawback of both chemical and physical surface modifications is that impurities

are often introduced into the CNT solution, and these are difficult to remove in further

processes or applications.

1.3.2 Dispersion of Graphene Sheets

Although graphene has superior properties comparable with CNTs, such a star

largely disappointed us in manufacturing lightweight, high strength polymer composites

because of graphene sheet agglomeration in the matrix - one of the major roadblocks

limiting their reinforcing effect and applications.[115,116] The mechanical properties of

graphene reinforced polymer composites are considerably below their theoretically

predicted potential.[117] A common observation from previous studies has shown that the

magnitude of improvement is, to a large extent, dependent upon the state of dispersion of

graphene sheets in the matrix. Only when monolayered graphene sheets are homogeneously dispersed and randomly oriented within the matrix, the enhancement could be improved. Graphene sheets often aggregate into flakes of weakly interacting monolayered sheets due to their strong hydrophobicity and van de Waals attraction.[118] One flake can contain up to several hundred monolayered sheets.[119,120] The monolayered sheets within a flake can easily slide over each other and the shear modulus of graphene flakes is relatively low.[121] The aggregates of graphene sheets also dramatically reduce the aspect ratio of the reinforcement.

Chemical functionalization of graphene sheets may reduce their agglomeration tendency to some extent,[115,122-124] the major drawback of chemical surface modification is that impurities are often introduced into the graphene solution and the presence of foreign stabilizers is undesirable for most applications. Many researchers have turned their attention to derivatives of graphite, especially graphite oxide, which is hydrophilic and has a larger interlayer distance than graphite.[125,126] Individual graphene oxide sheets can be produced in water more easily than monolayered graphene sheets, and such graphene oxide sheets may form stable dispersion after ultrasonication. Posterior deoxygenation is able to restore electrically insulating graphene oxide to conductive graphene, but many of the resultant sheets are crumpled and wrinkled.[127] New strategies to produce monolayered graphene sheets without destroying their unique structural integrity are strongly needed.

1.4 Overview of the Dissertation

In Chapter 2, the remarkable water molecule-induced stiffening in ZnO nanobelts is observed. It was found that the elastic modulus of ZnO nanobelts could increase

21

significantly from 40 GPa under ambient condition up to 88 GPa at 80% relative humidity. The physical mechanism for this phenomenon was explained in terms of increasing surface stress induced by water molecule adsorption on ZnO nanobelt surface.

Chapter 3 investigates the thermal stability depression in ZnO nanobelts using the *in-situ* transmission electron microscope. The ZnO nanobelts may begin to melt at ~600 °C and melt completely when the temperature increases to 850 °C. The apparent thermal depression in the ZnO nanobelts is attributed to the surface relaxation that occurs in terms of surface atoms moving outward resulting in bond length increase and bond energy decrease. The surface energy is higher than the internal energy in the ZnO nanobelts, which drives the surface atoms in the potential well to easily jump out.

In Chapter 4, a novel method combining hydrogen passivation and ultrasonication was developed to disperse multi-walled carbon nanotubes (MWCNTs) in an ethanol solution and an epoxy resin. Excellent dispersion of the MWCNTs was achieved in both media. The dispersion mechanism was discussed in terms of MWCNT/hydrogen interaction, bond energy, and ultrasonication-aided C-H bond formation. Three-point bending tests of the MWCNT/epoxy composites revealed a remarkable increase in elastic modulus with increasing MWCNT content.

Chapter 5 demonstrats that the graphene reinforcing potential can be significantly enhanced through the excellent dispersion of graphene sheets in the matrix material and the strong graphene-matrix bonding by the coupled hydrogen passivation and ultrasonication technique. The fabricated graphene/epoxy composites exhibit remarkable increase in their elastic modulus, fracture strength, and fracture energy.

Chapter 6 discusses fabrication of exceptional-tough CNT/SiC composites using a chemical vapor infiltration (CVI) technique. Nanotube pullout and sequential breaking and slippage of the walls of the CNTs during failure are consistently observed for all fractured CNT/SiC samples. These energy absorbing mechanisms result in the fracture strength of the CNT/SiC composites about one order of magnitude higher than the bulk SiC. The CVI-fabricated CNT/SiC composites have an intimate tube/matrix interface and an amorphous, crack-free SiC matrix, enabling the composites to resist oxidization at 700–1600 °C in air.

Chapter 7 summarizes all key results of the environmental effects on mechanical and thermal behaviors of ZnO nanobelts, and dispersion of carbon nanostructures, and nanocomposites reinforced by CNTs and Graphene. This chapter also recommends future research directions including the effect of electron beam on ZnO nanostructures, high yield of dispersed graphene and CNTs, etc.

CHAPTER 2

WATER MOLECULE-INDUCED STIFFENING IN ZnO NANOBELTS

One-dimensional (1-D) nanostructures, such as nanowires, nanobelts, and nanotubes of different materials, have significant applications as nanoscale interconnects and active/functional components of electronic and optoelectronic devices, sensors, actuators, nanoelectromechanical systems (NEMS), and energy generation/conversion systems. The functionality and/or reliability of those nanodevices and nanoenabled energy systems are determined by the elastic properties of individual 1-D nanostructures. However, the mechanisms for how the elastic modulus of 1-D nanostructures depends on their surface conditions are barely understood. The 1-D nanostructures have remarkably higher surface-to-volume ratio than their bulk counterparts. In a 1-D nanostructure, the surface exerts great influence on its overall elastic properties. As a result, the elastic modulus of a 1D nanostructure is determined by both the bulk elastic modulus and surface elastic modulus.[128,129] In a simplified way, the elastic modulus of a 1-D nanostructure can be written as equation 2.1[128]

$$Y_N = Y_B \left(\frac{A_B}{A_{Tot}} \right) + Y_S \left(\frac{A_S}{A_{Tot}} \right) \qquad\qquad 2.1$$

where Y_N, Y_B, and Y_S refer to the elastic modulus of the nanostructure, bulk, and surface, respectively. A_{Tot}, A_B, and A_S represent the respective corss-sectional areas of the nanostructure, bulk, and surface. Thus, the elastic response of a 1-D nanostructure depends strongly on the surface elastic constant.[130]

The surface of most 1-D nanostructures is quite reactive. When exposed to air, nanostructures could absorb water molecules on their surfaces. In particular, water molecule absorption is inevitable in nanostructure fabrication and operation. It is reasonable to assume that the adsorbed water molecules would alter the properties of surface and further the elastic properties of nanostructures. The adsorption of water molecules on ZnO surface was found to be energetically favorable from first principles density functional theory (DFT) calculation.[131,132] When water molecules are adsorbed on the surface of 1-D wurtzite nanostructures, a significant charge transfer will occur between the surfaces and the adsorbates. However, the effect of water molecule absorption on the elastic properties of 1-D nanostructures has never been reported. Here we report the first observed water molecule-induced stiffening in ZnO nanobelts using atomic force microscopy three-point bending. The physical mechanism for this phenomenon was analyzed in terms of the water molecule-induced surface atom motion and surface stress using the first principles DFT calculations.

2.1 EXPERIMENTAL

The synthesis of ZnO nanobelts was carried out in a three-zone horizontal tube furnace under controlled conditions. Equal amounts of ZnO and graphite powder (weight ratio 1:1) were used as the source materials. A silicon (100) wafer with a 20 nm thick gold coating was used as the substrate and catalyst, respectively. After synthesis, the ZnO nanobelts, together with the silicon (100) substrate, were removed from the tube furnace for direct morphology examination and composition analysis by scanning electron microscopy (SEM; Zeiss Ultra plus FESEM) equipped with an energy dispersive X-ray

(EDX) detector and high-resolution transmission electron microscopy (HRTEM, JEOL 2010 F at 200 kV). After SEM/EDX/HRTEM studies, the nanobelts were further detached from the substrate and dispersed into ethanol by ultrasonication. A few drops of this solution were spread onto silicon trench for three-point bending test. An atomic force microscopy (AFM) tapping-mode silicon tip with a tip radius of 15 nm and a height of 10-15 µm was employed to obtain the scan profiles of individual ZnO nanobelts. To avoid any image artifacts, an AFM tapping-mode silicon tip was calibrated carefully on a standard calibration sample from Veeco Metrology Group with the gratings (NGR-21 200 nm deep × 10 µm pitches) for a three-dimensional profile and AFM calibration.

2.2 RESULTS AND DISCUSSION
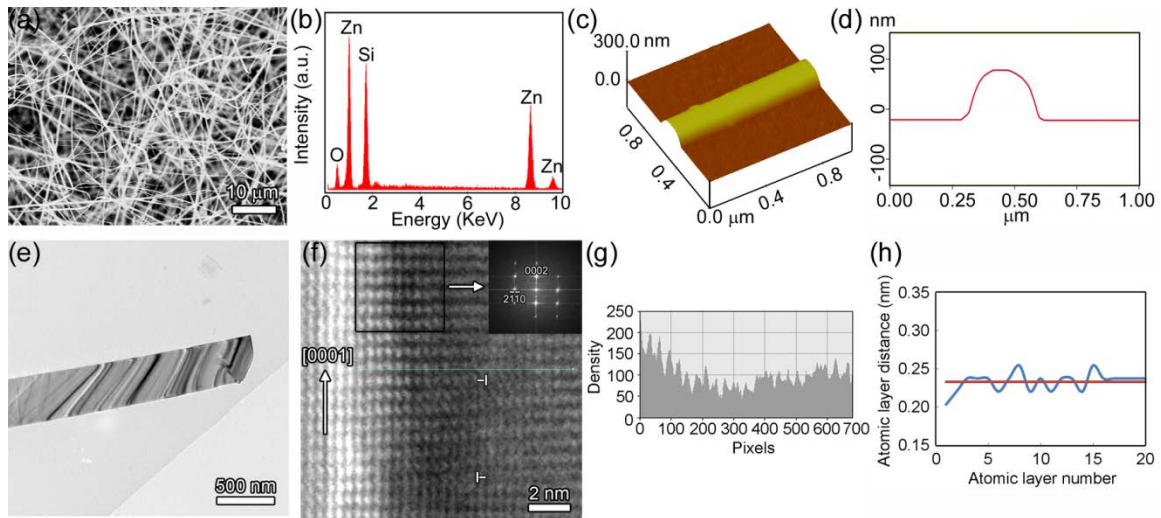
Figure 2.1 (a) SEM image of the as-synthesized ZnO nanobelts. (b) EDX spectrum obtained from the ZnO nanobelts. (c,d) Respective 3-D AFM image and corresponding cross-sectional height profile of an individual ZnO nanobelt. (e,f) Respective low-magnification and high-resolution TEM images of the ZnO nanobelt. (g) Intensity line scan across the nanobelt marked by dotted line (blue) in (f). (h) Lattice spacing profile in the surface layer along the radial/cross-sectional direction of the ZnO nanobelt.

Figure 2.1 shows the representative SEM image of the as-synthesized ZnO nanobelts. The nanobelts exhibit significant zinc and oxygen peaks in the EDX spectrum (Fig. 2.1b). Figs. 2.1c and 2.1d shows the representative 3-D AFM image and corresponding cross sectional height profile of a single ZnO nanobelt, showing a rectangular cross-section. The SEM and AFM examinations show that the nanobelts have smooth surfaces with width ranging from 120 to 350 nm and thickness from 50 to 150 nm. Figs. 2.1e and 2.1f show the respective low-magnification and high-resolution TEM images of the nanobelts. The fast Fourier transform (FFT) pattern (insert in Fig. 2.1f) indicates that the growth direction of the ZnO nanobelt is along the [0001] direction. A few edge dislocations with a Berger's vector of $(a/3) < 11\bar{2}0 >$ were observed in the surface layer. The intensity line scan across the nanobelt (Fig. 2.1g) was obtained by processing the image of Fig. 2.1f using Gatan Digital Microgragh software. The lattice spacing profile in the surface layer along the radial/cross-sectional direction of the nanobelt (Fig. 2.1h) was plotted by measuring the atomic distance between each two adjacent atoms in Fig. 2.1f using Photoshop software. The lattice spacing in the first 15 surface atomic layers exhibits a wavelike characteristic, as shown in Fig. 2.1g, indicating the existence of negative surface strain and then alternative negative and positive strains in the surface atomic layers along the radial direction of the nanobelts. The dislocations in the surface layer accommodate the surface stress /strain which will be discussed later in the first principles DFT calculations.

Three-point bending tests were performed on individual ZnO nanobelts over the trench on the Si wafer with two ends of the nanobelt bonded by electron beam induced deposition of carbon in SEM, as shown in Figure 2.2a. It should be noted that the

measured total deflection (d_t) consists of the deflection from the cantilever (d_c) and the deflection from the nanobelts (d_n). in order to eliminate the indentation effect (i.e., the depth that the tip was pushed into the nanobelt) and the silicon tip cantilever deflection effect on the net nanobelt deflection during bending, a baseline was first obtained by performing a bending test on a nanobelt sitting on a solid substrate at the desired applied load level; such a baseline (curve 1) is shown in Fig. 2.2b.
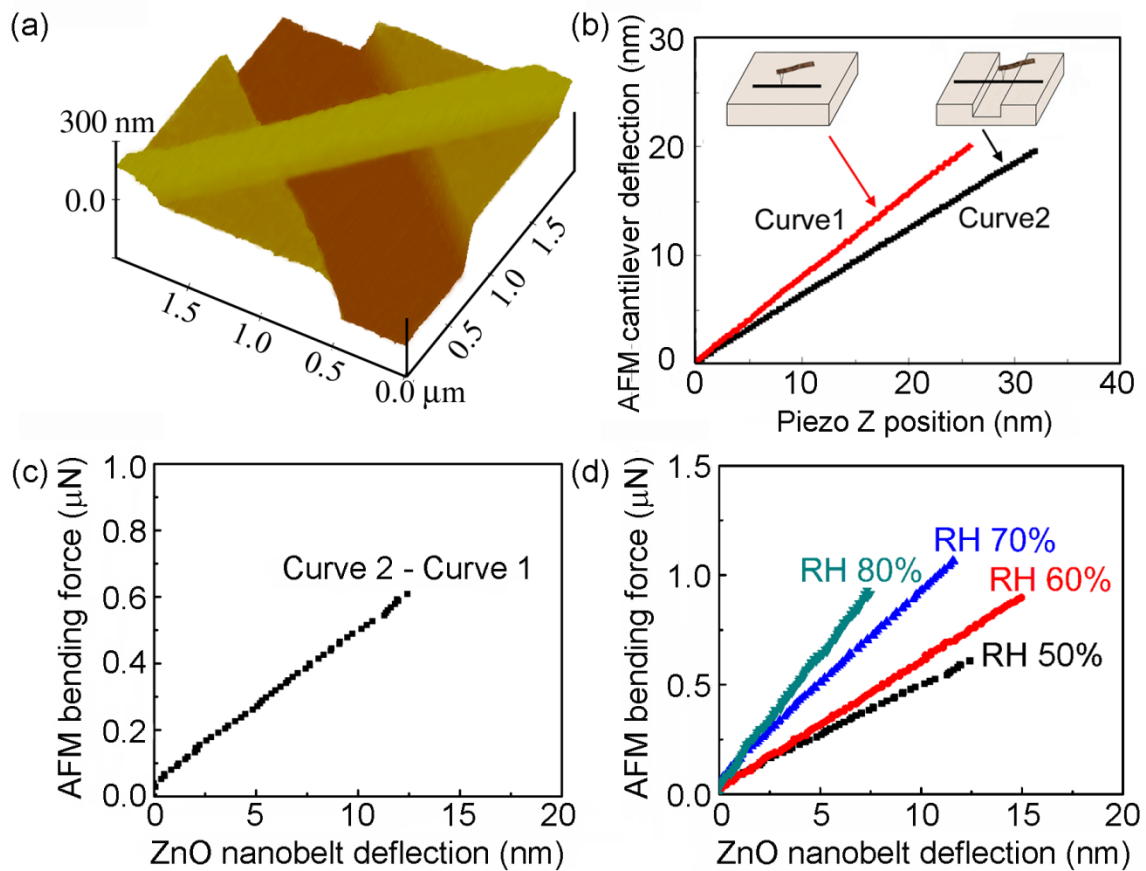
Figure 2.2 (a) The 3-D AFM image showing a ZnO nanobelt over the trench on the Si wafer. (b) Cantilever deflection as a baseline (curve 1) was obtained by performing three-point bending using an AFM tip directly. (c) Applied bending force as a function of net nanobelt deflection. (d) Applied bending force as a function of net nanobelt deflection under different relative humidity (RH) levels.

Fig. 2.2b also shows the AFM cantilever-piezo position along the z-direction curve (curve 2) obtained from a typical suspended ZnO nanobelt under an applied load of

around 1 µN. the corresponding applied force-nanobelt deflection relationship was obtained by subtracting the deflection caused by the indentation effect and the cantilever deflection from the total deflection obtained from the suspended nanobelt system (curve 2 minus curve 1 in Fig. 2.2c) and Fig.2.2d shows such a curve between the AFM applied load and the net deflection of a single ZnO nanobelt under different relative humidity (RH) levels. Here the ambient condition refers to the RH level of 50%. All the samples were stopped in loading after initial elastic modulus of individual ZnO nanobelts. It is clear that the AFM applied load and nanobelt deflection maintains a very good linear relationship (Fig. 2.2d).
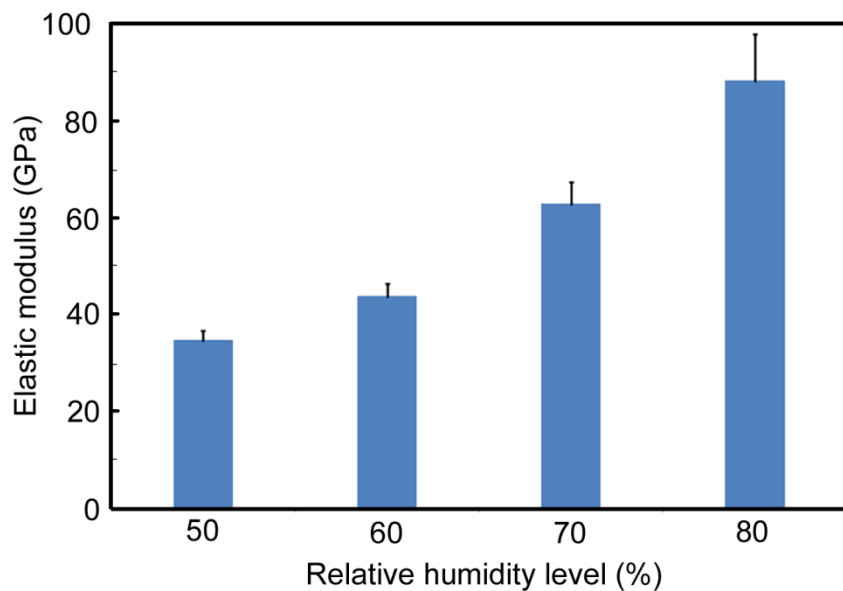
Figure 2.3 Elastic modulus values measured at different relative humidity levels.

In order to measure the bending elastic modulus of ZnO nanobelts, the spring constant of each nanobelt must be known. The spring constant of a nanobelt (k_n) is defined as the slop of the initial linear potion of the AFM applied force-nanobelt deflection curve, as shown in Fig. 2.2b. On the basis of the assumption that the nanobelt

follows the linear elastic theory of as isotropic material, the elastic modulus of a ZnO

nanobelt, E_n, can be calculated from the equation

$$E_n = \frac{FL^3}{192 d_n I} = \frac{K_n L^3}{192 I} \qquad\qquad 2.2$$

$$I = \frac{bh^3}{12} \qquad\qquad 2.3$$

where I is the moment of inertia. b and h are the width and height of the nanobelt,

respectively. L is the suspended length of the nanobelt and F is the applied load at its

midpoint position. K_n is the spring constant of the nanobelt.

To study the humidity effect on the elastic modulus of ZnO nanobelts, water

molecules were introduced into the AFM chamber. The elastic modulus of ZnO nanobelts

under ambient condition was measured to be 40 GPa, which is in good agreement with

the reported value.[3,4,94] As the humidity level increased, the slope of the AFM applied

force-nanobelt deflection curve increased accordingly, as shown in Fig. 2.2d. Figure 2.3

shows the elastic modulus of ZnO nanobelts increased significantly from 40 GPa under

ambient condition up to 88 GPa at the humidity level of 80%. To achieve less RH levels

(<10% or clean surface), experimentally the following two basic requirements must be

met: (1) the synthesized nanobelts need to be transported directly from the synthesis

furnace to the AFM in a vacuum chamber without exposing to air (ambient condition),

and (2) the synthesized nanobelts need to be heated up to 100 °C to vaporized the water

molecules. The heating process will change the surface state, which in turn affects the

elastic modulus of the nanobelt. To elucidate the relation between relative humidity and

elastic modulus of ZnO nanobelts, first-principles DFT calculations were used to

theoretically determine the surface elastic properties with H_2O adsorbates.

(a)

(b)   (c)
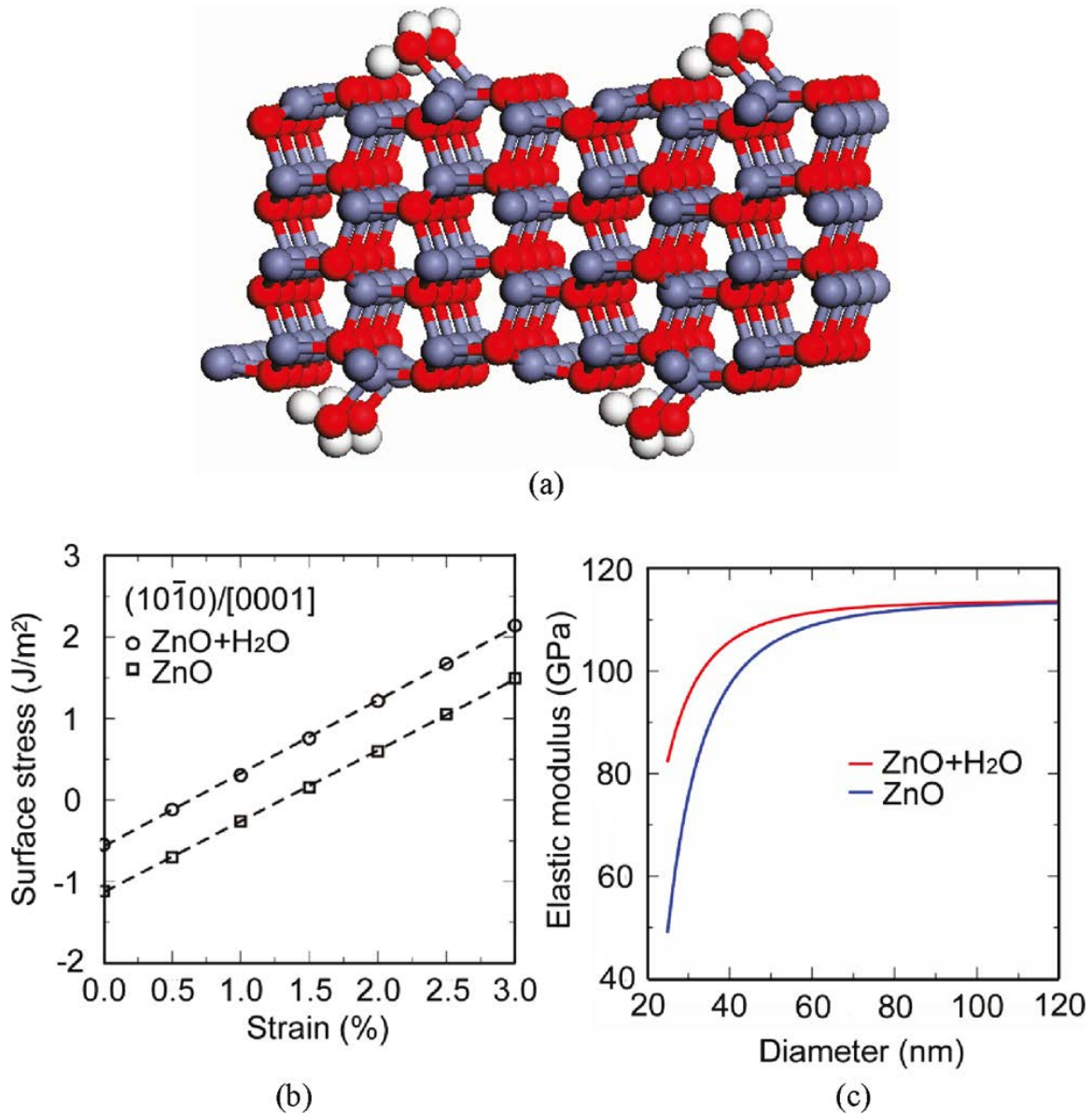
Figure 2.4 (a) Atomic structure of water molecule adsorbed on ZnO $(10\bar{1}0)$ surface. In the figure, red balls represent O atoms, gray balls represent Zn atoms, and white balls represent H atoms. (b) Variation of surface stress as a function of strain for the ZnO $(10\bar{1}0)$ surface with and without water adsorption. (c) Predicted size-dependent elastic modulus of ZnO nanowires enclosed by the $(10\bar{1}0)$ surface with and without water adsorption.

Equilibrium ZnO has a wurtzite crystal structure. In this work, we evaluated the surface stress of the nonpolar ZnO $(10\bar{1}0)$ surface with and without water adsorption

31

using first-principles DFT method. The calculations were performed using the VASP code.[133,134] We used the projector augmented wave method and the generalized gradient approximation of Perfew and Wang for exchange and correlation.[135,136] We chose a kinetic energy cutoff of 600 eV to expand the electric wave functions in the plane wave basis and a $6 \times 4 \times 2$ k-point grid for k-space integration. To Model $(10\bar{1}0)$ surfaces, we used a supercell containing eight surface layers and eight layers of vacuum. Each surface layer contains four Zn atoms and four O atoms.

The equilibrium structure of ZnO surface was obtained through optimizing atomic positions using first-principles DFT method. Significant relaxation in the $(10\bar{1}0)$ surface has been observed. In bulk terminated $(10\bar{1}0)$ surface, ZnO-O dimmers lay in parallel to the surface. In contrast, the Zn-O dimmers would tilt relative to the surface after relaxation. We found in our calculations that in the outmost layer of $(10\bar{1}0)$ surface, Zn cations move inward by $\Delta d_{\perp}(Zn) = -0.34\text{\AA}$ and move laterally toward O by $\Delta d_{\parallel}(Zn) = 0.16\text{\AA}$, O anions move inward by $\Delta d_{\perp}(O) = -0.002\text{\AA}$, and the resultant tilt angle of Zn-O dimmers to be ω=10.6°. Our theoretical results for the $(10\bar{1}0)$ surface are in good agreement with the experimental data ($\Delta d_{\perp}(Zn) = -0.45 \pm 0.1\text{\AA}$, $\Delta d_{\parallel}(Zn) = 0.1 \pm 0.2\text{\AA}$, $\Delta d_{\perp}(O) = -0.05 \pm 0.1\text{\AA}$, and ω=12 ± 5°).[137] Apparently, this surface relaxation process significantly reduced the surface stress along the [0001] direction of the $(10\bar{1}0)$ surface from 2.46 J/m^2 for the bulk-terminated surface to -1.13 J/m^2 for the fully relaxed reconstructed surface. A negative surface stress for the fully

relaxed $(10\bar{1}0)$ surface implies that the surface will energetically favor expansion and

hence lower the elastic modulus of ZnO nanobelts with clean surface.[138]

Further, we relaxed the $(10\bar{1}0)$ surface of ZnO with a water molecule coverage of

0.25 monolayer (ML), under which the interaction between the H_2O molecules is

negligible and a dissociative H_2O adsorption is not favored. Following previous DFT

calculation results, we placed the adsorbed H_2O molecule on the top of the hexagonal

channel of the ZnO surface and away from the top of Zn atom, as shown in Figure 2.4a.

After relaxation, the distance between the O atom of the H_2O molecule and the adjacent

surface Zn atom is 2.08 Å. This interaction drives the adsorbing Zn atom (one of the four

surface Zn atoms) to move outward of the surface by 0.35 Å from the relaxed clean ZnO

surface (note: this Zn atom almost moves back to its position in a bulk-terminated

surface). Accompanying with this structural change, the surface stress of ZnO $(10\bar{1}0)$

surface with H_2O adsorption would become -0.55 J/m^2, which is still negative, but 0.58

J/m^2 higher than that of the clean surface. Employing the model, we calculated the elastic

modulus of ZnO nanowires assuming that they were enclosed with either the clean or

0.25 ML water-adsorbed $(10\bar{1}0)$ surface. Our results plotted in Fig. 2.4c indicated that (1)

the ZnO nanowires would have higher elastic modulus when their surface adsorbed water

molecules as compared to the ZnO nanowires without water adsorption; and (2) the

elastic modulus of ZnO nanowires was lower than the bulk elastic modulus value and

decreased with the decreasing size of the nanobelts when the water coverage is 0.25 ML.

Consequently, our theoretical study revealed that water molecule adsorption on the ZnO

surface would attract surface Zn atoms to move outward and hence increase the value of

surface stress of ZnO surface. It is notable that nanowire and nanobelt differ only in the

shape of their cross sections. Hence, our calculation results for ZnO nanowires are quantitatively applicable to ZnO surface could increase surface stress and thus enhance the elastic modulus of ZnO nanobelts with the increase of humidity as unequivocally demonstrated by our experimental tests. Although we only simulated the case of 0.25 ML water molecule adsorption on the ZnO surface in this work, our conclusion on water adsorption enhancing the elastic modulus of ZnO nanobelts is expected to also hold true for other coverage of water adsorption. This is because the increase of surface stress correlates with the relaxation of the ZnO surface with water adsorption, while detailed DFT study showed that varying the water coverage does not cause much change in the extent of the relaxation in the ZnO surface.

2.3 SUMMARY

Strong water molecule induced stiffening effect was observed for the first time in ZnO nanobelts by atomic force microscopy three-point bending test. Such effect has theoretical and practical significance. The first principles DFT study unveiled that water molecule adsorption on the ZnO surface could attract surface Zn atoms to move outward and hence increase the value of surface stress of ZnO surface. Increasing surface stress associated with water adsorption is believed to be responsible for the experimentally observed enhancement of the elastic modulus of ZnO nanobelts with the increase of humidity. Our finding suggests that the elastic properties of 1-D ZnO nanostructures could be tuned by depositing water molecules on their surfaces, and in turn humidity could be sensed by monitoring the elastic property changes in 1-D ZnO nanostructures.

CHAPTER 3

THERMAL STABILITY DEPRESSION IN ZnO NANOBELTS

The application of nanomaterials in nanodevices and nanoenabled energy systems has advanced remarkably.[8,139,140] To keep the devices and systems fulfilling the deserved functions, the nanostructures should hold superior mechanical, electrical, and thermal stabilities. To the best of our knowledge, the melting behaviors and thermodynamic properties of nanomaterials are different from those of bulk materials. As the size of a solid particle reduces to nanoscale, the surface-to-volume ratio will remarkably increase and the melting temperature may apparently decrease. For example, the melting points of Ge and Zr bulk materials are 930 °C and 1852 °C, respectively. However, Ge nanowires with diameter of 10~100 nm and Zr nanowires with diameter of 1.43 nm may melt at 650 °C and 627 °C, respectively.[101,102] Recently, it is also observed that iron grains with submicron-size melt partially at 650 °C which is much lower than 1536 °C, the melting point of bulk iron.[103] Particle size plays an important role in melting point depression of all above nanomaterials. Theoretical investigations, such as molecular-dynamics simulation and thermodynamic simulation, have been done to study the melting point of nanomaterials.[98,100,102,141] Molecular-dynamics simulation is performed using isobaric-isoenthalpic ensembles to predict the melting point of aluminum nanoparticles and investigate the effect of surface charge development in the melting process. The melting temperature of an aluminum nanoparticle monotonically increases with the size increase, which is only 473 K at 2 nm and steps up to the bulk value of 937 K at 8 nm.[98]

ZnO nanostructures, spotlight of structural and functional nanobuilding blocks, have been intensively studied in the last two decades. The thermal stability of such nanostructures should be addressed. If one or two nanostructures in use suddenly fail, the whole nanodevice may malfunction. It is reported that the size effect on the melting point of ZnO is quite strong. The melting point of a ZnO nanowire with diameter of less than 10 nm could be close to or even below room temperature.[108] The size effect may result in the melting point depression in nanostructures, which is a commonly acceptable physical mechanism. However, two abstract questions are raised: why does the size effect happen and how does it work? Here, we limit our focus to the ZnO surface structures to answer such two questions. *In-situ* transmission electron microscope (TEM) can enable the visualization of nanostructures undergoing physical and chemical transformations. For instance, studies of nanostructure melting, growth, and coalescence have provided new insight about how size, shape, and interfaces affect phase behaviors.[142-144] In this chapter, we demonstrate that it is possible to directly observe the entire melting process of an individual ZnO nanobelt sitting in TEM. The melting point depression will be discussed in terms of surface structure and surface stress of ZnO nanobelts.

3.1 EXPERIMENTAL

The synthesis of ZnO nanobelts was carried out in a three-zone horizontal tube furnace under controlled conditions. Equal amounts of ZnO and graphite powders (weight ratio 1:1) were used as the source materials. A silicon (100) wafer with a ~5 nm thick gold coating was used as the substrate. After synthesis, the ZnO nanobelts together with the silicon (100) substrate were removed from the tube furnace for direct morphology

examination by scanning electron microscope (SEM; Zeiss Ultra plus FESEM) and transmission electron microscope (TEM; Hitachi HF 2000) equipped with an Aduro stage (Protochips, Inc.).
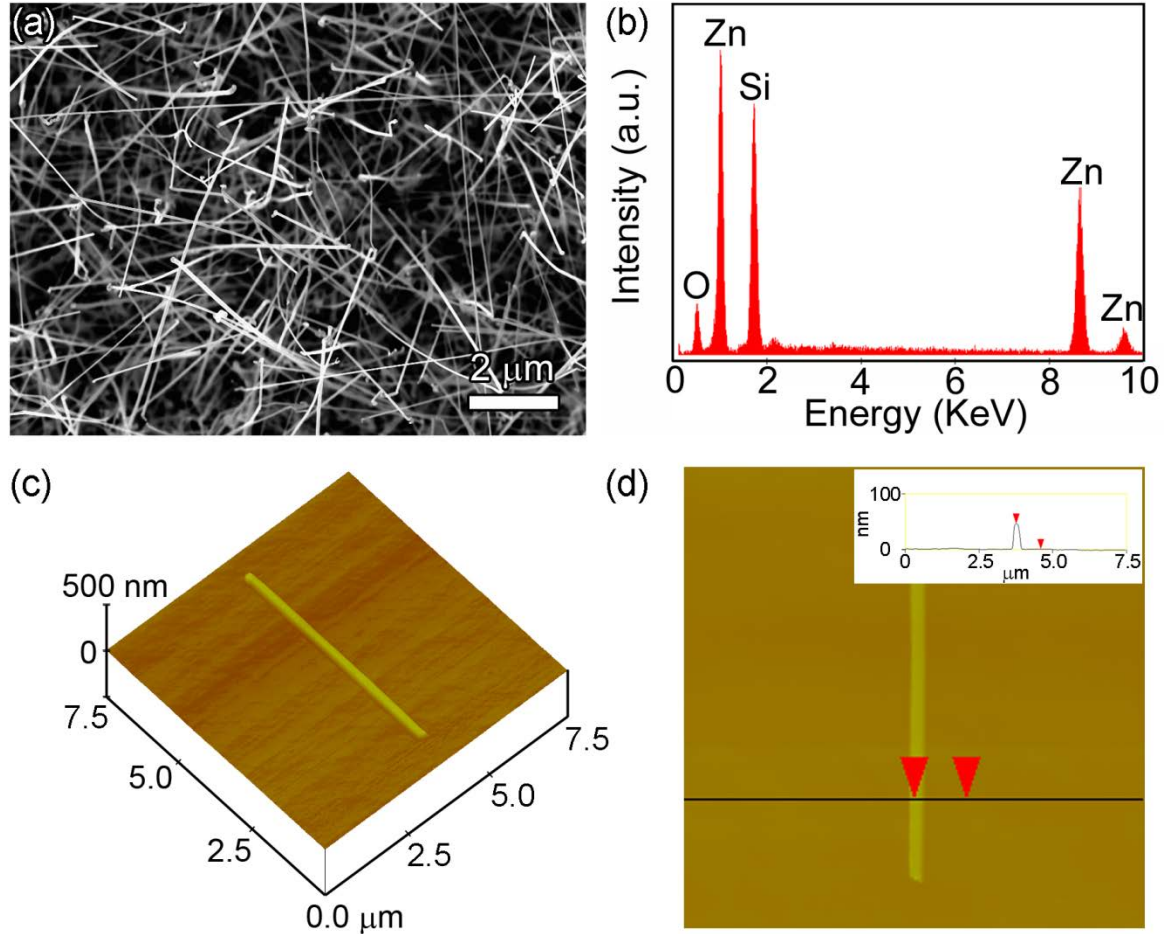
Figure 3.1 (a) SEM image of the as-synthesized ZnO nanobelts. (b) EDX spectrum obtained from the ZnO nanobelts. (c,d) Respective 3D and 2D AFM images of an individual ZnO nanobelt.

To avoid possible interference of Au catalyst on melting, the ZnO nanobelts were ultrasonicated in ethanol solution first, and then transferred onto a silicon wafer and an E-Chip, respectively. The E-chip was covered by a Si_3N_4 film with thickness of ~50 nm to support dispersed ZnO nanobelts. The ZnO nanobelt without Au tip was heated and analyzed using *in-situ* TEM. The temperature was set as 20 °C, 100 °C, 200 °C, 300 °C,

400 °C, 500 °C, 600 °C, 700 °C, 800 °C, and 850 °C, respectively. Each heating period was 2 min. The silicon wafer together with ZnO nanobelts was also heated at different temperature using a heating stage (INSTEC, HCP 601) in ambient condition. The temperature was controlled at 20 °C, 450 °C, 500 °C, 550 °C, 580 °C, and 600 °C, respectively. Each heating period was 2 h. The morphology of an individual ZnO nanobelt after heat treatment was checked by SEM and an atomic force microscope (AFM, Veeco 3100), respectively.

3.2 RESULTS AND DISCUSSION

The representative SEM image, EDX spectrum, and AFM images with cross-sectional height profile of the as-synthesized ZnO nanobelts are shown in Figure 3.1. The SEM and AFM examinations show that the nanobelts have smooth surfaces with width ranging from 50 to 150 nm and thickness from 20 to 50 nm. The thermal expansion and melting behaviors of an individual ZnO nanobelt were studied by *in-situ* TEM.
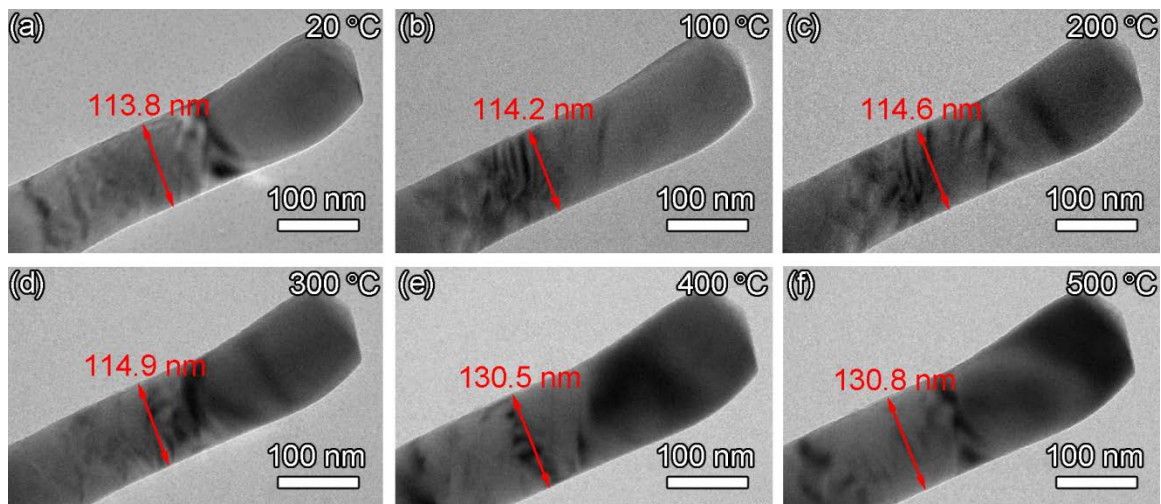
Figure 3.2 Thermal expansion of the ZnO nanobelt. TEM images of the ZnO nanobelt heated at (a) 20 °C, (b) 100 °C, (c) 200 °C, (d) 300 °C, (e) 400 °C, and (f) 500 °C, respectively. Each heating period is 2 min.

As the preamble for the subsequent melting, the thermal expansion will be discussed first. Figure 3.2 shows the entire thermal expansion process of the ZnO nanobelt with original width of 113.8 nm (Fig. 3.2a), which was heated at 100 °C, 200 °C, 300 °C, 400 °C, and 500 °C, respectively. Each heating period is 2 min. The ripple-like morphologies are due to the recombination of electrons and holes in the ZnO nanobelt. The energy of negative charged electron beam in the column is much larger than the band-gap energy, which induces formation of new electron-hole pairs. Electrons occupy the empty state associated with holes, leading to both carriers eventually annihilating in the process. Such recombination mechanisms can be reversed leading to carrier generation rather than recombination,[145,146] which is shown as ripple drifting in the ZnO nanobelt.
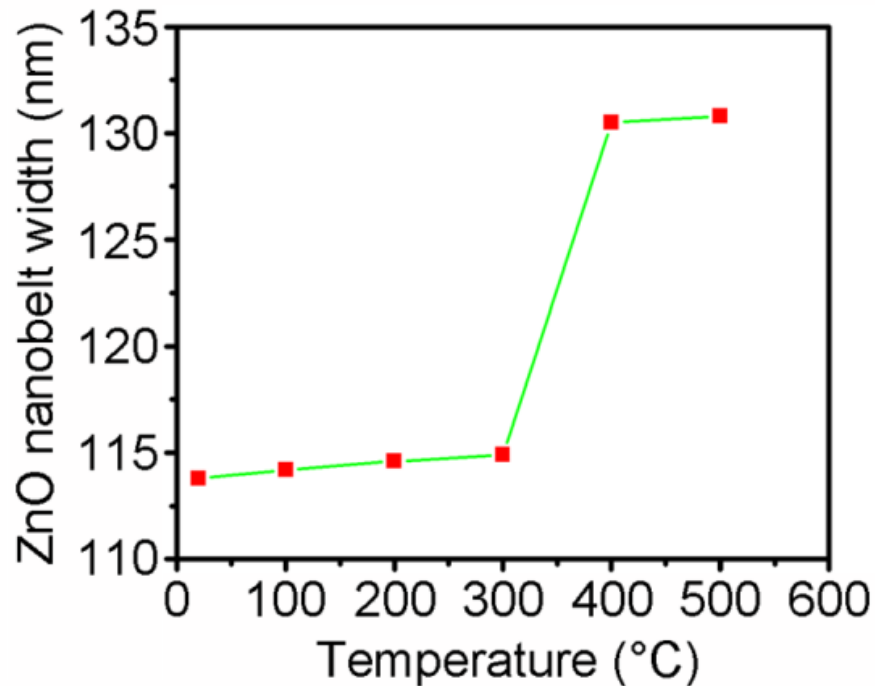
Figure 3.3 Dependence of the ZnO nanobelt width on temperature.
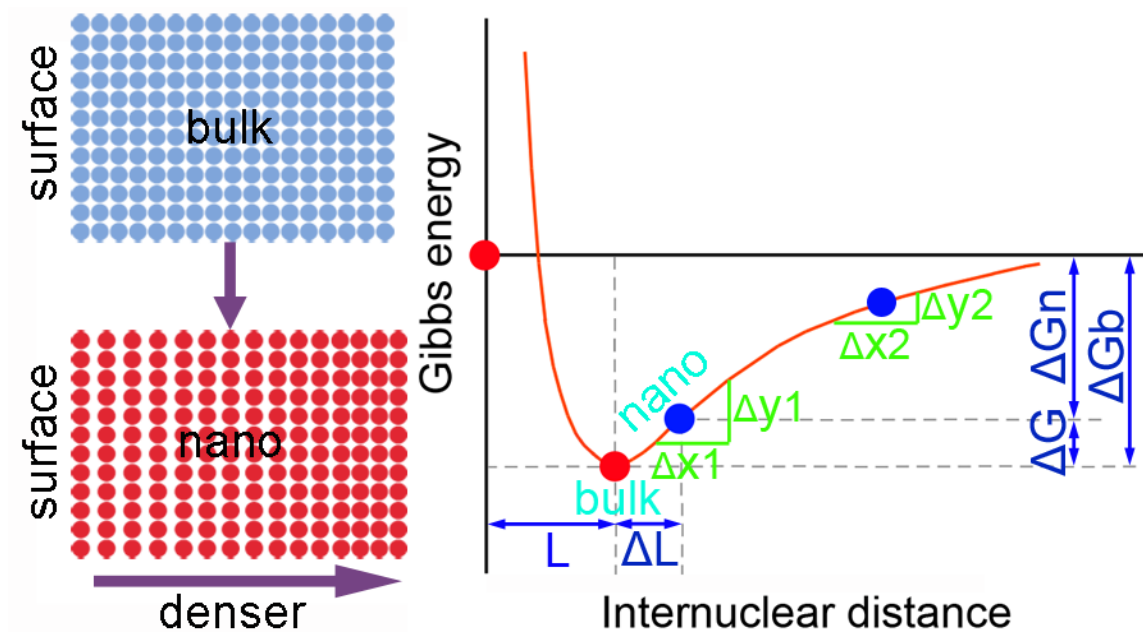
Figure 3.4 Schematic of crystal lattice of bulk and nano ZnO, and energy-distance curve.

The width of the ZnO nanobelt shown in Figs. 3.2b-3.2d gradually increases with the temperature less than 300 °C and reaches 114.9 nm at 300 °C, demonstrating 0.97 % increase compared with that of the ZnO nanobelt at room temperature. The thermal expansion coefficient of bulk ZnO at room temperature is 4.31×10^{-6}/K, however, the thermal expansion coefficient of the ZnO nanobelt across the growth direction at the temperature lower than 300 °C is 3.22×10^{-5}/K, which is close to one order of magnitude higher than that of bulk ZnO. Though the thermal expansion coefficient of the bulk ZnO as a function of temperature may hit 8.5×10^{-6}/K at 800K,[147] such value is still less than 3.22×10^{-5}/K for the ZnO nanobelt at 300 °C. As the size is down to nano scale, the surface effect can not be ignored, because the surface atoms will be less stable than inside atoms due to their lower coordination number. Surface atoms of free-standing nanocrystal also experience greater vibrational amplitude than those in the bulk, as they have no neighbors above them to restrain them.[148] However, atoms in bulk materials have lower

degree of freedom. It has been demonstrated that the surface relaxation does exist in the ZnO nanobelts. Zn cations may move outward by $\Delta d = 0.34$ Å and O anions move outward by $\Delta d = 0.002$ Å, which can lead to significant changes in mechanical properties of ZnO nanobelts.[97] Thermal properties, such as thermal expansion coefficient, of the ZnO nanobelts could also be affected. With the heat treatment temperature increase to 400 °C (Fig. 3.2e), the thermal expansion coefficient jumps to 3.67×10^{-4}/K, which is one order and two orders of magnitude higher than that of ZnO nanobelt at 300 °C and room temperature, respectively. The width of the nanobelt expands to 130.8 nm at 500 °C in Fig. 3.2f, indicating 17.0 nm increases in width compared with the original nanobelt. Figure 3.3 summerizes the dependence of ZnO nanobelt with upon temperature. Why does the thermal expansion coefficient of the ZnO nanobelt increase with the temperature increase? To address such a question, the energy-atom distance curve is drawn in Figure 3.4. The slope of the energy-atom distance curve can be defined as equation 3.1:

$$s = \frac{\Delta y}{\Delta x} \qquad\qquad 3.1$$

where Δx and Δy denote atom distance change and energy change that drives atom to move Δx. When the atom is at position 1, the slope is written as s_1 shown in equation 3.2. With temperature increase, the atom may move to position 2. The slope of the energy-atom distance curve will be s_2 shown in equation 3.3.

$$s_1 = \frac{\Delta y_1}{\Delta x_1} \qquad\qquad 3.2$$

$$s_2 = \frac{\Delta y_2}{\Delta x_2} \qquad\qquad 3.3$$

$$s_2 < s_1 \qquad\qquad 3.4$$
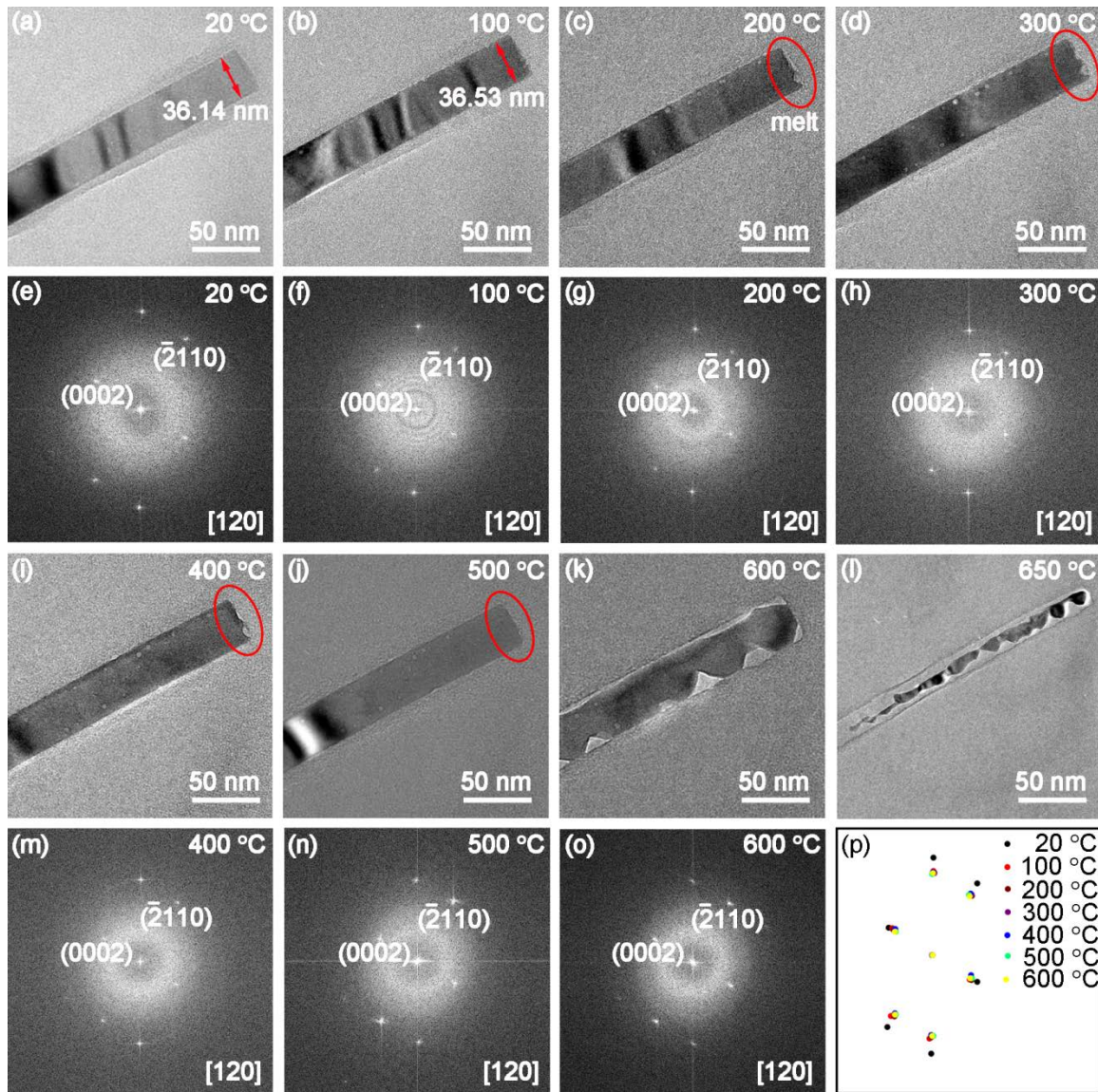
Figure 3.5 Heat-treatment on an individual ZnO nanobelt. TEM images of the ZnO nanobelt heated at (a) 20 °C, (b) 100 °C, (c) 200 °C, (d) 300 °C, (i) 400 °C, (j) 500 °C, (k) 600 °C, and (l) 650 °C. The corresponding diffraction patterns at different temperature are shown in (e-h) and (m-o). (p) Overlap of all diffraction patterns. Each heating period is 2 min.

The slope of energy-atom distance curve at position 2 is less than that at position 1 illustrated in equation 3.4, which means that to move the atom with same atom distance Δx will require less energy only if the atom is activated to move at lower temperature. The ZnO nanobelt at 300 °C or lower will expand at a relatively low thermal expansion coefficient. With temperature increase, both Zn and O atoms are easy to move outwards.

Though Zn and O atoms absorb same amount energy, both atoms can move with larger distance, resulting in higher thermal expansion in ZnO nanobelt at or over 400 °C. To further confirm whether the thermal expansion coefficient is resulted from phase transformation, the diffraction patterns are obtained at different temperature on a ZnO nanobelt shown in Fig. 3.5. The nanobelt is with growth direction of $(\bar{2}110)$. The cystal planes, (0002) and $(\bar{2}110)$ do not change with temperature increasing. However, the lattice distance of the ZnO nanobelt heated at different temperature increases compared with that of the one at the room temperature. The details of lattice distance at different temperature are shown in Figure 3.6.
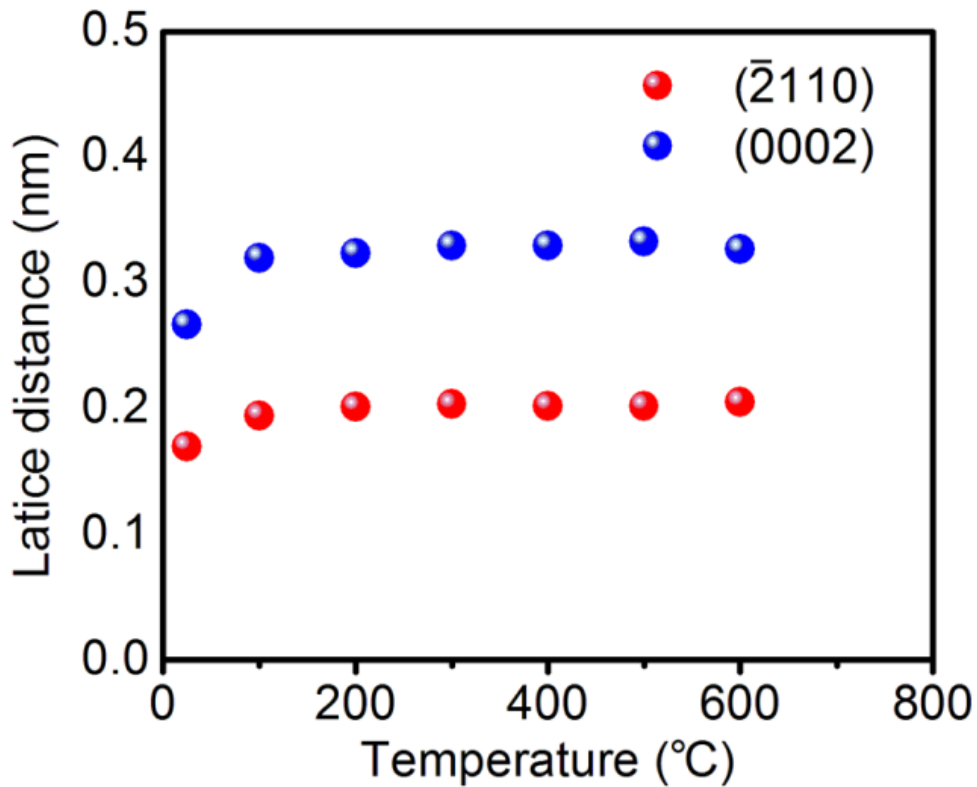
Figure 3.6 Lattice distance of the ZnO nanobelt at different temperature.
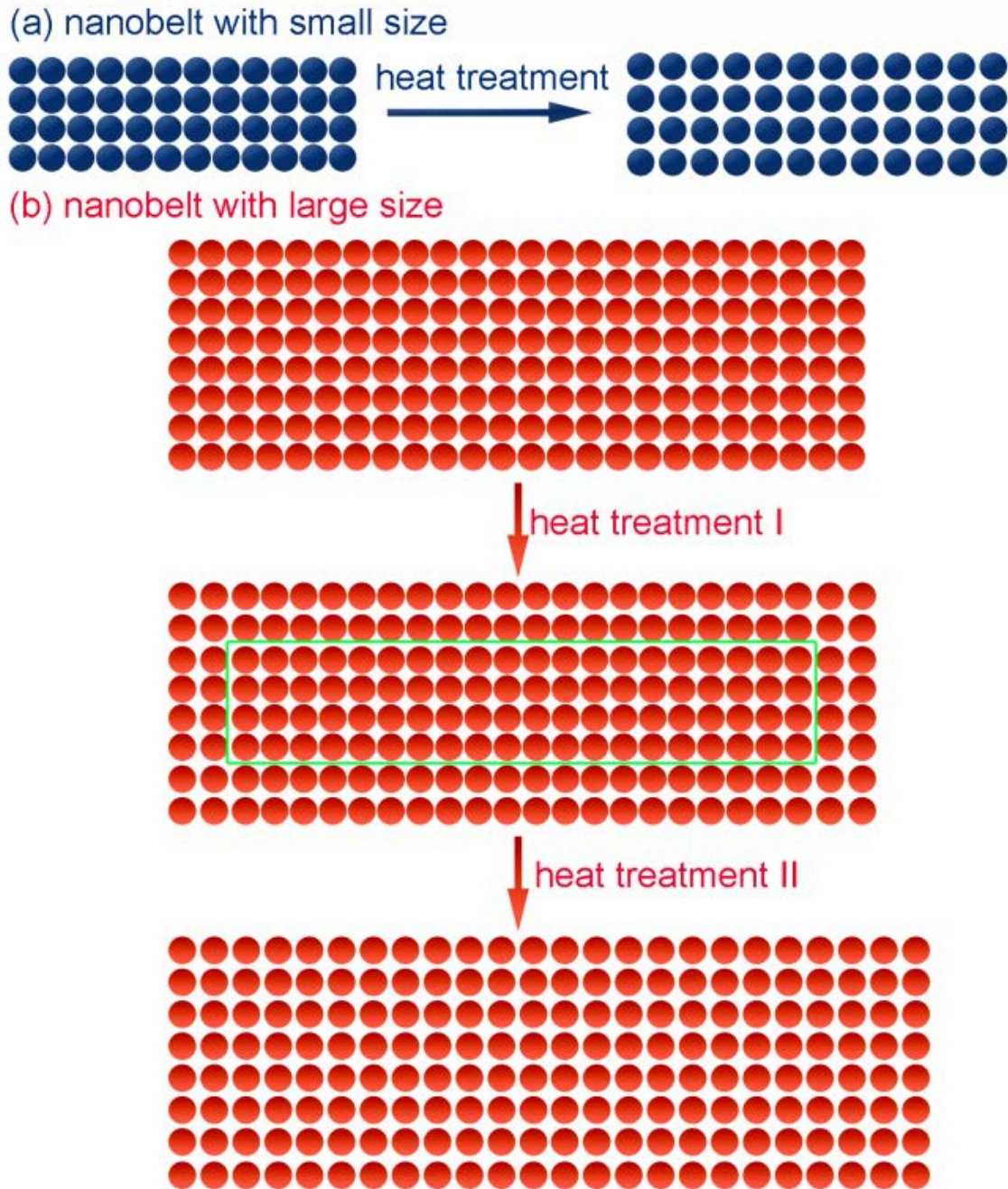
Figure 3.7 Schematics of thermal expansion in nanobelt with small and large size.

The thermal expansion in ZnO nanobelt behaves differently. The size plays a key role in thermal expansion coefficient of the ZnO nanobelt. For example, the width of the nanobelt at room temperature in Fig. 3.5a is only 36.14 nm, which increases to 36.53 nm at 100 °C. The corresponding thermal expansion coefficient is calculated to be 4.12×10⁻

44

[5]/K. The nanobelt in Fig. 3.2 is with width of 113.8 nm. The thermal expansion

coefficient is measured as 3.22×10^{-5}/K and 3.67×10^{-4}/K at 300 °C and 400 °C,

respectively.
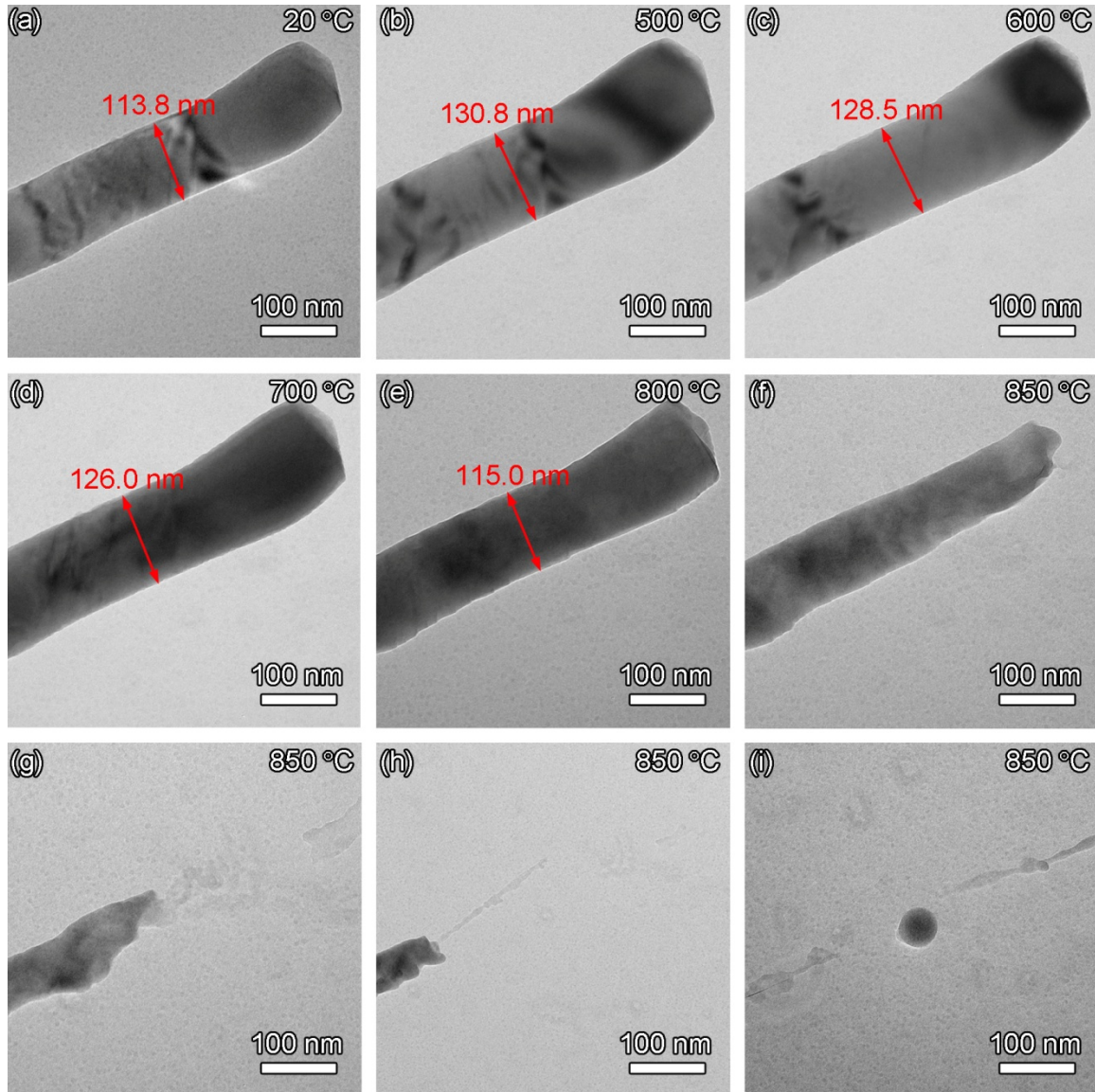
Figure 3.8 Melting of the ZnO nanobelt. TEM images of the ZnO nanobelt heated at (a) 20 °C, (b) 500 °C, (c) 600 °C, (d) 700 °C, (e) 800 °C, and (f-i) 850 °C, respectively. Each heating period is 2 min.

The width is one of the important parameters in thermal depression, and also the

thickness of the nanobelt can not be ignored. The ZnO nanobelt in Fig. 3.11 is with

thickness of 46.0 nm and width of 234.1 nm at room temperature. The ratio of thickness

to width of the synthesized ZnO is about one fifth. The thickness of the nanobelt in Fig.

3.5 and Fig. 3.2 might be about 7 and 23 nm, respectively, at room temperature. For ZnO

nanobelt with ultra small size, the constraint from neighboring atoms may be cut down.

All atoms can move simultaneously at a certain temperature shown in Fig. 3.7a.

However, not all atoms in the nanobelt with large size can move instantly when the

temperature increases. Only the surface atoms can take the action shown in Fig. 3.7b-heat

treatment I. With the energy accumulation, the subatoms would join in the expansion and

finally all atoms would move outward shown in Fig. 3.7b-heat treatment II. Such

mechanism is the reason why the nanobelt with ultra small size has a constant thermal

expansion coefficient and the nanobelt with large size possesses step-shape thermal

expansion coefficient. With the temperature increasing to 400 °C, the thermal expansion

coefficient suddenly jumps to 3.67×10^{-4}/K for large size ZnO nanobelt. However, the

ZnO nanobelt with 36.14 nm in width and 7 nm in thickness begins to melt around 200

°C.

Figure 3.8 shows the *in-situ* whole melting process of the ZnO nanobelt. The

original width of the ZnO nanobelt is 113.8 nm at room temperature shown in Fig. 3.8a.

Such value reaches 130.8 nm at 500 °C in Fig. 3.8b resulted from thermal expansion.

However, the width begins to decrease ~600 °C in Fig. 3.8c, which indicates that the ZnO

nanobelt does not expand any more, but melts instead. After 2 minute heating, the

temperature is increased to 700 °C in Fig. 3.8d, the width is cut down by another 2.5 nm.

With the temperature increasing to 800 °C, the ZnO nanobelt obviously melts shown in

Fig. 3.8e. The width drops to 115.0 nm. Moreover, the ZnO nanobelt is more transparent

under the electron beam than that in Fig. 3.8d, which shed insight on that the thickness of

ZnO nanobelt is decreasing as well. When the temperature increases to 850 °C, the ZnO

nanobelt melts promptly shown in Figs. 3.58-3.8h. Finally, the ZnO nanobelt becomes a

ball, and finally disappears. The melting point of the bulk ZnO is 1975 °C, while the

melting point of the ZnO nanobelt with thickness less than 50 nm is only ~600 °C. The

difference in the melting point between the ZnO nanobelt and the ZnO bulk is

surprisingly over 1000 °C. What is the mechanism behind this special phenomenon?
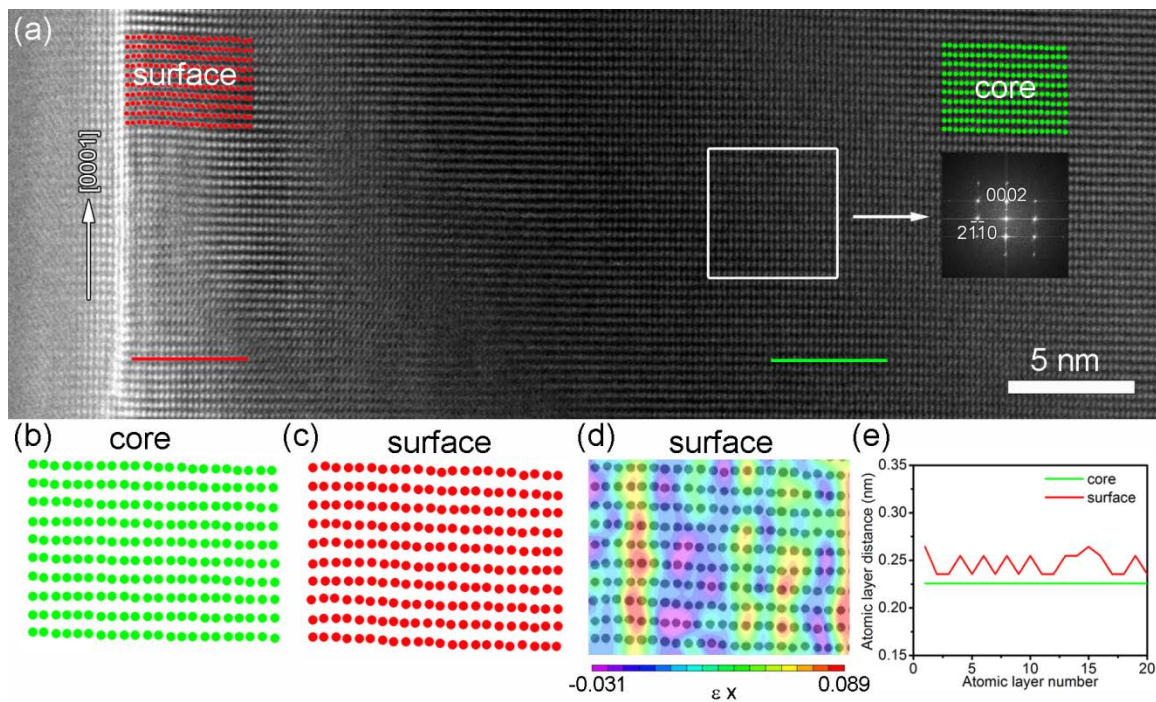
Figure 3.9 Structure and strain analysis of ZnO nanobelt. (a) High-resolution TEM image of the ZnO nanobelt. The inset is the fast Fourier transform (FFT) pattern indicating that the growth direction of the ZnO nanobelt is along the [0001] direction. (b) and (c) Schematics of atoms at core and surface, respectively. (d) Surface strain analysis along the cross-sectional direction of the ZnO nanobelt. (e) Lattice spacing profile in the surface and core along the cross-sectional direction of the nanobelt.

To the best of our knowledge, as the size of a solid particle reduces to nano-scale,

the surface-to-volume ratio will increase and the surface may exerts great influence on its

overall properties.[97] As a result, the melting point of the ZnO nanobelt can be determined

by both bulk melting point and surface melting point. In a simplified way, the melting

point of a ZnO nanobelt can be written as equation 3.5:

$$T_N = T_B \left(\frac{A_B}{A_{Tot}} \right) + T_S \left(\frac{A_S}{A_{Tot}} \right)$$
3.5

where T_N, T_B, and T_S refer to the melting points of the nanostructure, bulk, and surface,

respectively. A_{Tot}, A_B, and A_S represent the respective cross-sectional areas of the

nanostructure, bulk, and surface. Thus, the melting point of a 1-D nanostructure strongly

depends on the surface melting point. To confirm the above assumption of core/shell

melting process in the ZnO nanobelt, the lattice distance at surface and core along the

cross-sectional direction of the ZnO nanobelt was analyzed, respectively. The Digital

Image Correlation (DIC) was also employed to study the strain distribution in top 20

atomic layers. Figure 3.9 shows the structure and strain analysis in the ZnO nanobelt. Fig.

3.9a is the low-magnification TEM image of the nanobelt. The inset is the fast Fourier

transform (FFT) pattern indicating that the growth direction of the ZnO nanobelt is along

the [0001] direction. Two arrays of atoms at surface and core of the ZnO nanobelt were

highlighted in Fig. 3.9a. The corresponding schematics enlarged two times higher than

those original sizes are shown in Figs. 3.9b and 3.9c, which reveal the details of lattice at

core and surface in the ZnO nanobelt, respectively. The DIC analysis in Fig. 3.9d shows

the strain in ZnO nanobelt surface is not even, which is obtained by comparison between

core schematic in Fig. 3.9c and surface schematic in Fig. 3.9b. The alternative positive

and negative strain distribution at the surface may possibly induce melting at lower

temperature. The lattice spacing profiles in the core and surface layers along the cross-

sectional direction of the nanobelt highlighted by lines in Fig. 3.9a are plotted by

measuring the atomic distance between each two adjacent atoms using Photoshop

software. The lattice spacing of the ZnO nanobelt core is a constant. However, the lattice spacing of the ZnO nanobelt surface exhibits a wavelike characteristic shown in Figure 3.9e, indicating the existence of negative and positive surface strain. Such alternative negative and positive strain in the surface atomic layers along the radial direction of the nanobelt is in agreement with the DIC results. The surface can be thought as shell with alternative strain compared with the core. Moreover, the average lattice spacing at the surface is 0.2462 nm, which is higher than 0.2256 nm, the lattice spacing in the core. Such a difference confirms that the surface relaxation exists in ZnO nanobelts.

From a thermodynamic point of view, the bulk ZnO can be considered a thermodynamic system with constant pressure and temperature. The system energy can be expressed as equation 3.6:

$$G = U + P \cdot V - T \cdot S \qquad\qquad 3.6$$

where G is the Gibbs free energy and U, P, V, T, and S are the internal energy, pressure, system volume, absolute temperature, and system entropy, respectively. Apparently, the bulk ZnO can not transfer from solid to liquid spontaneously. An external energy source is required to make $G < 0$. With temperature increasing to the melting point of bulk ZnO, ΔG_b in Fig. 3.4 will be cut down to zero, which denotes that the atom in the bulk can jump out of potential well and get rid of the constraints from coordinated atoms. The corresponding temperature at the atom jumping out of the potential well is melting point. Such temperature can be written as equation 3.7:

$$T_b = \frac{\Delta U_b + P \cdot \Delta V_b - \Delta G_b}{\Delta S_b} \qquad\qquad 3.7$$

When the size of the ZnO is reduced to nano scale, the surface relaxation occurs in term of surface atoms moving outward shown in Fig. 3.4 (position 1), which is also proved by

first-principles DFT simulation.[97] The equilibrium bond length is not the original L in bulk, but $L+\Delta L$ instead. As the bond length increases, the bond energy will decrease resulting in the decrease of internal energy U. The Gibbs free energy of surface atom in the potential well is also cut off by ΔG, which makes the surface atom in the nanoscale ZnO more easily to jump out the potential well. The addition energy required to make the surface atom jump out is ΔG_n here. The temperature to drive $\Delta G_n < 0$ is the nanoscale ZnO surface melting point, which is shown in equation 3.8:

$$T_s = \frac{\Delta U_n + P \cdot \Delta V_n - \Delta G_n}{\Delta S_n} \hspace{3cm} 3.8$$

So the melting point of the ZnO nanobelt is determined by both core and shell melting points, which are bulk melting point (T_b) and shell melting point (T_s), respectively. The ZnO nanobelt melting point can be written as equation 3.1, where T_s may be much less than T_b, so the shell melting point will dominate the ZnO nanobelt melting point depression. With heat transferring to the ZnO nanobelt, the shell starts to melt first due to lower melting temperature compared with the nanobelt core. After the first several layers are gone, a new shell will generate and melt subsequently. Finally, the entire ZnO nanobelt melts out at relatively low temperature comparing the bulk ZnO.

To further confirm the thermal stability depression in the ZnO nanobelts, SEM and AFM were employed to check the morphology change of the ZnO nanobelts after heat treatment. The ZnO nanobelts were dispersed onto a silicon wafer. The observation and analysis using SEM are shown in Figure 3.10. First, the ZnO nanobelts were dispersed on a silicon wafer. Several nanobelts were located shown in Fig. 3.10a. The SEM image were taken at a working voltage of 20 kV, which is much lower than that of TEM voltage. It is noticed that the ZnO nanobelts were with 44.8 nm in width. SEM

analysis of the ZnO nanobelts showed that there is no observable change in the morphology upon heating at temperatures up to 450 °C. Some part began to miss which shows in Fig. 3.10b. For the nanobelts annealed at higher temperature, which is up to 550 °C shown in Figs. 3.10c and 3.10d, all three ZnO nanobelt morphology changed greatly. Some small particles on the right can be seen, resulted from the melting ZnO nanobelts condensing together when the temperature is down to room temperature. When the temperature is increased to 580 and 600 °C, half nanobelt on the left melt out and a big particle is shown as well when the temperature is down to 20 °C shown in Figs. 3.10e and 3.10f. As seen from Fig. 3.10, annealing at 600 °C induced partial melting of ZnO nanobelts, which also indicated that ZnO nanobelt with diameter less 100 nm can melt at the temperature of ~ 600 °C.
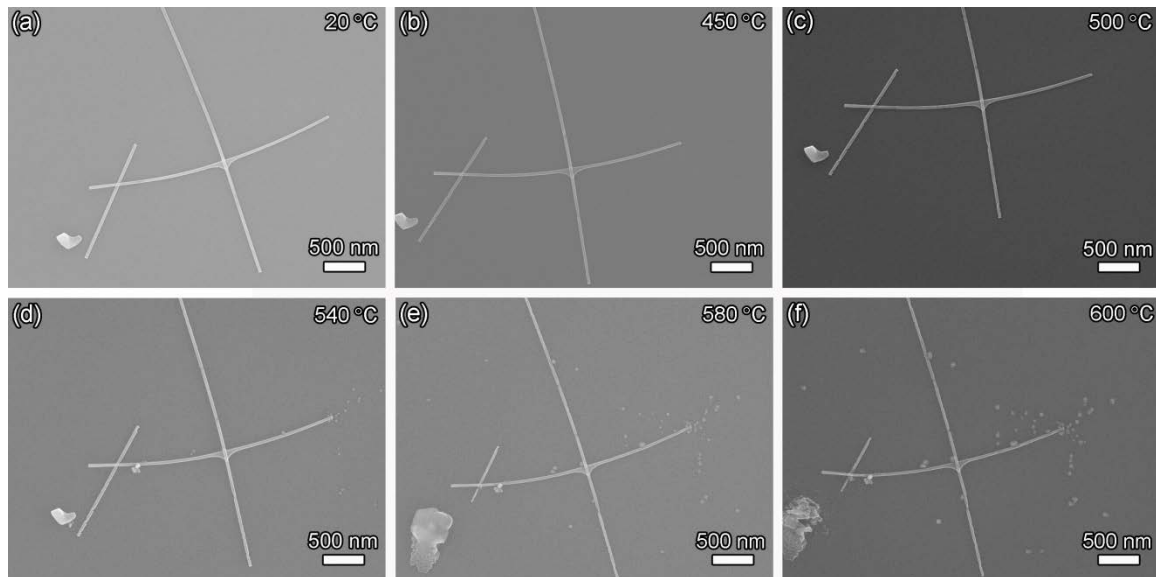
Figure 3.10 Morphologies of the ZnO nanobelts at different temperature. SEM images of the ZnO nanobelts heated at (a) 20 °C, (b) 450 °C, (c) 500 °C, (d) 540 °C, (e) 580 °C, and (f) 600 °C, respectively. Each time period is 2 h.

Figure 3.11 shows AFM images of an individual ZnO nanobelt heated at different temperature. The nanobelt in Fig. 3.11a at ambient condition is with width and thickness

of 234.1 nm and 46.0 nm, respectively. As the temperature increases to 400 °C in Fig.

3.8b, the width of the nanobelt increases to 257.1 nm, demonstrating 9.82% increase

comparing with it at room temperature. The thermal expansion coefficient at 400 °C is

calculated to be 2.46×10^{-4}/K, which is close to 3.67×10^{-4}/K obtained from *in-situ* TEM.

No diffusion is found in the ZnO nanobelt during thermal expansion. With temperature

increasing to 500 °C, the thickness of the nanobelt increases to the 51.5 nm shown in Fig.

3.11c. However, the width of the nanobelt is dropped to 208.8 nm. The width is 5 times

higher than the thickness of the nanobelt. The atoms on the side surface have less

constrains than those on the top surface, which results in that the side surface atoms may

easily jump out of the potential well and melt. While the top surface atoms are still

accumulating the energy and trying to jump out, leading to the thickness increase. As the

temperature further increases, the atoms at both side and top surfaces can jump out of the

potential well and melt. The width and thickness of the nanobelt at 550 °C is 204.6 nm

and 41.1 nm, respectively. The corresponding AFM image at such temperature is shown

in Fig. 3.11d. Another interesting phenomenon is that some small particles attach to the

side of the nanobelt, which is believe that the melted ZnO recrystallization occurs when

the temperature is down to room temperature. At 580 and 600 °C, the nanobelt melting

aggregates and the particle size increases from 57.4 nm at 550 °C to 191.2 nm at 580 °C

and then 994.3 nm at 600 °C shown in Figs. 3.11d and 3.11f, respectively. The width and

thickness of the nanobelt at 600 °C is 181.4 nm and 43.4 nm, demonstrating 22.5% and

5.7% reduction compared with those at 20 °C, respectively. Figs. 3.11g-3.11i show that

the thickness, width, and length of the ZnO nanobelt measured by AFM vary with the

temperature. It is clear that the thermal stability depression occurs in the ZnO nanobelt. The melting point may be down to ~550 °C.
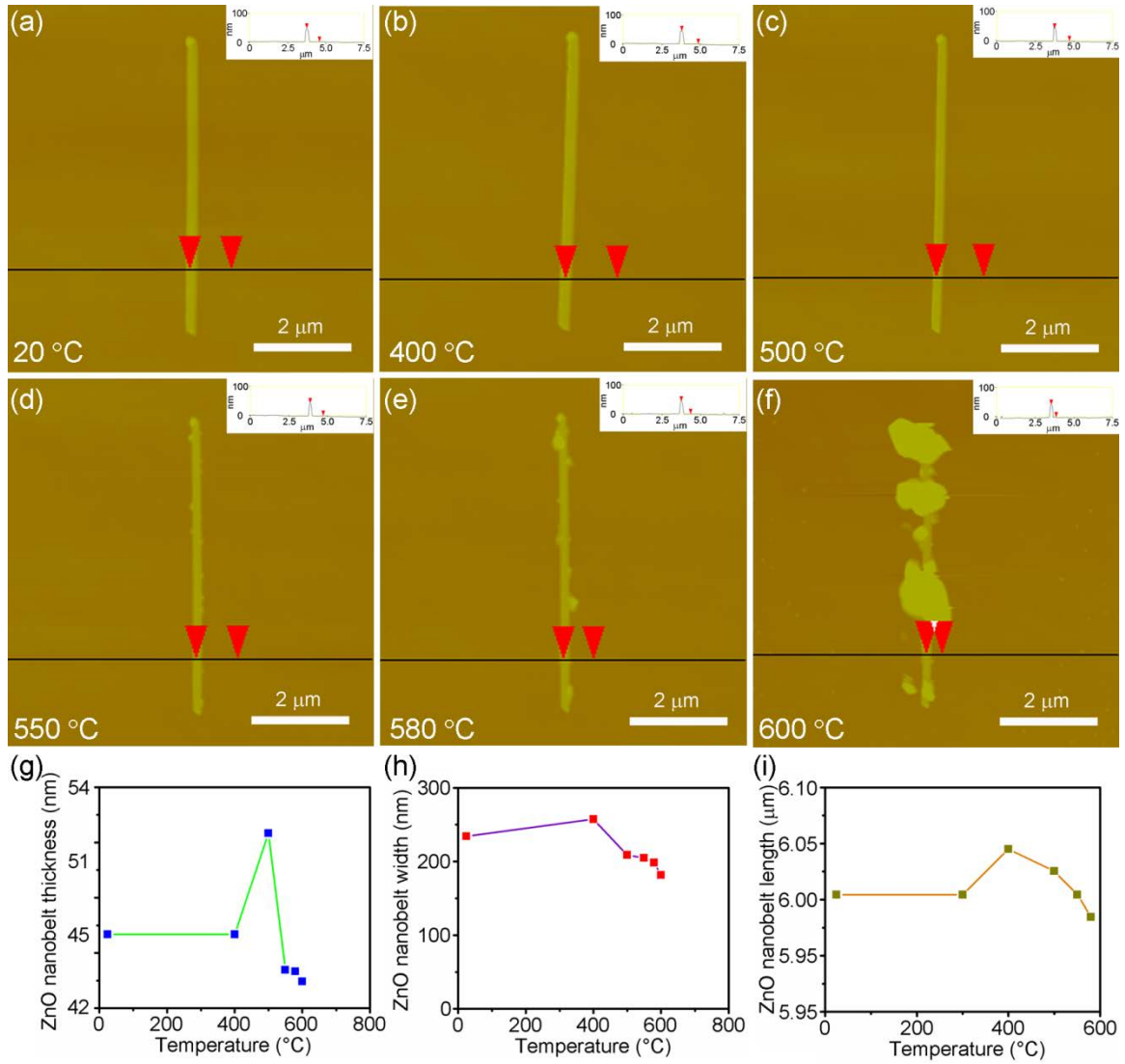
Figure 3.11 Thickness, width, and length of the ZnO nanobelt. AFM images of the ZnO nanobelt heated at (a) 20 °C, (b) 400 °C, (c) 500 °C, (d) 550 °C, (e) 580 °C, and (f) 600 °C, respectively. Each time period is 2 h. (g-i) Dependence of thickness, width, and length of the ZnO nanobelt on temperature.

3.3 SUMMARY

Significant thermal stability depression is found in the ZnO nanobelts. The

thermal expansion coefficient of the ZnO nanobelt at 400 °C is 3.67 $\times 10^{-4}$/K which is two

orders of magnitude higher than that of the ZnO nanobelt at room temperature. The nanobelt may melt at ~600 °C which is much lower than the melting point of the bulk ZnO. Both thermal stability changes in the ZnO nanobelts are confirmed by *in-situ* TEM, AFM, and SEM. The marked reduction in melting point for semiconductor nanocrystals has some potential applications. For example, the optimum annealing temperature for preparation of high-quality defect-free nanocrystals can be expected to be a small fraction of the bulk annealing temperature. However, as the dimension of active domains is reduced to the nanoscale, the issue of thermal stability of nanostructures cannot be ignored.

CHAPTER 4

DISPERSION OF MULTI-WALLED CARBON NANOTUBES

The exceptional mechanical, superior thermal and electrical properties of carbon nanotubes (CNTs) have made them promising for many engineering applications, such as composite reinforcements,[9-11] scanning probe tips,[149] field emission sources,[150] hydrogen storage systems,[151] super-capacitors,[152] quantum devices,[153] and biosensors.[154] A significant challenge for both fundamental research and practical applications of CNTs is to disperse CNTs into certain media, such as ethanol, water, or polymers. Since CNTs are insoluble and tend to form bundles due to their strong hydrophobicity and van der Waals attractions, a great deal of effort has been invested to develop efficient and low-cost approaches to realize full dispersion of CNTs.

Approaches can be divided into two categories, namely mechanical dispersion and surface modification.[155] Mechanical methods, such as ultrasonication, high shear mixing, and ball milling, have been commonly employed to disperse one kind of material into another, including CNTs. The shear mixing approach uses a shear force produced by air flow in conjunction with a rapidly moving fluid to disperse and align CNTs. The torque produced by the shear force can make CNTs aligned and straightened along the axial direction.[156] Although the shear mixing method is faster in aligning CNTs, only a marginal proportion of CNTs were completely separated. Ultrasonication and ball milling can also be used to disperse CNTs in solutions or polymers. These two methods are easy to operate but usually take long time to disperse CNTs with low-efficiency. During

55

intensive ultrasonication and ball milling, CNT fracture failure often occurs, which destroys the integrity of the dispersed CNTs. Surface modification can be either chemical or physical. Chemical surface modification enables the CNT surface to be functionalized through reactions with atoms or molecules such as fluorine, alkanes, or by ionic modification to improve their chemical compatibility. Wetting or adhesion characteristics of CNTs can be altered through functionalization to reduce their tendency to agglomerate. For example, an amine group or dangling amine moieties can easily form amide bonds by interacting with carboxylic groups located at the ends, sidewalls, and defect sites of the oxidized CNTs and further induce the formation of salt.[110,157,158] This method has been proven to be effective in terms of making CNT solution stable and preventing them from aggregating in the solution state. However, such dispersed CNTs tend to clump together after drying. Physical surface modification is the noncovalent stabilization of CNTs by interaction with certain solvents, such as surfactants, polymers, and biomolecules.[112,159,160] For instance, sodium dodecylbenzene sulfonate was used as surfactant to assist the dispersion of CNTs.[159] A major drawback of both chemical and physical surface modifications is that impurity is often introduced into the CNT solution, such an impurity is difficult to remove in further processes or applications.

Surface passivation has been widely used to treat semiconductor materials to minimize the surface contribution of the semiconductors to the electrical properties of the device.[114,161-163] For example, it is well-known that hydrogen can interact with the dangling bonds (DBs) of Si to form Si-H bonds and thus passivate the density surface of Si, which is primarily in the form of DBs and harmful to Si device performance.[114, 162] In fact, CNTs formed from a graphene sheet also have DBs due to the unclosed shells with

rather waving flakes that follow the curvature of the tubes and create many open edges on the surface.[164] These DBs provide CNTs with a high chemical activity and the probability to uptake hydrogen, which can be used to passivate CNTs for the dispersion purpose. Hydrogen atoms absorbed by CNTs can be either in the physisorption state, where the hydrogen molecules are bonded with the exterior CNTs surface via weak van der Waals interaction, or in the chemisorption state, where a hydrogen atom is chemically bonded with a carbon atom of the CNTs.[165] However, to the best of our knowledge, there are no reports on dispersion of CNTs using hydrogen passivation (HP).

In this chapter, a novel method combining ultrasonication and HP was developed to disperse multi-walled carbon nanotubes (MWCNTs) in both ethanol solution and the epoxy resin. Hydrogen binding to MWCNTs was extremely effective and facile. Excellent dispersion of MWCNTs was achieved in both media. Mechanical characterization was performed on individual dispersed MWCNTs by atomic force microscopy (AFM) to measure the elastic modulus of such dispersed MWCNTs. Three-point bending tests of the MWCNT/epoxy nanocomposites produced revealed a remarkable increase in elastic modulus with increasing MWCNT content, suggesting that such coupled HP and mild ultrasonication approach holds a great promise to achieve the theoretically predicted potentials of CNTs in their composites.

4.1 EXPERIMENTAL

The MWCNTs used in this study were two millimeter-long well-aligned MWCNT sheets with a thickness of 10–20 μm. To disperse the MWCNTs in absolute ethanol, ~0.001g MWCNTs were first immersed into 1 ml ethanol (Sigma-Aldrich) in a

glass bottle. Then the glass bottle was put into the basin of an ultrasonicator (Branson 5510, Branson Ultrasonic Corp., CT, USA). Ultrasoncations were done in two ways, namely with the inlet hydrogen (HP) and in ambient environment. The hydrogen gas was produced by reaction of zinc powder (Sigma-Aldrich) and 0.1 mol/L hydrochloric acid (Fisher Corp.). This gas passed a long steel tube to eliminate any hydrochloric acid vapor.

One drop of the solution was taken out from the glass bottle after 15 min, 30 min, 1 h, and 2 h ultrasonication, and dropped down onto the silicon wafer coated by 20 nm gold film, and the copper grid, respectively, for future study. Scanning electron microscopy (SEM; Zeiss Ultra plus Field Emission Gun (FEG)-SEM) and transmission electron microscopy (TEM; Hitachi H-8000-TEM) were used to examine the effects of the dispersion. To determine the C-H bonds, X-ray photoelectron spectroscopy (XPS; Kratos Axis Ultra DLD) was employed to characterize the CNTs dispersed with and without HP.

To produce MWCNT/epoxy composite, MWCNTs were first dispersed in epoxy resin, EPO-TEK 302-3M Part A, (Epoxy Technology, MA, USA) with 2 h ultrasonication under HP. Then the hardener, EPO-TEK 302-3M Part B, (Epoxy Technology, MA, USA) was added to the epoxy resin and the mixture was stirred for 30 minutes and cured for 24 hours under ambient condition. The weight proportion of epoxy resin to hardener was 100 to 45 as suggested by the manufacturer. Two epoxy composites reinforced with 0.35 wt.% and 1.0 wt.% MWCNTs were produced in this study. A control sample with 0 wt.% MWCNTs was also fabricated. Fresh cleavage surfaces of both MWCNT/epoxy composites and the control sample were observed to check the morphology and dispersion of the MWCNTs using SEM.

A drop of the ethanol solution with well dispersed MWCNTs was dropped onto a standard AFM reference sample (NGR-21010, Veeco Metrology Group, NY, USA) with uniform trenches. Individual MWCNT that bridges a trench was located under SEM. Carbonaceous materials (Alfa Aesar) were deposited on both ends of the MWCNT by electron-beam induced deposition to clamp the MWCNT to prevent any sliding of the MWCNT during the three-point bending test. The bending test was performed by directly indenting the center of the suspended MWCNT with a tapping mode silicon tip using a Veeco Dimension 3100 AFM (Veeco Metrology Group, NY, USA). During the test, both applied bending load and the corresponding deflection of the MWCNT was recorded and the initial loading curve was used for the elastic modulus analysis.
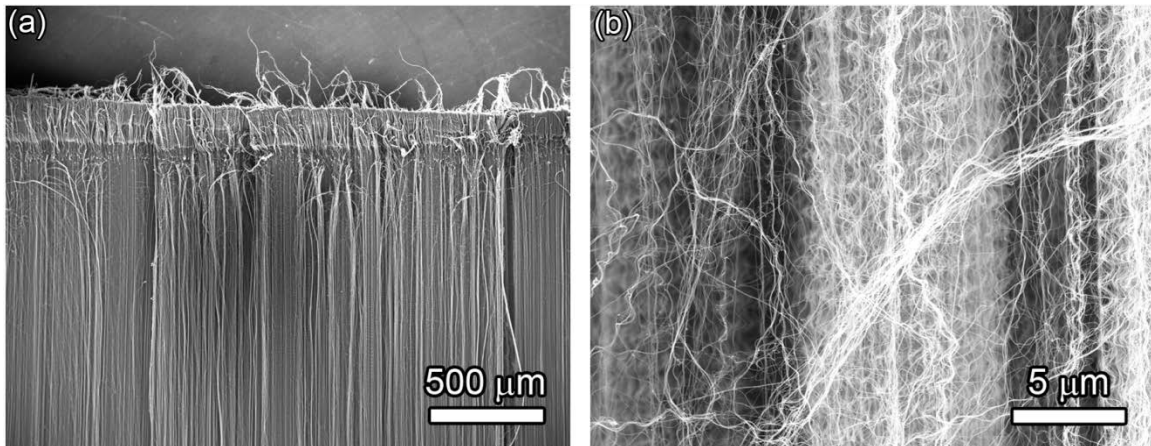
Figure 4.1 (a) Low and (b) high magnification SEM images of an aligned MWCNT sheet.

To measure the elastic modulus of the MWCNT/epoxy composites, three-point bending test was also performed on two composites with 0.35 wt.% and 1 wt.% MWCNTs produced in this study using microtribometer (CETR Inc., CA, USA). The control sample was also tested for comparison. For each material, six beam samples with the dimension of $30 \times 3 \times 3$ mm (length × width × height) were tested. The elastic

modulus of the tested materials was calculated from the initial linear portion of the loading curve of the three-point bending test.

4.2 RESULTS AND DISCUSSION
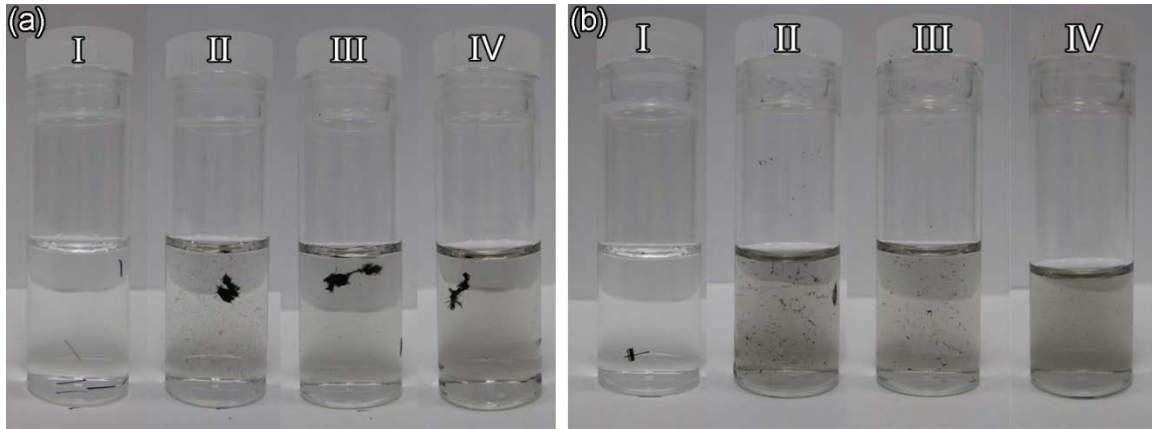
Figure 4.2 Optical images of dispersed MWCNTs with (a) ultrasonication only and (b) coupled HP and ultrasonication for different dispersion time periods, 0 h (I), 0.5 h (II), 1 h (III), and 2 h (IV).

The MWCNTs used in this study were two millimeter-long well-aligned MWCNT sheets with a thickness of 10–20 μm.[166,167] Representative SEM images of bundled MWCNTs shown in Figure 4.1 in curved morphology indicate that MWCNTs have good flexibility. Figure 4.2 shows the optical images of the dispersed MWCNTs in absolute ethanol with ultrasonication only (Fig. 4.2a) and with coupled HP and ultrasonication treatment (Fig. 4.2b). The images were taken after different dispersion time periods, namely 0 h (I), 0.5 h (II), 1 h (III), and 2 h (IV). For dispersion with ultrasonication only (Fig. 4.2a), majority of the MWCNTs tended to agglomerate and formed floccules in the ethanol solution while only a marginal part of the MWCNTs truly dispersed in the solution, making the solution darker in color. However, for dispersion with coupled HP and ultrasonication (Fig. 4.2b), the MWCNTs were well dispersed in the

solution after HP and 2 h ultrasonication, no MWCNT floccules were found in the

ethanol solution, as shown in Fig. 4.2b-IV.
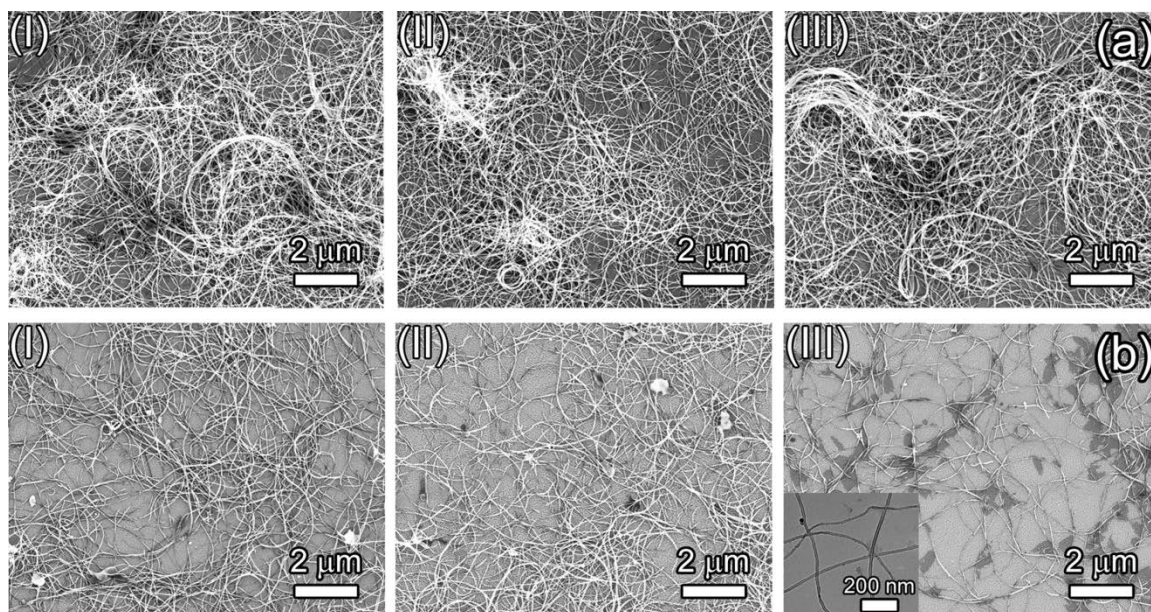
Figure 4.3 SEM images of dispersed MWCNTs with (a) ultrasonication only and (b) coupled HP and ultrasonication for different dispersion time periods, 0.5 h (I), 1 h (II), and 2 h (III).

Figure 4.3 shows the SEM images of the MWCNTs dispersed in ethanol solution

after 0.5 h (I), 1 h (II), and 2 h (III) ultrasonication treatment without (Fig. 4.3a) and with

(Fig. 4.3b) HP . Without HP, the dispersed MWCNTs in ethanol were still agglomerated

together even after 2 h ultrasonication (Fig. 4.3a-III). It is very difficult to manipulate

these MWCNT bundles and perform mechanical tests on individual MWCNTs.

Contrarily, dispersion of the MWCNTs with HP shows a completely different result. As

shown in Fig. 4.3b, with increasing ultrasonication time, the MWCNTs started to separate

from one another and no MWCNT bundles were found. An excellent dispersion of the

MWCNTs was achieved for 2 h ultrasonication (see Fig. 4.3b-III). The insert in Fig.

4.3b-III, TEM image, also provides evidence for individually dispersed MWCNTs with

coupled HP and 2 h ultrasonication. The diameter of the individual MWCNTs is approximately 30 nm. Clearly, almost all the MWCNTs were separated in ethanol solution and can be easily manipulated and tested using AFM to probe their mechanical properties.
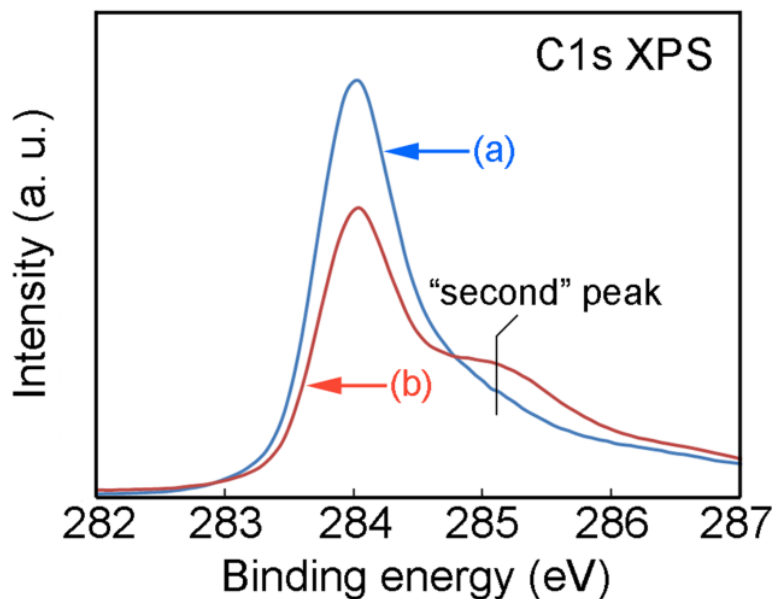
Figure 4.4 C1s XPS spectra of dispersed MWCNTs with (a) ultrasonication only and (b) coupled HP and ultrasonication for 1 h dispersion.

To shed light on the mechanism of HP induced MWCNT dispersion, the interaction between the MWCNT and the hydrogen atoms was proposed and also studied in details. Two critical barriers need to be overcome in MWCNT dispersion, i.e., the van der Waals force between MWCNTs and the C-C bonds formed in the dangling bonds of MWCNTs. Compared to the C-C bonding, the van der Waals force between MWCNTs is rather weak and easy to overcome. Therefore, the key to separate the MWCNT bundles is to make the dangling C- bonds form new more stable bonds with other atoms. The inlet hydrogen serves as a source of the second atoms to form more stable C-H bonds. The following reaction occurs during the HP.

$$C - C + H_2 \rightarrow 2C - H \qquad\qquad 4.1$$

Since the bond energy is 347 kJ/mol for C-C, 436.2 kJ/mol for H-H, and 416.3 kJ/mol for C-H, it is clear that additional energy is needed so that the reaction (4.1) can proceed. This additional energy is provided by the sound energy produced by the ultrasonication treatment. To prove whether the sound energy is enough to break hydrogen bond, we give the calculation. The hydrogen bond energy is 436 KJ/mol. The required frequency to break the individual hydrogen bond is calculated as follows:

$$E_e = \frac{2\pi \hbar c}{\lambda} \qquad\qquad 4.2$$

$$\lambda = \frac{c}{f} \qquad\qquad 4.3$$

where E_e, $\hbar$, c, λ, and f are energy, reduced Plank constant, speed of light, wavelength, and frequency, respectively. The required frequency is 1.09×10^{15} Hz which is much higher than 40 kHz for ultrasonication. Therefore, the ultrasonication can not provide enough energy to break the individual hydrogen bond. However, the hydrogen does attach on CNTs based on the XPS analysis. The question is how it occurs? Actually, the attached hydrogen is H_2, not free charged hydrogen. The constant vibrational motion provided by ultrasonication can cause distortions of electrical symmetry in H_2.[168,169] The asymmetric H_2 can attach on carbon dangling bonds in CNTs. As shown in Figure 4.4, hydrogen interaction led to a dramatic change in the C1s peak shape. For HP (b), an additional C1s peak was recognized as a shoulder at higher binding energy compared to the C1s peak for ultrasonication only (a). This observed binding energy shift between the main peak and the second peak for HP was in accordance with the chemical shift between

63

sp² and *sp³* hybridized carbon species in MWCNT[170] and due to attachment of hydrogen to the C dangling bonds resulting in C-H bond formation.[171]

The dispersion process of MWCNTs in HP is schematically shown in Figure 4.5. The MWCNTs tend to form bundles due to the van der Waals interaction between individual MWCNTs and the C-C bonds formed in the dangling bonds. Upon ultrasonication, MWCNTs will be agitated by the applied sound energy from ultrasonication. When the applied sound energy is high enough to overcome the van der Waals force and break the C-C bonds in the MWCNTs, the MWCNT bundles start to debond and disperse into the media. If there is no inlet hydrogen during the ultrasonication, the dangling C- bonds formed from the broken C-C bonds may rebind with nearby dangling C- bonds when the ultrasonication is stopped. This will lead to rebundling of the MWCNTs. However, hydrogen reacts with the dangling C- bonds, forming more stable C-H bonds. This passivates the MWCNTs and prevents them from bundling together through the formation of the C-C bonds[171] during and after ultrasonication so that excellent dispersion of MWCNTs can be achieved.
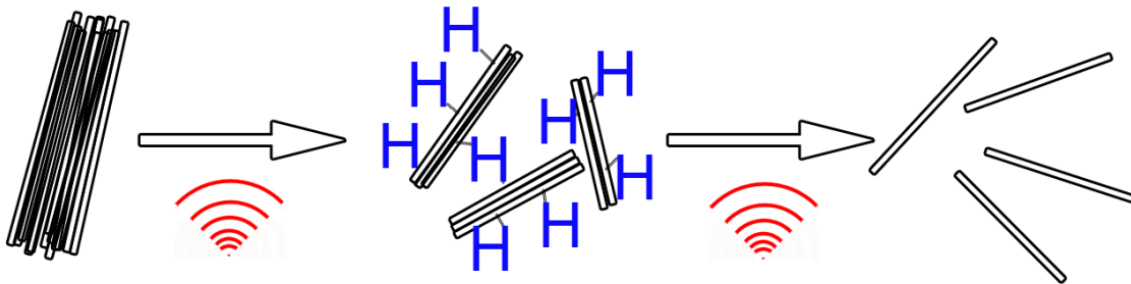
Figure 4.5 Schematic of MWCNT dispersion process with coupled HP and ultrasonication.
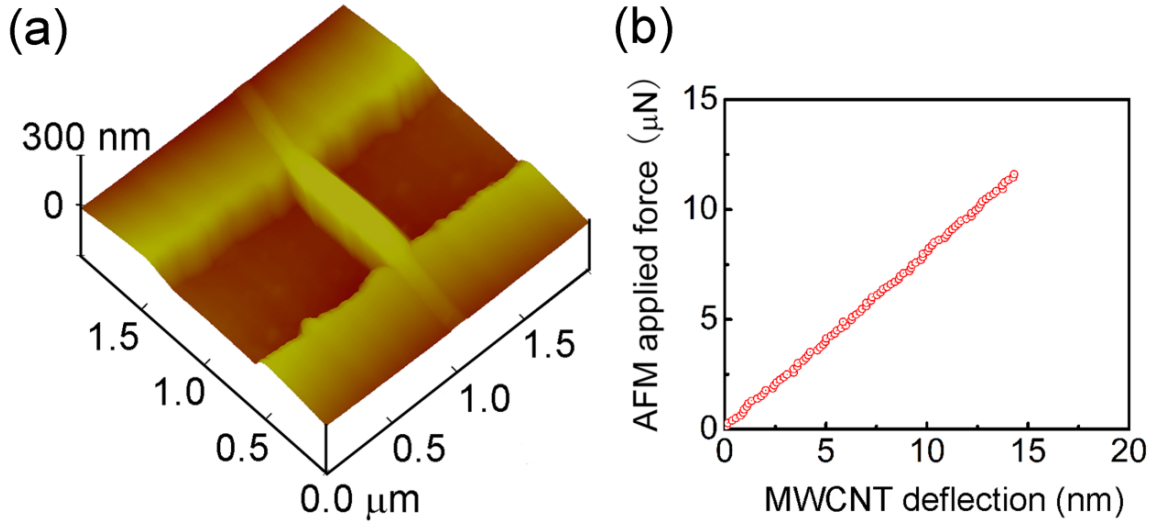
Figure 4.6 (a) 3D AFM image showing a MWCNT over the trench on the Si wafer. (b) Applied bending force as a function of net MWCNT deflection.

Compared to the conventional dispersion methods, the coupled HP and ultrasonication method developed in this study has several significant advantages. The new method is very efficient in dispersing MWCNTs. Excellent dispersion of MWCNTs can be achieved with only 2 h ultrasonication after HP, which is much shorter than the conventional ultrasonic method that requires at least 10 h.[173] This method offers opportunities for dispersing a series of materials which tend to bundle together due to dangling bond, such as graphene. Unlike other surface modifications, where MWCNT surface is functionalized by the reactions with atoms or molecules such as fluorine, alkanes, HP adds no impurities that may affect the further application of the dispersed MWCNTs. In fact, the hydrogen adsorbed in MWCNTs can be released at temperature around 600 °C[171] so that none impurities would remain in MWCNTs.

To investigate whether our coupled HP and ultrasonication dispersion method impaired the dispersed MWCNTs, mechanical characterization of both individual dispersed MWCNTs and the MWCNT/epoxy nanocomposites was carried out. AFM

three-point bending tests were performed on individual MWCNTs as shown in Figure 4.6a. An initial portion of a typical bending force-deflection curve is shown in Fig. 4.6b. The linear relationship between the bending force and the deflection of the MWCNT indicates an elastic deformation. The elastic modulus can be calculated from the linear portion of the bending-deflection curve using the following equation.

$$E = \frac{KL^3}{192I} \qquad\qquad 4.4$$

where I, L, and K are the moment of inertia, the suspended length, and the slope of the initial bending force-deflection curve, respectively. The average elastic modulus of the MWCNTs measured by AFM three-point bending is 774 ± 33 GPa. This agrees well with the reported values in literature ranging from 0.3 to ~1 TPa[149,155,174] suggesting that the coupled HP and ultrasonication treatment did not damage the MWCNTs' integrity.
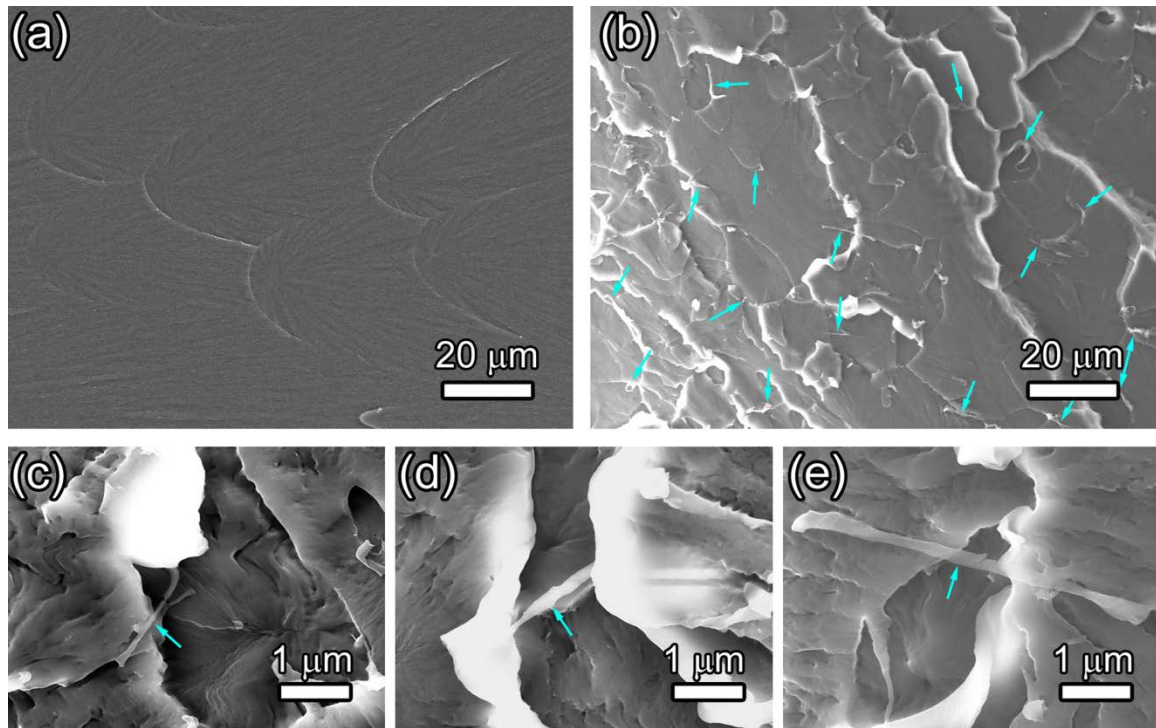
Figure 4.7 (a) SEM image of pure epoxy resin. (b) Low magnification SEM image of the MWCNTs well-dispersed in epoxy resin. (c-e) High magnification SEM image of individual MWCNTs well-dispersed in epoxy resin.

Figure 4.7 shows the SEM images of the fresh cleavage surfaces of a pure epoxy resin sample and an MWCNT/epoxy nanocomposite sample. Compared to the smooth fractured surface of the pure epoxy (Fig. 4.7a), the nanocomposite is rough and consists of many small facets (Fig. 4.7b). This is expected since the MWCNTs in the nanocomposite highlighted by the arrows in Fig. 4.7b are randomly distributed in and well bonded with the epoxy matrix. These MWCNTs inhibit fracture of the nanocomposite and thus result in a rougher cleavage surface. Figs. 4.7c-4.7e show the high magnification SEM images of individual MWCNTs dispersed in epoxy matrix. As can be seen, the MWCNTs, treated by the developed coupled HP and ultrasonication method, were well dispersed in epoxy matrix.
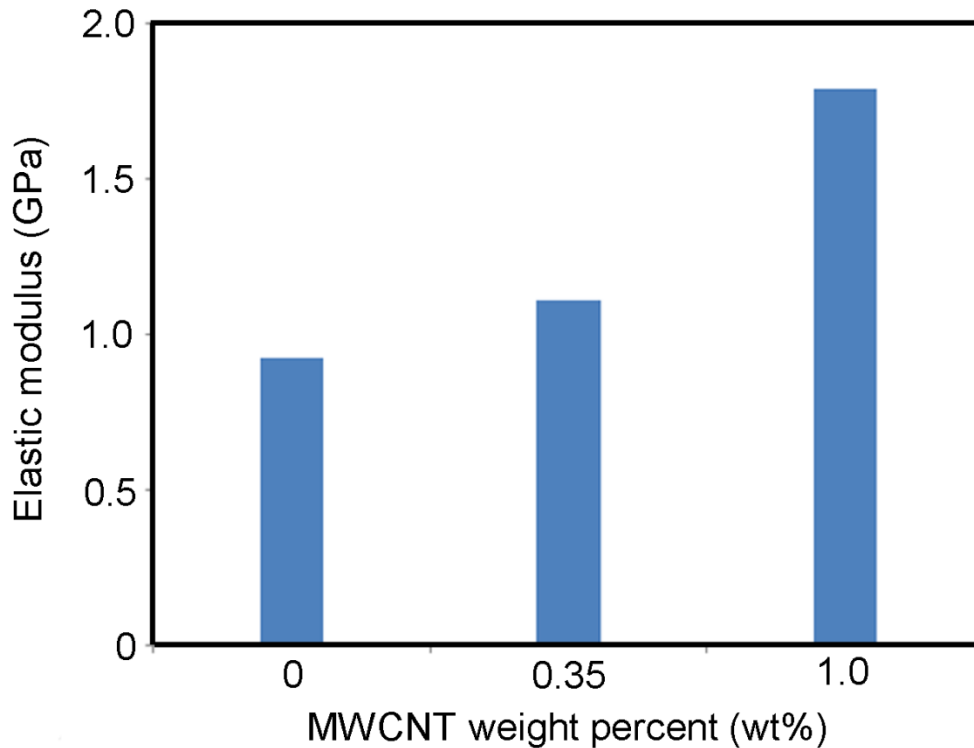
Figure 4.8 Variation of elastic modulus with MWCNT percentage for MWCNT/epoxy composites.

Table 4.1 Elastic modulus increase of selected 1 wt.% CNT/polymer composites

CNT	Matrix	Elastic modulus (GPa)		E increase %	Reference
		Control sample	composite		
DWCNT	Epoxy resin	3.29	3.51	6.62	[11]
MWCNT	Phenylethynyl	2.84	3.07	8.10	[10]
MWCNT	Polystyrene	2.35	2.59	10	[175]
SWCNT	Epoxy resin	3.79	4.54	19.8	[176]
MWCNT	Phenolic	5.12	6.50	26.9	[9]
CNT	Epoxy resin	1.65	2.15	30	[177]
MWCNT	Polyethylene	0.98	1.36	38.4	[178]
MWCNT	Epoxy resin	0.92	1.79	94.57	This study

The elastic modulus of the MWCNT/epoxy nanocomposites determined by three-point bending test is shown in Figure 4.8. As expected, the elastic modulus of MWCNT/epoxy composites increases with increasing MWCNT content. The elastic modulus of the control sample (pure epoxy) is 0.92 ± 0.05 GPa. The elastic modulus values of the 0.35 wt.% and 1 wt.% MWCNT reinforced nanocomposites are 1.11 ± 0.04 GPa and 1.79 ± 0.10 GPa, respectively, demonstrating 20% and 94.57% increase compared to the control sample. The mechanical properties of CNT/epoxy nanocomposites are determined by many factors such as the type and content of CNTs, the structure and properties of matrix, the dispersion of CNTs in the matrix, and CNT/matrix interfacial bonding. For comparison, Table 4.1 summarizes the increased values of elastic modulus for 1 wt.% CNT/polymer composites achieved by different research groups. The increased values in elastic modulus range from 6.62% to 38.4%.[9-11,175,178-180] The 1 wt. % MWCNT/epoxy nanocomposite fabricated by our coupled HP

and ultrasonication dispersion method exhibits a surprisingly high increase in elastic

modulus of 94.57%, 2.5 times higher than the reported values in literature.

4.3 SUMMARY

A method for dispersing MWCNTs has been developed by coupling HP and

ultrasonication and successfully applied to disperse MWCNTs into absolute ethanol and

epoxy resin media. SEM observation revealed that excellent dispersion of MWCNTs has

been achieved in both media with 2 h untrasonication after HP. Three-point bending tests

have been performed on both dispersed MWCNTs and the MWCNT/epoxy composites.

The elastic modulus of the individual MWCNTs is 774 ± 33 GPa. The elastic modulus

values of the 0.35 wt.% and 1 wt.% MWCNT/epoxy composites are 1.11 ± 0.04 GPa and

1.79 ± 0.10 GPa, respectively.

CHAPTER 5

PUSHING UP GRAPHENE REINFORCING LIMITS IN COMPOSITES

Exceptional physical properties, high aspect ratio and low density of graphene have made it an ideal candidate for developing the next generation of polymer composites.[181-185] Graphene, as the strongest material ever measured, is known to have a Young's modulus of 1 TPa and intrinsic strength of 130 GPa. Such values are 5 and 20 times greater than those for steel, respectively, at just 1/3 the weight.[179,186-188] Thus, graphene sheets are expected to serve as mechanical reinforcements for lightweight composite systems. However, graphene has largely disappointed us in manufacturing lightweight, high strength polymer composites because of graphene sheet agglomeration in the matrix - one of the major roadblocks limiting its reinforcing effect and applications.[115,116] The mechanical properties of graphene reinforced polymer composites are considerably below their theoretically predicted potential.[117] A common observation from previous studies is that the magnitude of improvement is, to a large extent, dependent upon the state of dispersion of graphene sheets in the matrix. Only when graphene sheets are homogeneously dispersedwithin the matrix, the enhancement could be more significant. Graphene sheets often aggregate into flakes of weakly interacting monolayered sheets due to its strong hydrophobicity and van der Waals attraction.[118] One flake can contain up to several hundred monolayered sheets.[119,120] The monolayered sheets within a flake can easily slide over each other and the shear modulus of graphene flakes is relatively low.[121]

In addition, the aggregates of graphene sheets dramatically reduce the aspect ratio of the reinforcement.

It has been shown that harvesting well-dispersed graphene is challenging. Although chemical functionalization of graphene sheets may reduce their agglomeration tendency to some extent.[115,122-124] the major drawback of chemical surface modification is that impurity is often introduced into the graphene based composites and the presence of foreign stabilizers is undesirable and difficult to remove in further processes.[189] Many researchers have turned their attention to derivatives of graphite, especially graphite oxide, which is hydrophilic and has a larger interlayer distance than graphite.[126,190-192] Individual graphene oxide sheets can be produced in water more easily than monolayered graphene sheets, and such graphene oxide sheets may form stable dispersion after ultrasonication. Posterior deoxygenation is able to restore electrically insulating graphene oxide to conductive graphene, but many of the resultant sheets are crumpled and wrinkled.[127] New strategies to produce monolayered graphene sheets without destroying their unique structural integrity are in a pressing need. Surface passivation has been proven to be one of most effective methods to disperse multi-walled carbon nanotubes (MWCNTs) in both absolute ethanol and epoxy.[193] The inlet hydrogen atoms serve as a source of the second atoms to occupy the dangling C-bonds in MWCNTs, forming more stable C-H bonds.[164] The dangling bonds provide graphene with high chemical activity and the possibility to uptake hydrogen.[194] which may be used to passivate the surface of graphene, thereby achieving excellent dispersion.[195]

Here we limit our focus to graphene reinforced composites fabricated by the coupled hydrogen passivation (HP) and ultrasonication dispersion method. Atomic force

microscopy (AFM), which has been proven to be the most effective method to visualize dispersed graphene sheets, was employed to evaluate the thickness of the graphene sheets after 2 hours of dispersion assisted by ultrasonication only and the coupled HP and ultrasonication, respectively. Three-point bending tests of the graphene/epoxy composites fabricated by the coupled HP and ultrasonication technique revealed remarkable increases in elastic modulus, fracture strength, and fracture energy with an increase in graphene concentration. We demonstrate that the reinforcing limits of graphene composites can be further pushed up by the coupled HP and ultrasonication technique, which overcomes the roadblock and creates opportunities for taking advantages of the structural uniqueness and exceptional mechanical prowess of graphene in its applications.

5.1 EXPERIMENTAL

The average flake thickness of the graphene sheets (Graphene Supermarket, NY, USA) used in this study was 12 nm. The specific surface area was about 80 m^2/g. To disperse the graphene sheets in absolute ethanol, graphene sheets (~0.001g) were first immersed into ethanol (1 ml, Sigma-Aldrich) in a glass bottle. Then the glass bottle was put into the basin of an ultrasonicator (Branson 5510, Branson Ultrasonic Corp., CT, USA). Ultrasoncation was carried out in two ways, namely with the inlet hydrogen (HP) and in ambient environment. The hydrogen gas was produced by the reaction of zinc powder (Sigma-Aldrich) and hydrochloric acid (0.1 mol/L, Fisher Corp.). This gas passed through a long steel tube to eliminate any hydrochloric acid vapor.

A silicon wafer was cleaned by acetone and ethanol successively in an ultrasonicator. Each process was performed for 5 min. A drop of the ethanol solution

containing dispersed graphene sheets without HP was then dropped onto the silicon wafer. Another drop of the ethanol solution containing dispersed graphene sheets with HP was dropped onto the fresh surface of Mica (Jupiter Commercial Company, Kolkata, India). The thickness of dispersed graphene sheets by both ultrasonication only and coupled HP and ultrasonication was measured by a Veeco Dimension 3100 AFM (Veeco Metrology Group, NY, USA) with a tapping mode silicon tip. 50 images obtained at random locations were used to analyze the thickness distribution for both dispersion methods. Scanning electron microscopy (SEM; Zeiss Ultra plus Field Emission Gun (FEG)-SEM) was used to examine the dispersed graphene sheets on silicon and Mica substrates. To determine the C-C and C-H bonds, X-ray photoelectron spectroscopy (XPS; Kratos Axis Ultra DLD) was employed to characterize the graphene sheets dispersed with and without HP.

To produce graphene/epoxy composites, graphene sheets were first dispersed in epoxy resin, EPO-TEK 302-3M Part A, (Epoxy Technology, MA, USA) with 2 h ultrasonication under HP. Then the hardener, EPO-TEK 302-3M Part B, (Epoxy Technology, MA, USA) was added to the epoxy resin and the mixture was stirred for 30 minutes and cured for 24 hours under ambient condition. The weight proportion of epoxy resin to hardener was set to 100 to 45 as suggested by the manufacturer. Four kinds of epoxy composites reinforced by 0.5 wt.% and 1.0 wt.% graphene sheets with and without HP treatment were fabricated in this study. A control sample without any graphene was also prepared for comparison. Fresh cleavage surfaces of both graphene/epoxy composites and the control sample were observed using SEM to examine the morphology and dispersion of the graphene sheets. To measure the elastic modulus and fracture

strength of the graphene/epoxy composites, three-point bending tests were performed on all four kinds of the composites reinforced with 0.5 wt.% and 1.0 wt.% graphene sheets with and without HP treatment using a microtribometer (CETR Inc., CA, USA). The control sample was also tested for comparison. For each composite, five beam samples with the dimension of $20 \times 2.5 \times 2.0$ mm (length $\times$ width $\times$ height) were tested. The elastic modulus of the tested composites was calculated from the initial linear portion of the three-point bending loading-displacementcurve. The loading force at failure in bending test was used to calculate the fracture strength of the beam.

5.2 RESULTS AND DISCUSSION

The raw graphene sheets used in this study were 12 nm in thickness. SEM images of original graphene at both low- and high-magnification can be seen in Figs. 5.1a and 5.1b, which illustrate that graphene sheets were bundled together. Figs. 5.1c and 5.1d show the SEM images of the graphene sheets dispersed by ultrasonication only and the coupled HP and ultrasonication, respectively. For dispersion with ultrasonication only, the majority of the graphene sheets tended to agglomerate and formed flakes in the ethanol solution. Several smaller graphene flakes assembled into a bigger graphene block. However, the graphene sheets dispersed by the coupled ultrasonication and HP (Fig. 5.1d) exhibit a completely different result. Such graphene sheets were well dispersed in the solution, and no graphene floccules were found in the ethanol solution. The individual graphene layers observed with SEM appear transparent. The silicon wafer coated by coarse-grained Au was clearly observed through the covered graphene sheets.

Evidently excellent dispersion of the graphene was achieved by the combined HP and ultrasonication.
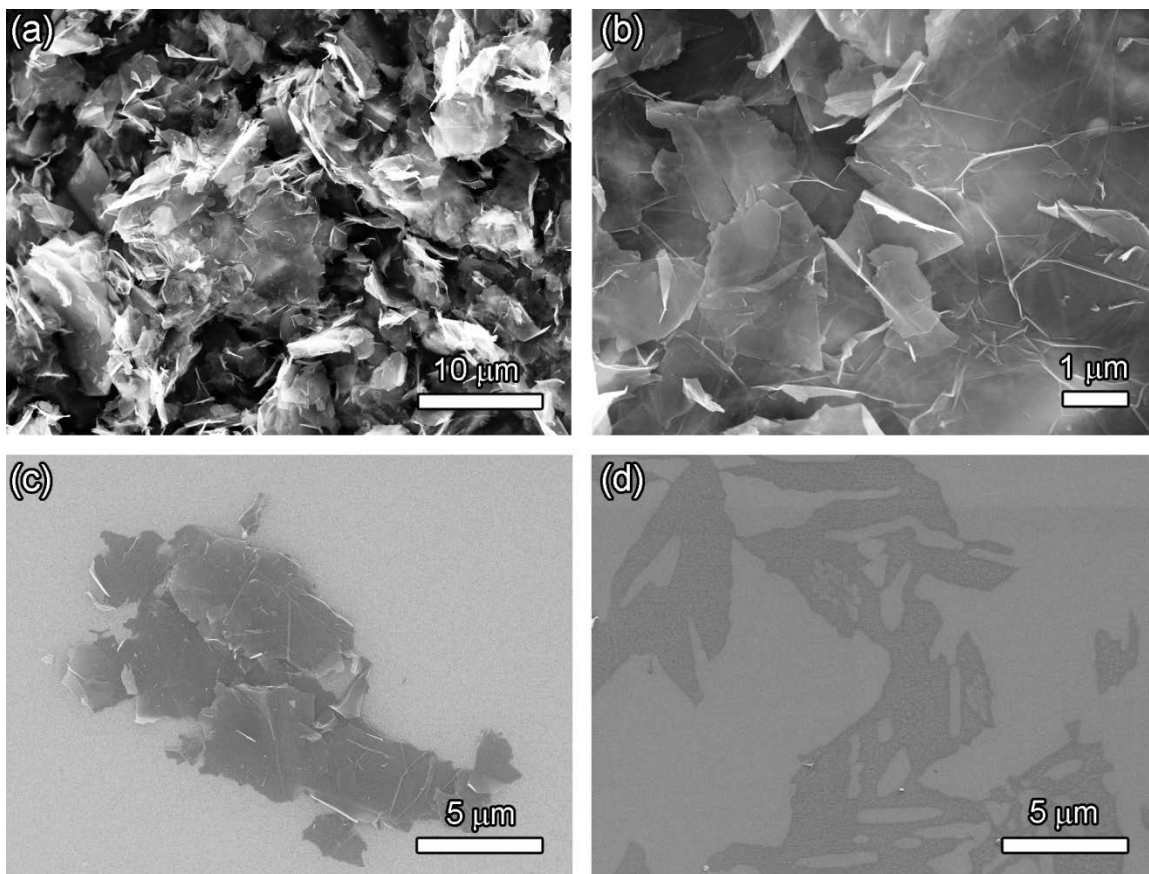
Figure 5.1 SEM images of original and dispersed graphene sheets. (a) and (b) low and high magnification images of original graphene sheets. (c) Graphene sheets dispersed by ultrasonication only. (d) Graphene sheets dispersed by coupled HP and ultrasonication.

Graphene sheets with different concentrations were dispersed into absolute ethanol using the combined HP and ultrasonication. Details of the dispersion can be found in the TEM images (Figure 5.2). The thickness of the dispersed graphene sheets could be down to a few layers when the concentration was less than 2 mg/ml (Figs. 5.2a and 5.2b). We often found graphene flakes containing tens of layers or even more when the concentration was increased up to 3 mg/ml or 5 mg/ml (Figs. 5.2c and 5.2d). The stable solution was achieved when the graphene concentration was ~2 mg/ml.
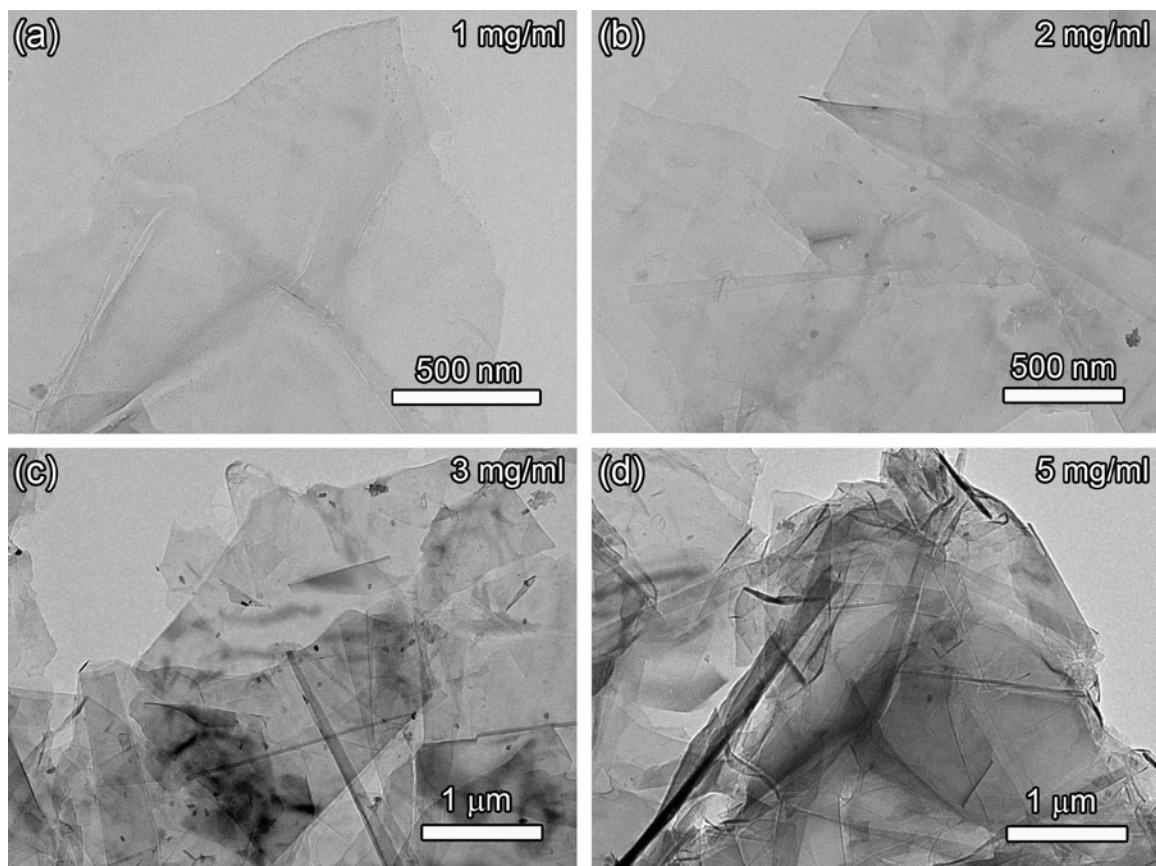
Figure 5.2 TEM images of graphene sheets dispersed in absolute ethanol with different concentrations using the combined hydrogen passivation and ultrasonication. (a) 1 mg/ml. (b) 2 mg/ml. (c) 3 mg/ml. (d) 5 mg/ml.

The graphene solutions dispersed by ultrasonication only and the combined HP and ultrasonication method were dropped onto silicon wafer and Mica for AFM observation, respectively. The AFM mounted with a silicon tip (tip radius: 8 nm) was then employed to scan at random locations, and 50 AFM images were obtained. The average thickness of the dispersed graphene by ultrasonication only was 17.958 ± 5.555 nm (Fig. 5.3a), which was even higher than the average thickness of the original graphene sheets before dispersion. Such difference implies that further agglomeration occurred during dispersion. The dispersed graphene was still in a block format, which is evident in the AFM cross-section analysis (Fig. 5.3c).
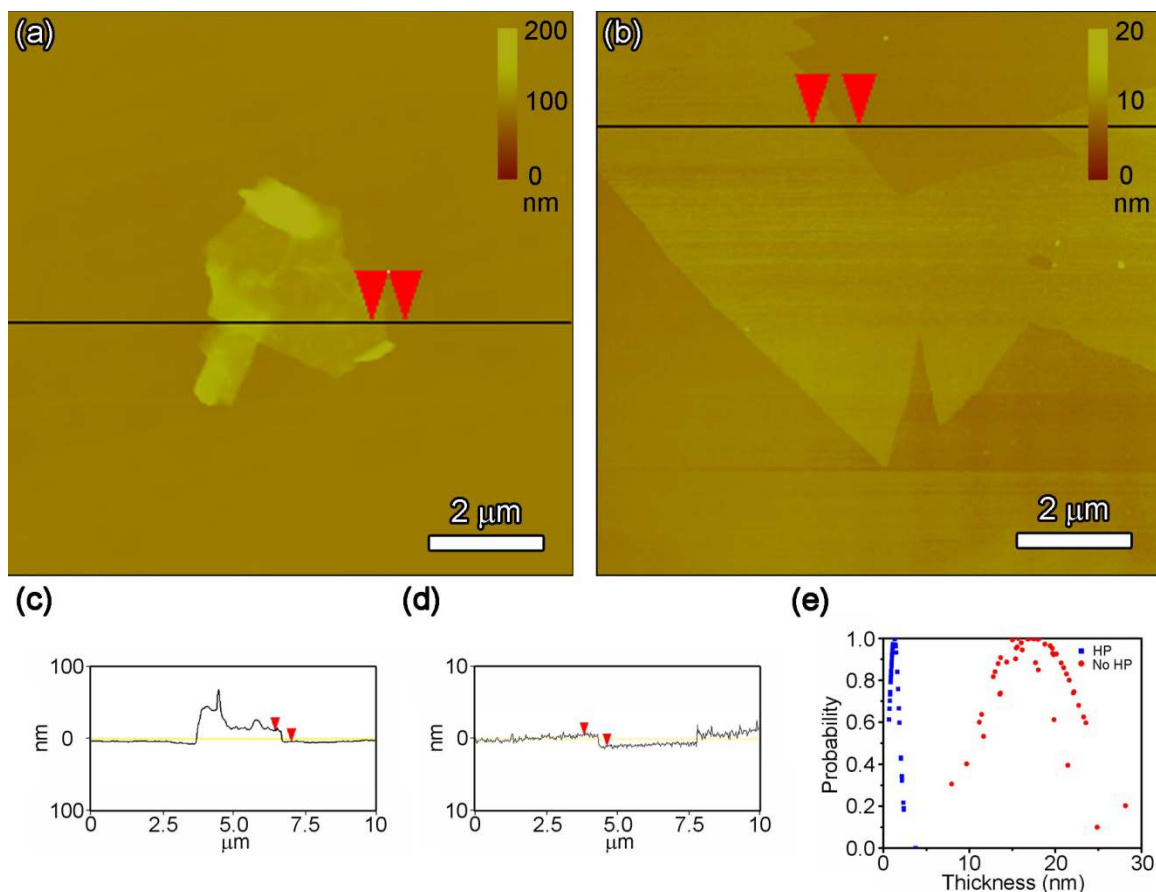
Figure 5.3 AFM characterization on dispersed graphene sheets. (a) A representative AFM image of graphene sheets dispersed by ultrasonication only sitting on a silicon wafer. (b) A representative AFM image of graphene sheets dispersed by the coupled HP and ultrasonication sitting on Mica. (c) and (d) Cross sectional high profiles of graphene sheets in (a) and (b) indicated by line. (e) Probability of thickness distribution of graphene sheets dispersed by ultrasonication only, versus by the coupled HP and ultrasonication.
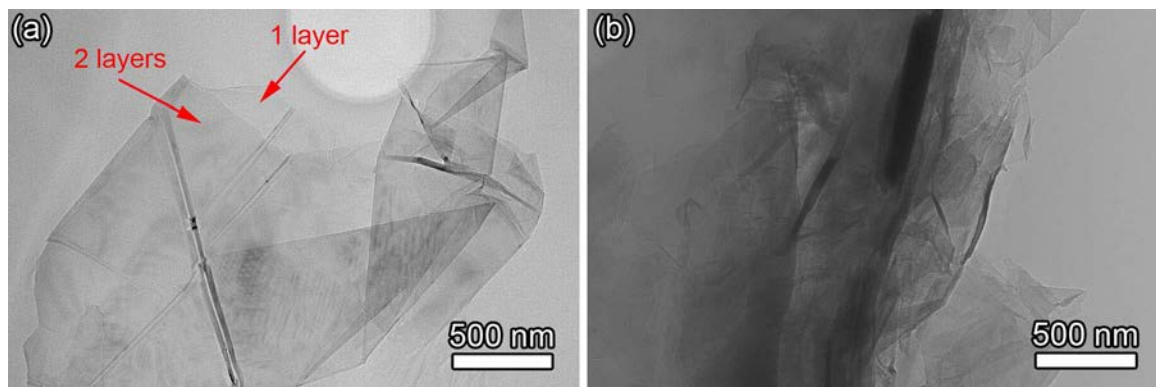
Figure 5.4 TEM images of the graphene sheets dispersed in epoxy. (a) Dispersed by the coupled hydrogen passivation and ultrasonication for 2h. (b) Dispersed by ultrasonication only for 2h.
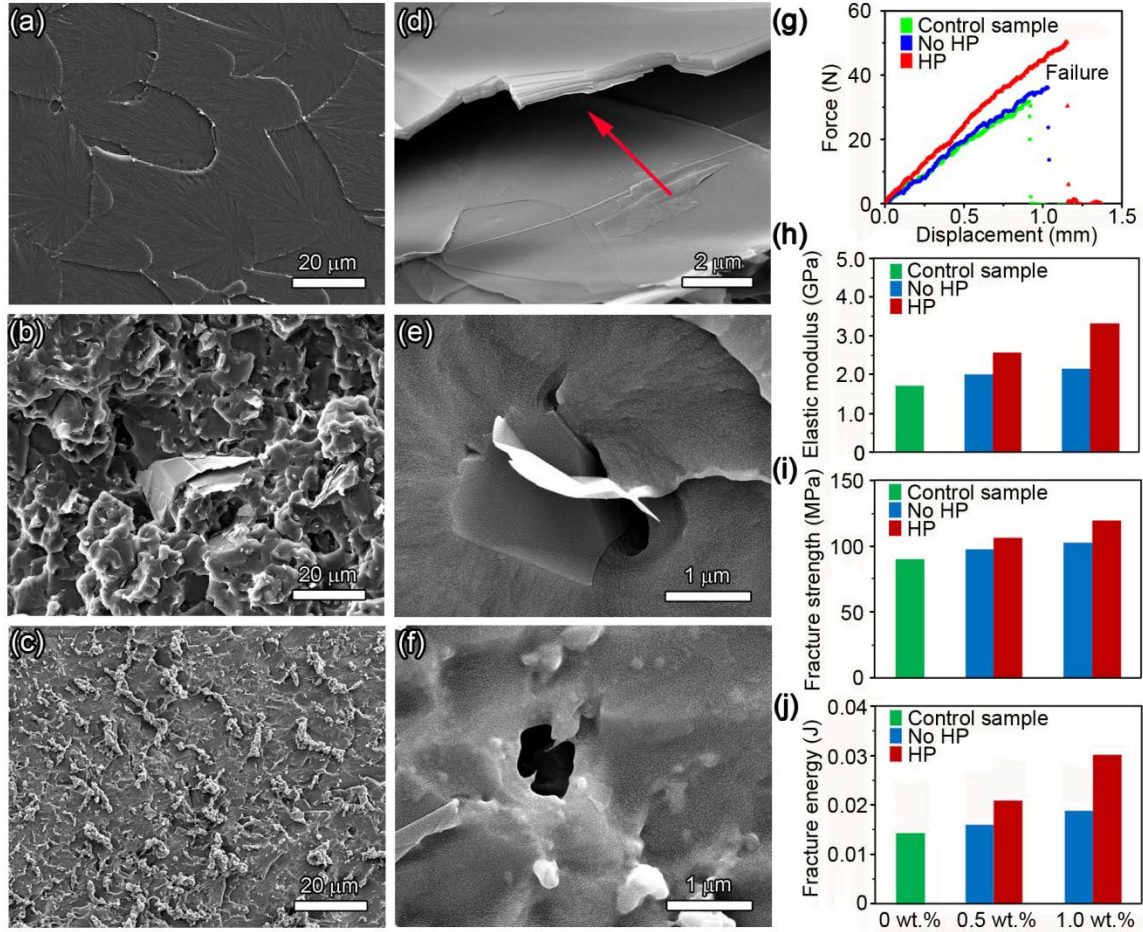
Figure 5.5 Morphology and mechanical characterization of 1.0 wt% graphene/epoxy composites. (a-c) SEM images of fracture surfaces of pure epoxy resin, composites reinforced with graphene dispersed by ultrasonication only and by the coupled HP and ultrasonication, respectively. (d) High magnification image of graphene block in (b). (e) and (f) High magnification images of wrinkled and bridging graphene in (c). (g) Representative load-displacement curves. (h), (i), and (j) Variations of elastic modulus, fracture strength, and fracture energy with different graphene percentage for graphene/epoxy composites.

However, the graphene dispersed by the coupled HP and ultrasonication gives rise to a rather different result. The solution containing dispersed graphene sheets was dropped onto the fresh surface of Mica, whose roughness is much lower than that of the silicon wafer. 50 random AFM images were obtained. The average thickness of the coupled HP and ultrasonication dispersed graphene was 1.275 ± 0.607 nm. A

representative AFM image and corresponding cross-section profile of such dispersed graphene, with the thickness of 1.091 nm, are shown in Figs. 5.3b and 5.3d. The thickness of such dispersed graphene is much lower than that of the graphene dispersed by ultrasonication only. Fig. 5.3e shows the probability analysis of thickness distribution of the graphene sheets dispersed by ultrasonication only, versus the thickness distribution of the graphene sheets dispersed by the coupled HP and ultrasonication. The main peak of the graphene dispersed by the coupled HP and ultrasonication is located at 1 nm, whereas a broad peak is found at 18 nm for the graphene dispersed by ultrasonication only. Clearly the coupled HP and ultrasonication method effectively disperses graphene and prevents its agglomeration, achieving well-dispersed graphene sheets in media.

The composite reinforced graphene block was trimmed under light microscope. The trimmed block was then installed into a microtome (Sorvall MT-2B Ultramicrotome) to obtain thin sections. The thickness was controlled to be ~100 nm. Several pieces of thin sections were transferred to a copper grid (300 mesh). The TEM images of the composite reinforced by dispersed graphene sheets are shown in Fig. 5.4. No gap was found along graphene edges and on the sides, which prove that the graphene and epoxy are in intimate contact. The numbers of graphene layers can be examined by the edges of the sheets. For example, Fig. 5.4a shows that graphene sheets in epoxy dispersed by the coupled hydrogen passivation and ultrasonication contain ~5 graphene layers. Whereas the graphene sheets in epoxy dispersed by ultrasonication only contain a bunch of graphene layers, as shown in Fig. 5.4b and majority of the graphene sheets tend to agglomerate and form flakes in the epoxy.
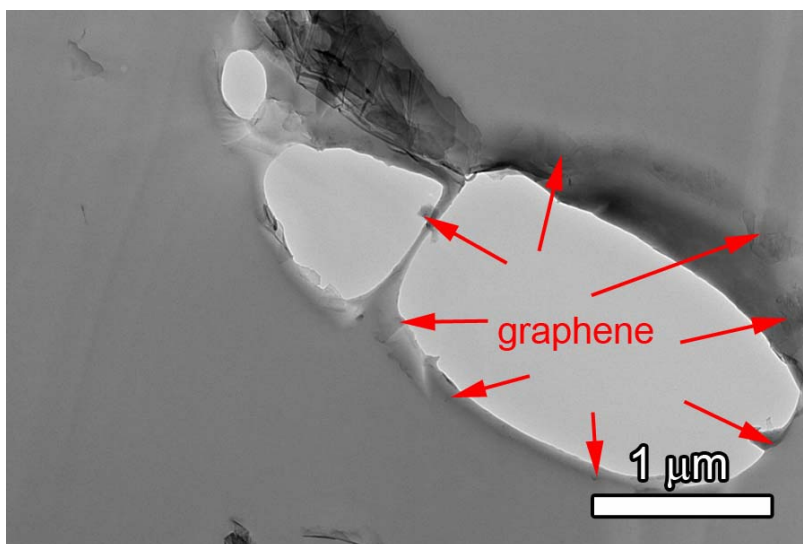
Figure 5.6 TEM image of bridging graphene sheets in epoxy.
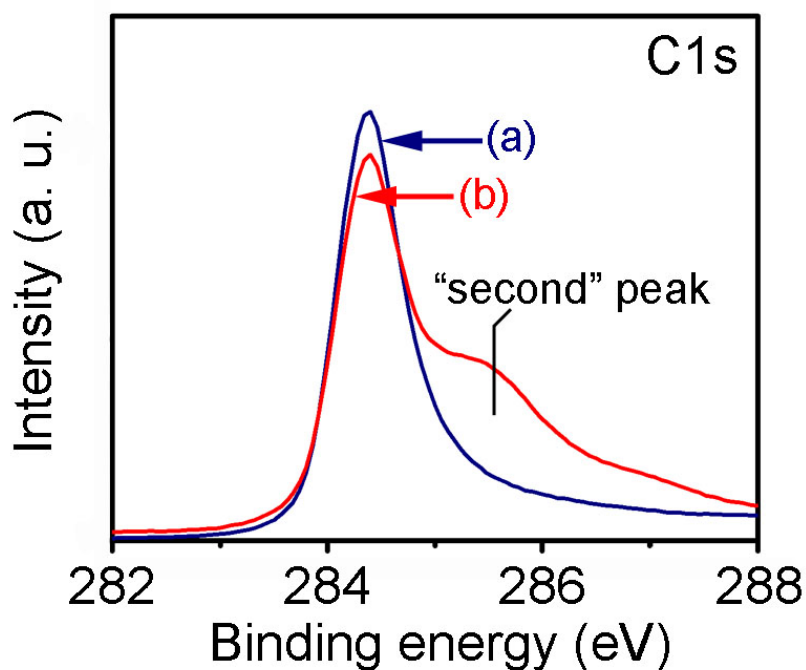
Figure 5.7 C1s XPS of dispersed graphene. (a) Ultrasonication only and (b) coupled HP and ultrasonication.

Figure 5.5 shows the SEM images of the fresh cleavage surfaces of a pure epoxy resin (Fig. 5.5a) and the graphene/epoxy composites fabricated by ultrasonication only (Fig. 5.5b) and by the coupled HP and ultrasonication (Fig. 5.5c). The fracture surface of the control sample is relatively smooth (Fig. 5.5a). Compared to the smooth fracture

surface of the pure epoxy, the fracture surfaces of graphene/epoxy composites are rough and consist of many small facets, elucidating that the graphene inhibits fracture of the composites and thus results in a rougher fracture surface. However, the dispersion of graphene sheets by ultrasonication only was not good enough. Big graphene blocks can be seen in the graphene reinforced composites fabricated by ultrasonication only (Figs. 5.5b and 5.5d). The big gap between the graphene sheets, as indicated by the arrow in Fig. 3d, implies that the graphene sheets slide over each other during the bending test. In this case, the graphene block actually worked as a defect in its composite, which would severely impair the mechanical properties of the composite. While the graphene sheets dispersed by the coupled HP and ultrasonication achieved excellent dispersion in epoxy matrix, no graphene blocks were found on the fracture surface. The graphene was found to be thickly coated with an adsorbed epoxy layer (Fig. 5.5e) and the graphene bridging was often seen on the fracture surface (Fig. 5.5f, and Fig. 5.6), jointly pointing toward strong epoxy-graphene interaction and enhanced mechanical properties.

Figure 5.8 Raman spectra of the graphene sheets dispersed respectively by ultrasonication only and coupled HP and ultrasonication. (a) G band. (b) 2D band.

To unveil the HP induced dispersion mechanism, the chemical interaction between the graphene and the hydrogen atoms is propounded here. Graphene tends to form bundles due to the van der Waals interaction between individual monolayer graphene sheets and the formation of C-C bonds by jointing C dangling bonds of neighboring graphene sheets.[194,195] Upon ultrasonication, graphene was agitated by the applied sound energy from ultrasonication. When the applied sound energy was high enough to overcome the van der Waals force and break the C-C bonds between the individual graphene sheets, the graphene bundles started to debond and be dispersed into the media. If there was no inlet hydrogen during the ultrasonication, the C dangling bonds resulted from the broken C-C bonds might rebind with nearby C dangling bonds when the ultrasonication stopped, leading to rebundling of the graphene sheets. The inlet hydrogen then reacted with the C dangling bonds to form more stable C-H bonds. This process passivated the graphene sheets and prevented them from bundling together through the formation of the C-H bonds during and after ultrasonication so that the excellent dispersion of graphene was achieved. C-H bonds can be identified by the chemical shift of the C1s level due to the hydrogen coordination change in x-ray photoelectron spectroscopy (XPS). The plots (a) and (b) in Figure 5.7 show the C1s XPS for graphene sheets dispersed by ultrasonication only and by the couple HP and ultrasonication, respectively. The graphene was directly exposed to the hydrogen molecules during the HP. The hydrogen interaction with carbon dangling bonds leads to a dramatic change in the C1s peak shape. The second C1s peak is recognized as a shoulder at higher binding energy compared with the C1s peak of the graphene dispersed by ultrasonication only. This observed binding energy shift between the main peak and the second peak for the

graphene dispersed by the couple HP and ultrasonication is attributed to a rehybridization from sp^2 to sp^3 due to the attachment of hydrogen to the C-C π bonds, resulting in C-H bond formation.[170,171] The combined HP and ultrasonication method to disperse graphene sheets has several unparalleled advantages over the conventional dispersion methods. The combined HP and ultrasonication method is powerful in dispersing graphene sheets. Unlike other surface modifications, in which graphene surface is functionalized by the reactions with atoms or molecules, such as organic groups, the HP adds no impurities that may affect the further application of the dispersed graphene. In fact, the hydrogen adsorbed in graphene can be released around 600 °C,[171] therefore no impurities would remain in graphene.

The number of graphene layers was also measured by Raman spectroscopy (Horiba LabRam HR800 Raman Spectrometer). The solutions of graphene sheets with concentration of 1 mg/ml dispersed respectively by ultrasonication only and the combined HP and ultrasonication in absolute ethanol were dropped onto a silicon wafer and dried in ambient condition. Both G band and 2D band are given in Fig. 5.8. The G bands of the graphene sheets dispersed by ultrasonication only and the coupled HP and ultrasonication are at 1586.8 cm^{-1} and 1581.7 cm^{-1}, respectively (Fig. 5.8a). Empirically, the G band position can be correlated to the number of atomic layers via the following relation:[196]

$$\omega_G = 1581.6 + \frac{11}{1+n^{1.6}} \qquad\qquad 5.1$$

The number of layers was found to be 2~5 for the graphene sheets dispersed by the combined HP and ultrasonication, while the number of layers was calculated to be more than 60 for the graphene sheets dispersed by ultrasonication only. The second-order

Raman 2D band reflecting the electronic band structure of graphene is shown in Fig. 5.8b. For multiple-layered graphene sheets, the 2D band is broad due to the change of electronic structure of graphene.[197] The number of lay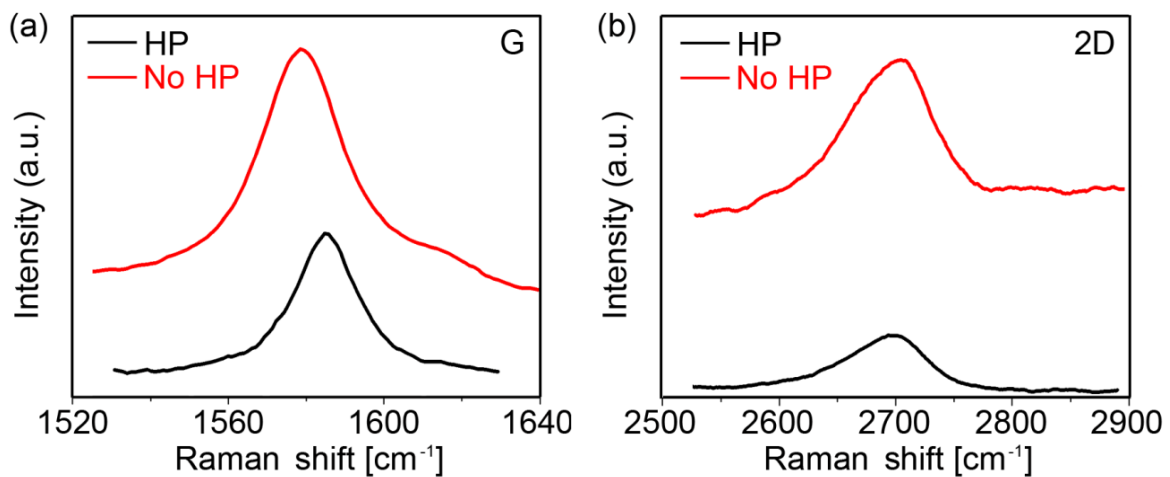ers of the graphene sheets dispersed respectively by ultrasonication only and coupled HP and ultrasonication was determined to be more than 2, as confirmed by both shape and position of the 2D band.[198]

Three-point bending test was performed on the graphene/epoxy composites and epoxy control sample. The elastic modulus was calculated from the linear portion of the bending force-displacement (deflection) curve using the following equation:[97,199]

$$E = \frac{KL^3}{48I} \qquad\qquad 5.2$$

where I, L, and K are the moment of inertia, the suspended length, and the slope of the initial linear portion of the bending force-displacement curve, respectively. The representative bending force-displacement curves are depicted in Fig. 5.5g. The bending force and displacement at failure for the graphene/epoxy composites fabricated by the coupled HP and ultrasonication were much higher than those of the control sample and the graphene/epoxy composites prepared by ultrasonication only. The elastic modulus values of the graphene/epoxy composites and the control sample determined by three-point bending are compared in Fig. 5.5h. As expected, the elastic modulus of the graphene/epoxy composites fabricated by either ultrasonication only or the coupled HP and ultrasonication increases with increasing graphene content. Specifically, the elastic modulus of the composites reinforced with 0.5 wt.% and 1 wt.% graphene by ultrasonication only is, 1.81 ± 0.38 GPa and 1.95 ± 0.42 GPa, respectively, demonstrating only 19.9% and 29.1% increase compared with the control sample with an elastic modulus of 1.51 ± 0.15 GPa. Whereas the graphene/epoxy composites reinforced with

the same amount of graphene fabricated by the coupled HP and ultrasonication exhibit a remarkable increase in elastic modulus. The elastic modulus of the 1.0 wt.% graphene reinforced epoxy composite was measured to be 3.07 ± 0.21 GPa, demonstrating 103.3% and 57.4% increase in elastic modulus compared with the control sample and the composite with the same amount of graphene fabricated by ultrasonication only, respectively. The Halpin-Tsai model, which has been widely used for predicting the modulus of randomly distributed filler-reinforced nanocomposites,[200-203] was employed to calculate the theoretical elastic modulus of the composites by assuming that graphene sheets were perfectly dispersed in the matrix material and every monolayer graphene sheet was coherently bonded with the matrix. The composite modulus Ec is defined as

$$E_c = E_m \left[\frac{3}{8} \frac{1 + \eta_L \zeta V_f}{1 - \eta_L V_f} + \frac{5}{8} \frac{1 + 2\eta_T V_f}{1 - \eta_T V_f} \right] \qquad 5.3$$

$$\eta_L = \left[\frac{\frac{E_f}{E_m} - 1}{\frac{E_f}{E_m} + \zeta} \right] \qquad 5.4$$

$$\eta_T = \left[\frac{\frac{E_f}{E_m} - 1}{\frac{E_f}{E_m} + 2} \right] \qquad 5.5$$

$$\zeta = \frac{2\alpha_f}{3} = \frac{2l_f}{3t_f} \qquad 5.6$$

where E_c is the predicted elastic modulus of composite, E_f and E_m are the elastic modulus of fiber and matrix, respectively. V_f is the volume fraction of the fiber. α_f, l_f, and t_f refer to the aspect ratio, length, and thickness of the graphene sheet, respectively. The theoretical elastic modulus of the 1.0 wt.% graphene reinforced epoxy composite was calculated to

be 3.56 GPa. In our study, the measured elastic modulus was up to 86.23% of the theoretical value. The increase in elastic modulus in the composites fabricated by the coupled HP and ultrasonication is higher than that in the composites with the same graphene contents in previous reports.[117,204-208]

Fracture strength, which is directly related to the flow strength of a material, depends on the effective load transfer between the matrix and the reinforcement phase in a composite. In this study, the fracture strength was calculated by the force at failure during bending using the following equation:[209]

$$\sigma_f = \frac{3PL}{2bh^2} \qquad\qquad 5.7$$

where P, L, b, and h are the maximum bending force, the suspended length, the width and height of the sample, respectively. The fracture strength of the control sample was measured to be 82.01 ± 3.53 MPa, whereas the fracture strength of the graphene/epoxy composites reinforced with 1.0 wt.% graphene fabricated by ultrasonication only and the combined HP and ultrasonication was increased up to 92.81 ± 1.47 MPa and 121.34 ± 5.48 MPa, respectively, demonstrating 13.2% and 47.9% increase compared with the control sample.

Fracture energy, which is the ability of a material to absorb energy and deform up to fracture, was obtained by integrating the load-displacement curve up to the fracture failure. Note that the fracture energy measured here consists of the energy used for both crack initiation and propagation. The fracture energy can be calculated by the equation (5.9) as follows:

$$W_f = \int_0^d f(x)dx \qquad\qquad 5.8$$

where W_f, $f(x)$, and d are the fracture energy, function of load and displacement in curve, and the maximum of displacement, respectively.
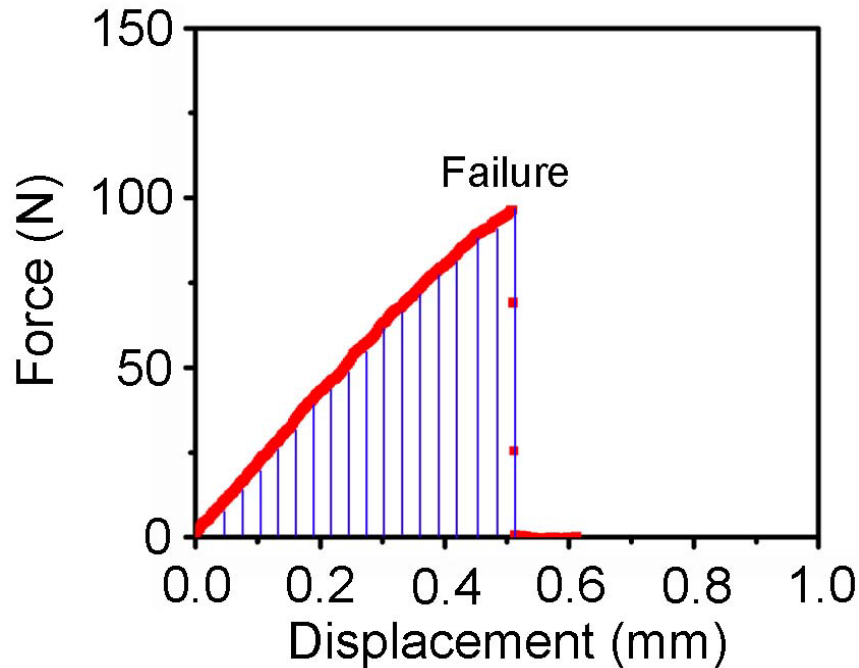
Figure 5.9 Load-displacement curve for calculating fracture energy.

The fracture energy of the control sample, graphene/epoxy composites reinforced with 1.0 wt.% graphene fabricated by ultrasonication only and the coupled HP and ultrasonication, was measured to be 0.014 ± 0.002 J, 0.019 ± 0.002 J, and 0.03 ± 0.004 J, respectively. The 1.0 wt.% graphene reinforced composite fabricated by the coupled HP and ultrasonication exhibits 111.2% and 32.0% increases in fracture energy compared to the control sample and the composite with 1.0 wt.% of graphene fabricated by ultrasonication only, respectively. Such remarkable, simultaneous increases in fracture strength and energy are ascribed to the excellent dispersion of graphene sheets in the epoxy matrix and the strong interfacial bonding between the epoxy and the well-dispersed hydrogen-passivated graphene (Fig. 5.5e). If the interface debonds easily, the load transfer will fail.[210] For instance, the graphene block in the composite fabricated by

ultrasonication only (Fig. 5.5d) debonded and slid over each other, leading to fracture failure at much lower loads. Whereas the composites fabricated by the coupled HP and ultrasonication method demonstrate superior dispersion and ultra strong interfacial bonding, as evidently seen in the wrinkled texture fracture surface and individual graphene sheets wrapped with epoxy on the fracture surface (Figs. 5.5e and 5.5f), which is believed to be responsible for providing an effective load transfer from the epoxy matrix to individual graphene sheets to achieve the exceptional combined properties of high strength, stiffness and fracture energy.

5.3 SUMMARY

A simple, low-cost technique that combines HP with ultrasonication has been developed to separate graphene flakes with an excellent dispersion in both absolute ethanol solution and epoxy resin, overcoming the major roadblock in the application of graphene. The yield is based on the quantity of hydrogen introduced into the solution and the power of ultrasonication. The fabricated graphene/epoxy composites exhibit simultaneous increases in elastic modulus, fracture strength, and fracture energy. The elastic modulus, fracture strength, and fracture energy values of the 1.0 wt.% graphene/epoxy composites fabricated by the coupled HP and ultrasonication are 3.07 ± 0.84 GPa, 121.34 ± 5.48 MPa, and 0.030 ± 0.004 J, respectively, demonstrating respective 103.3%, 47.9%, and 111.2% increase compared to those of the matrix material. The coupled HP and ultrasonication method should find more applications where the structural uniqueness and exceptional properties of graphene need to be fully utilized.

CHAPTER 6

ALIGNED CARBON NANOTUBE REINFORCED SILICON CARBIDE COMPOSITES BY CHEMICAL VAPOR INFILTRATION

Currently, the fabrication of carbon nanotube (CNT)-reinforced ceramic matrix composites (CMCs) mainly follows a disperse-mix-sintering strategy.[211] In this strategy, often the first step is to modify and functionalize the CNT surfaces, followed by dispersing the modified CNTs in a solvent. The CNT solution was then mixed together with a conventional ceramic powder, a colloidal ceramic suspension, or a sol-gel precursor, by applying shear forces using high shear mixers, ultrasonic probes, or ball mills. Finally, the dried CNT-powder mixture was densified by high-temperature hot-pressing sintering (>1600 °C) or by spark-plasma sintering (~1150–1550 °C). Various CNT-CMCs, such as CNT/SiC,[212] CNT/Al$_2$O$_3$,[213-216] CNT/Si$_3$N$_4$,[217] and CNT/SiO$_2$,[218] have been fabricated using such disperse-mix-sintering method. Due to the extremely small size of nanotubes, however, the disperse-mix-sintering method encounters several manufacturing problems in the fabrication of CNT-CMCs, which result in undesirable microstructures and much-lower-than-expected mechanical properties. The manufacturing problems include, but are not limited to, (i) poor dispersion of nanotubes in the matrix, whereby the nanotubes tend to form aggregates, which initiate cracks in composites, rather than reinforcing them; (ii) damage of nanotubes during processing due to surface modification, mechanical mixing and high-temperature sintering that comprise

89

their properties; and (iii) poor interfacial bonding between the nanotubes and the surrounding matrix such that the nanotubes can localize at the grain boundaries of the matrix material as ropes or bundles, which cannot create effective interfacial load transfer. In order to fully exploit the reinforcing ability of CNTs, these manufacturing problems must be solved. Accordingly, it requires (i) homogeneous distribution of CNTs in the matrix; ideally, the CNTs need to be aligned for better performance under stress,[219,220] (ii) development of novel but simple processing methods that do not lead to, or can minimize, CNT damage, and (iii) optimization of the interfacial bonding between CNTs and matrix in order to maximize the energy involved in debonding the CNTs from the matrix while maintaining effective interfacial load transfer.

Continuous-fiber reinforced CMCs (such as carbon/carbon (C/C) and carbon/SiC (C/SiC) composites) are important materials for many advanced high-temperature structural applications, such as aerojet engines, gas turbines, and nuclear reactors.[221] Because of the susceptibility of the fibers to damage from traditional methods used for the fabrication of ceramics such as hot-pressing sintering, a relatively new technique, chemical vapor infiltration (CVI),[222] has emerged in the past two decades as an alternate method for commercial manufacturing of continuous-fiber CMCs. In CVI, gaseous reactants infiltrate a fibrous perform held at an elevated temperature, thereby depositing matrix material on the substrate structure via a standard chemical vapor deposition reaction. The CVI method possesses several significant advantages over conventional CMC fabrication techniques.[221-224] Firstly, it allows the formation of very high melting point materials with high densities at relatively low temperature (900−1100 °C) and little mechanical stress, sparing the fibers from damage and degradation. Secondly, it enables

proper tailoring of the fiber-interface-matrix system with only modest differences in thermal expansion coefficients, producing a composite with optimized interface bonding and minimal residual stress. Thirdly, it permits the use of a wide variety of ceramic matrix materials including carbides, silicides, borides, nitrides, and oxides. Lastly, it allows the fabrication of near-net-shape, complex, three-dimensional (3-D) CMC products that can be used without extensive post-processing machining.

Inspired by the success of CVI in the fabrication of continuous-fiber CMCs, particularly in the fabrication of C/SiC composites, the use of the CVI method to fabricate aligned CNT-reinforced SiC (CNT/SiC) composites is investigated in this chapter. Results show that by using the CVI method, several of the fabrication steps such as dispersion, surface modification, and sintering, are no longer necessary, and therefore most of the manufacturing problems previously encountered in the fabrication of CNT composites can be readily overcome.

6.1 EXPERIMENTAL

Draw was initiated using a piece of adhesive tape to firmly contact the top part (~0.5−1 mm height) of the CNT forest sidewall (see Figure 6.1a). An aligned CNT sheet with a thickness of ~10−20 μm and length the same as the forest height was then made by drawing the tape downwards. The alignment of the nanotubes was well preserved during drawing, as is evident in the photographs of Fig. 6.1b.

A graphite beam (~1×1×5 cm^3 in size) was used to hold the CNT sheets. A stretch (~1 mm wide and 0.5 mm deep) was machined on one surface of the beam along the length direction. One or several CNT sheets were fixed along the stretch with the tubes'

longitudinal direction perpendicular to the beam surface. The graphite beam along with the CNT sheets on it was then placed at the center of an alumina tube that was inserted in a horizontal tube furnace, where the temperature, reaction chamber pressure, gas flow rate, and deposition time can be precisely controlled. After the alumina reaction chamber was pumped to ~2×10^{-3} Torr, the CNT sheets were gradually heated to 1000 °C under the protection of 150 sccm (standard cubic centimeters per minute) flowing argon gas. At 1000 °C, a flow of 150 sccm H_2 gas was used to bubble the reactant methyltrichlorosilane (MTS, CH_3SiCl_3) and carried the MTS vapor into the reaction chamber for SiC deposition. During the CVI process, the reaction chamber pressure was held at 150 Torr. The deposition time varied from 10 to 60 min. After the deposition, the furnace was naturally cooled down to room-temperature.

The morphology and cross-section of the as-synthesized and annealed CNT/SiC composites was examined with a FEI Inspect F field emission gun (FEG) SEM operating at 15 KV. The microstructures of the composites were characterized with a Hitachi HF-3300 FEG STEM/TEM operating at 300 KV.

The elastic modulus (E) and fracture strength (σ_f) of individual CNT/SiC composite nanowires were measured using a Veeco Dimension 3100 AFM by the three-point bending method. A drop of ethanol solution containing the nanowires was placed on a standard AFM reference sample (Veeco Metrology Group) with uniform stretches. In order to avoid sample sliding during the bending tests, both ends of the nanowire, which bridges the trench, were clamped by 20 min of electron-beam-induced deposition of paraffin. The nanowire was then directly indented at the center with either a silicon

AFM tip or a diamond AFM tip till to fracture. The applied bending load–deflection curve during the loading process was recorded.

6.2 RESULTS AND DISCUSSION
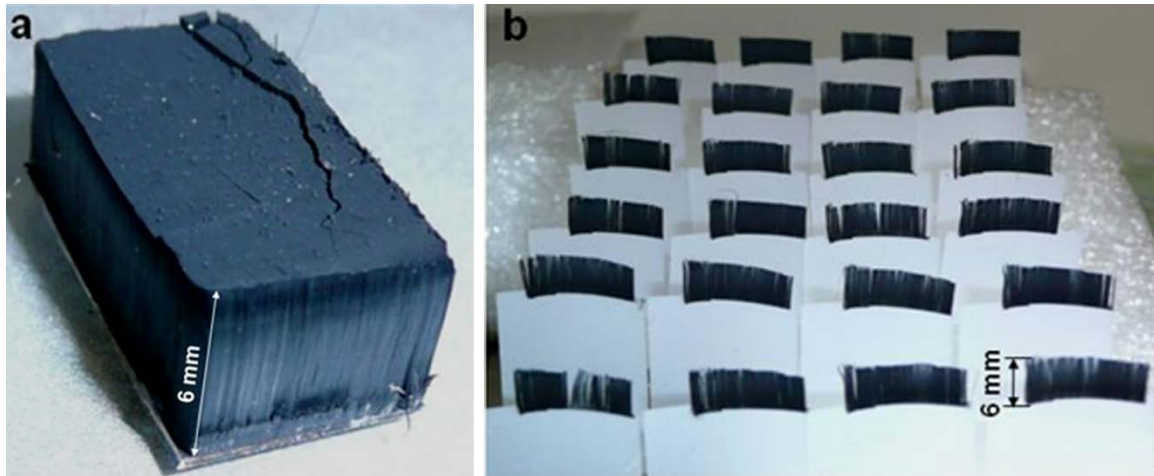
Figure 6.1 Aligned carbon nanotube forest and sheets. (a) Optical image of a 6-mm-tall carbon nanotube forest grown on a Si wafer substrate. (b) Twenty-four 6-mm-long vertically-aligned nanotube sheets drawn from a side wall of the forest in (a).

For the research presented here, millimeter-long aligned multi-walled CNT (MWCNT) sheets were used as the substrates for SiC infiltration.[166,225] The diameters of the nanotubes were ~20 nm. Figure 6.1a shows a 6-mm-tall CNT forest grown on a Si wafer substrate and Fig. 6.1b shows twenty-four 6-mm-long vertically-aligned CNT sheets drawn from a sidewall of the forest. The thicknesses of the CNT sheets are ~10–20 μm. The obtained CNT sheets were fixed on a graphite support that was then inserted into the center of a tube furnace for SiC matrix infiltration. No treatments, such as dispersion, mixing, surface modification, and functionalization, were needed before SiC infiltration, which avoided the structural damage to the nanotubes. In the CVI process, infiltration of SiC matrix occurred via the decomposition of the reactant

methyltrichlorosilane (MTS, CH_3SiCl_3) in the presence of hydrogen. MTS was used because it has a one to one ratio of carbon to silicon that yields stoichiometric SiC over a wide range of processing conditions. Typical CVI conditions used were a deposition temperature of 1000 °C, a H_2 flow rate of 150 sccm (standard cubic centimeters per minute), an Ar flow rate of 150 sccm (Ar functions as a dilute gas), a chamber pressure of 150 Torr, and a deposition time ranging from 10 to 60 min.
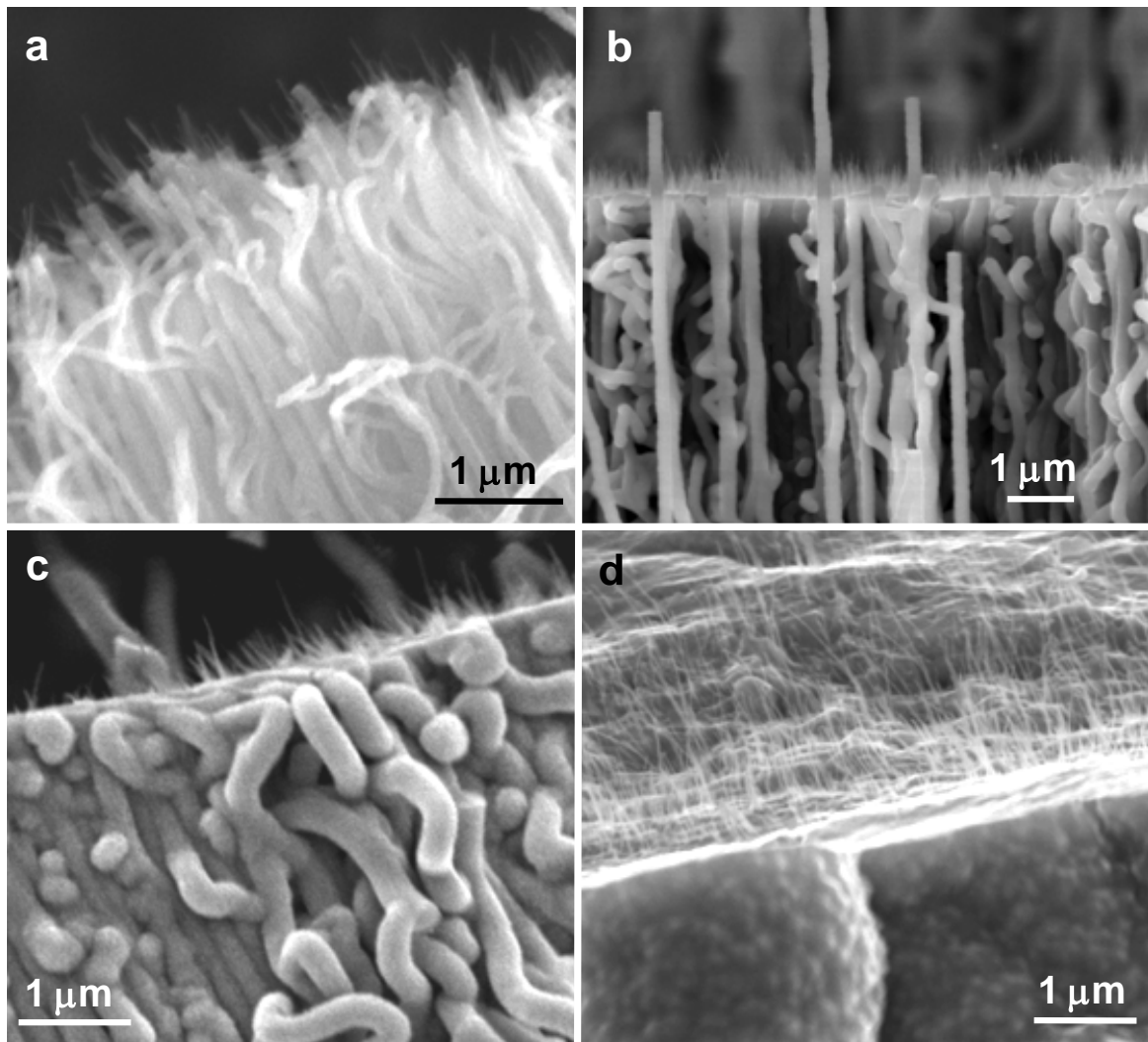
Figure 6.2 SEM images of fractured CNT/SiC composite sheets. (a) A sheet obtained after 10 min infiltration. (b) A sheet obtained after 30 min infiltration. (c) A sheet obtained after 45 min infiltration. (d) A sheet obtained after 60 min infiltration.
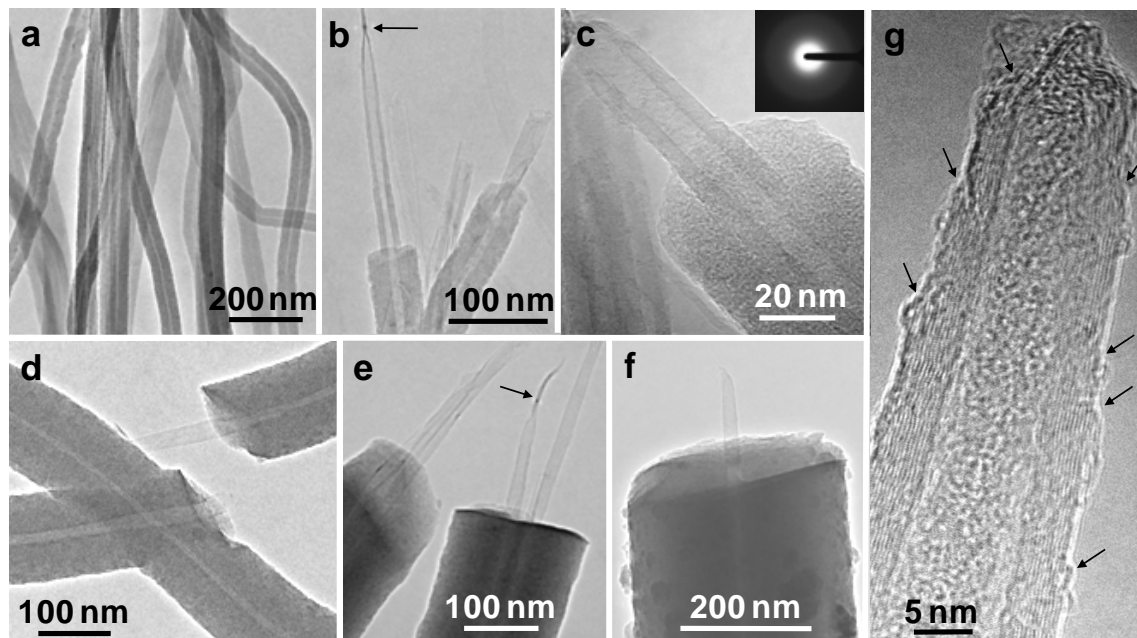
Figure 6.3 TEM and HRTEM images of individual CNT/SiC composite nanowires. (a-c) Nanowires obtained after 10 min infiltration. The arrow in (b) indicates a collapsed nanotube. The inset in (c) is the electron diffraction pattern of the amorphous SiC coating. (d) Nanowires obtained after 20 min infiltration. (e) Nanowires obtained after 30 min infiltration. The arrow indicates a collapsed nanotube. (f) Nanowires obtained after 45 min infiltration. (g) HRTEM image of a broken nanotube. The arrows indicate the positions where the tube shells are broken.

After the CVI reaction, the original black CNT sheets changed in color to silver-grey CNT/SiC sheets while the shapes of the sheets and the alignment of the nanotubes were perfectly preserved. The obtained CNT/SiC sheets were examined using scanning electron microscopy (SEM) and a transmission electron microscope (TEM). Some of the CNT/SiC sheets were intentionally broken using tweezers for the observation of the fracture surfaces. Figure 6.2 shows four fractured CNT/SiC sheets obtained after 10 min, 30 min, 45 min, and 60 min CVI. With increasing infiltration time, the diameter of individual CNT/SiC composite nanowires and the density of the CNT/SiC sheets increased. After 30 min infiltration, the sheet becomes so dense that almost no pores are present on the fracture surface. Nanotube pullout, an important energy absorbing and thus

toughening mechanism for C/SiC composites, was consistently observed on all fracture surfaces of the CNT/SiC samples, indicating that the CNTs can play the same role as carbon fibers to toughen the brittle SiC matrix.

TEM studies of individual CNT/SiC composite nanowires provide additional insights into the morphology, microstructure, and fracture mechanisms of these new composites. TEM imaging confirms the dependence of nanowire diameters on the infiltration time. The diameters of the CNT/SiC nanowires are ~50−60 nm (Figs. 6.3a–6.3c), ~120–130 nm (Fig. 6.3d), ~180–200 nm (Fig. 6.3e), and ~320–340 nm (Fig. 6.3f) after 10 min, 20 min, 30 min, and 45 min infiltration, respectively. Several important CNT growth and CMC fracture (failure) phenomena necessary for high-performance CNT-CMCs, were observed and/or discovered in the TEM studies.

It was observed from the TEM analyses that the SiC matrix was always uniformly coated on the CNT surface regardless of the curvature of the tubes and the infiltration time used (Figs. 6.3a–6.3f). The interfaces between the CNTs and the SiC coating were so intimate that no gaps or voids were observed between them, even when observed with high-resolution TEM (HRTEM) imaging (Fig. 6.3c). These observations indicated that pre-coating or surface treatment of the nanotubes before infiltration to increase interfacial bonding was unnecessary and that chemical damage of the tubes during CVI processing is negligible. These observations, together with the images shown in Fig. 6.2, indicated that in the dense CNT/SiC sheet of the millimeter-long aligned CNTs are coated and surrounded by a uniform, continuous SiC matrix along their entire length. This is a desired structure for a multifunctional CNT composite because it can not only enhance

96

the composite's mechanical performance under stress, but can also improve the composite's electrical and thermal conductivities along the tubes' length.[219]
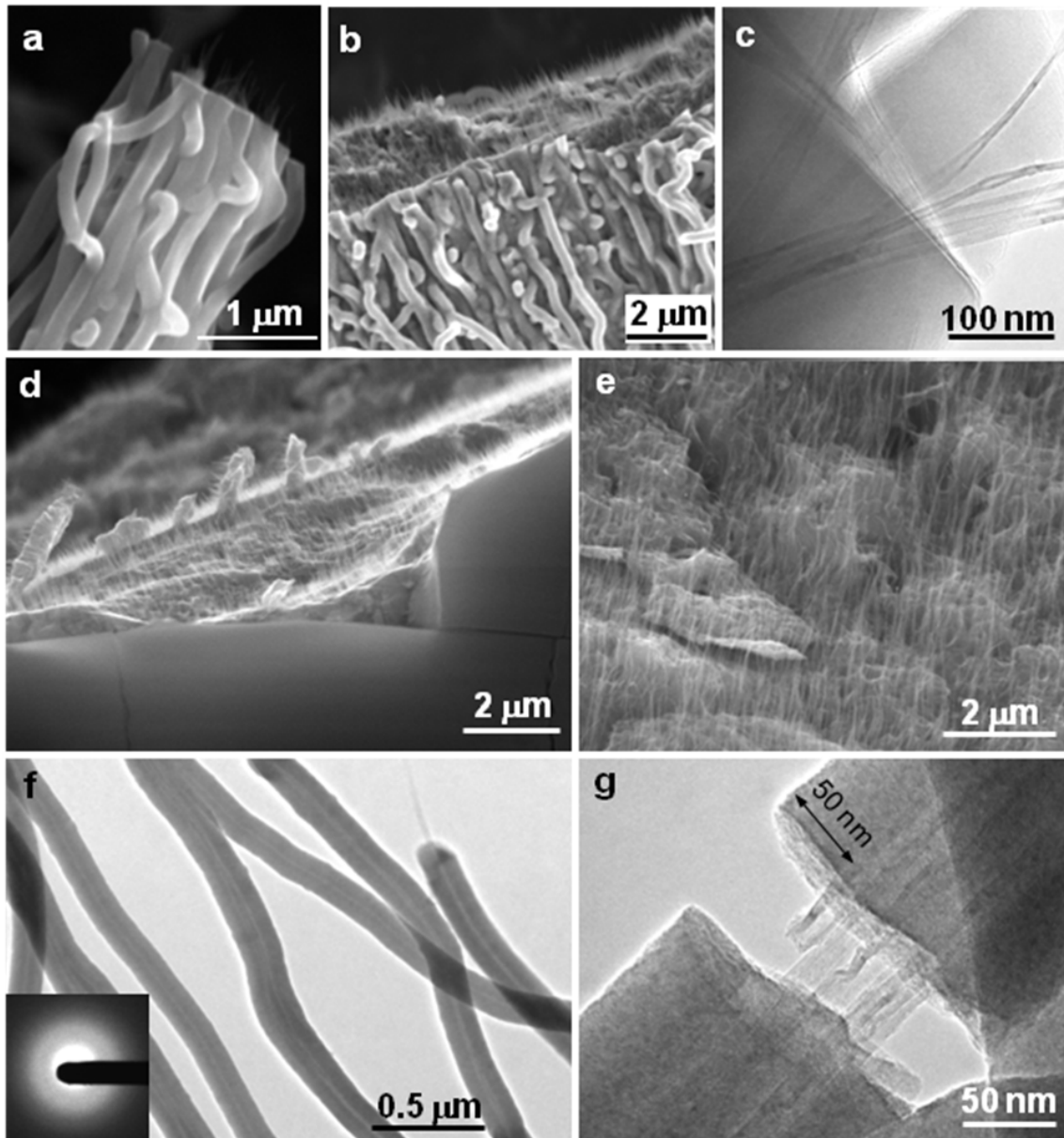
Figure 6.4 SEM and TEM images of fractured CNT/SiC composites after annealing in air at 700°−1600 °C for 1 h. (a) Annealed at 800 °C. (b,c) Annealed at 1200 °C. (d) Annealed at1400 °C. (e−g) Annealed at1600 °C. The inset in (f) is the electron diffraction pattern of the CNT/SiC nanowires. The original CNT/SiC composites were obtained after 30 min of infiltration.

The SiC matrix is amorphous, as confirmed by selected area electron diffraction (SAED) (inset Fig. 6.3c). This is different from the C/SiC composites fabricated using the same CVI conditions, where the SiC matrix consists of columnar grains oriented with the c-axis approximately normal to the micrometer-sized (7–10 μm) carbon fibers.[224,226,227] The formation of amorphous SiC matrix may be related to the very high radius of curvature of the nanotubes, which deserves further theoretical investigation.

The MWCNTs that pulled out during fracture generally have a gradually-shrinking tip (Figs. 6.3b–6.3f); some tubes were severely torn apart, leading to severe deformation or collapse, as indicated by the arrows in Figs. 6.3b and 6.3e. HR-TEM observations (Fig. 6.3g) reveal that the diameter shrinkage is a result of sequential breaking and slippage of the walls of the MWCNTs, i. e., when the outermost wall, which is bonded to the SiC matrix and initially carries the load breaks, the load is transferred to the next graphite wall, and when this wall breaks, the load is transferred to the second wall, and so on, until the tube is completely broken. This sequential breaking process suggests that it is not only the outermost wall adjacent to the matrix that controls the interfacial strength, but that the inner walls of the MWCNTs, also contribute, at least at a certain level, to the mechanical properties of the composites. This added energy absorbing capacity from the inner walls is highly anticipated for MWCNT-reinforced composites because this can maximize the mechanical potential of the nanotubes and can therefore significantly increase the composites' toughness. Note that the finding of sequential breaking and slippages of the nanotube walls during failure is different from the previous simulations and observations of the breaking mechanism of MWCNTs in severe mechanical stress failure mode,[228-232] where it was found that the interaction and

the shear strength between the nanotube walls was very weak and low and that when the outermost wall fractured, the inner sections would be freely pulled out.

The as-synthesized SiC matrix is crack-free. The absence of cracks in the SiC matrix is highly desirable for high-temperature applications because when the composites are exposed to an oxidizing atmosphere at medium or high temperatures, the diffusion of oxygen towards the oxidation-prone CNTs can be avoided.[221] Indeed, our CNT/SiC composites exhibit outstanding oxidization resistance in air over temperatures ranging from 700° to 1600 °C. Figure 6.4 shows SEM and TEM images of the 30-min-infiltrated CNT/SiC composite annealed in air for 1 h at 800 °C (Fig. 6.4a), 1200 °C (Figs. 6.4b and 6.4c), 1400 °C (Fig. 6.4d), and 1600 °C (Figs. 6.4e−6.4g). These images clearly show that the CNTs survived after high-temperature annealing and that CNT pullout occurs for all the annealed samples. At temperatures below 1400 °C, no apparent changes were observed for the composites.

At temperatures above 1400 °C, a ~0.5−1 μm thick silica shell was often formed on the CNT/SiC sheet surface due to the oxidization of SiC (Fig. 6.4d). However, we did not observe oxidization on all of the individual annealed CNT/SiC nanowires, even at 1600 °C, as that displayed in Figs. 6.4f and 6.4g. Remarkably, Fig. 4.4g clearly reveals that a SiC coating as thin as ~50 nm can effectively protect the CNT from being oxidized at temperature as high as 1600 °C. Moreover, TEM imaging and SAED analyses show that the SiC matrix remains amorphous after annealing, up to 1600 °C (Figs. 6.4f and 6.4g). The resistance to crystallization of the amorphous SiC matrix at high-temperature may be related to its strong Si−C covalent bonds, which would show negligible

contributions to the enthalpy of formation from long-range bonding interactions that

drive crystallization.[233]
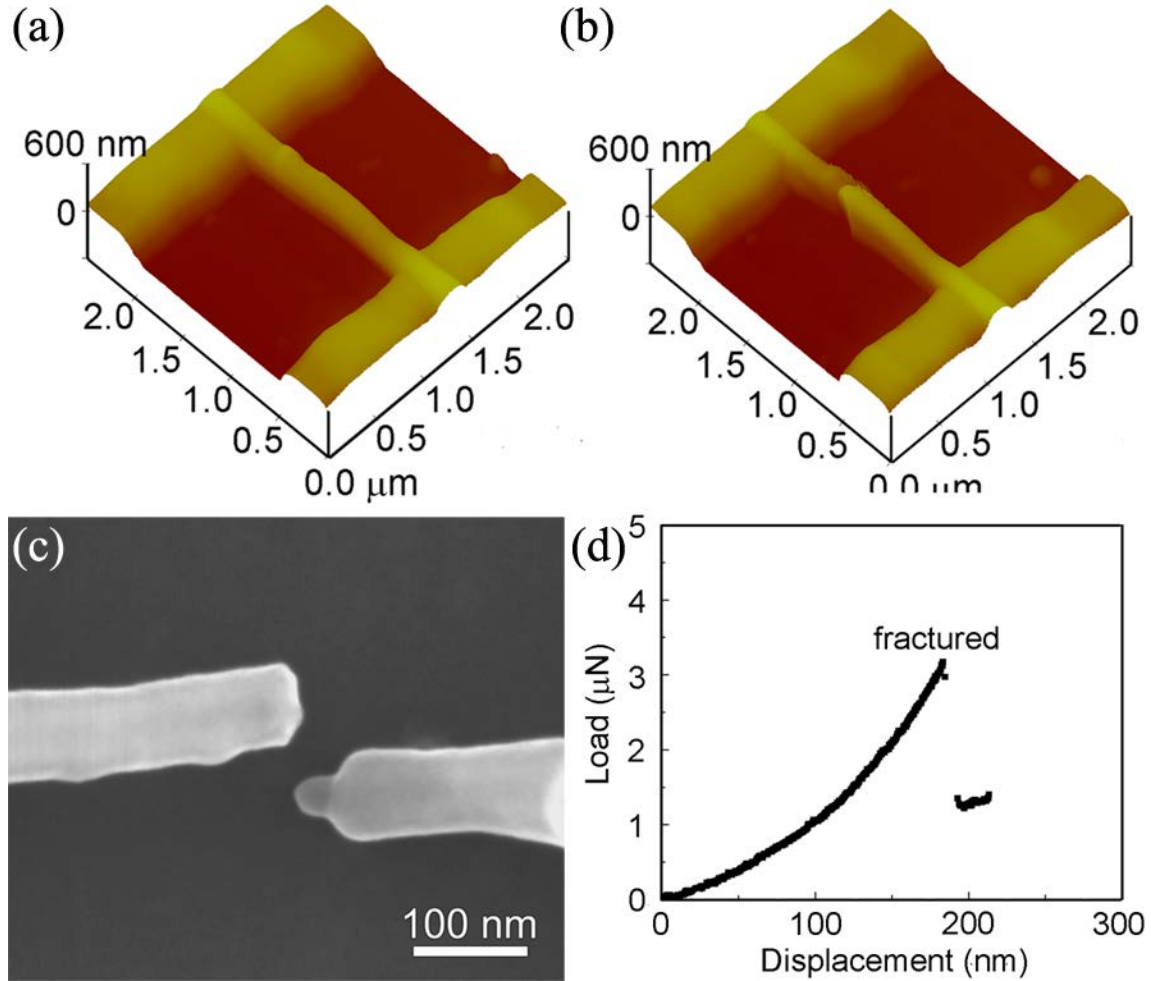
Figure 6.5 Mechanical properties of CNT/SiC composites. (a,b) AFM images of a 10-min-grown CNT/SiC nanowire (diameter: ~55 nm) suspended over a trench before and after three-point bending, respectively. The two ends of the nanowire were clamped to the trench edges by 20 min of electron-beam-induced deposition of paraffin. (c) SEM image of the fractured CNT/SiC nanowire in (b), showing the pullout and breakage of the CNT with a tapered tip. (d) Applied bending load-deflection curve of the AFM three-point bending measurement on the CNT/SiC nanowire in (a) and (b).

A well-known embrittlement problem exists for C/SiC composites in the

intermediate temperature range of 700–800 °C, as a result of the large difference between

the coefficients of thermal expansion of the carbon fibers and the matrix, which can cause

the formation of microcracks in the vicinity of the fiber-matrix interface. The microcracks result in fiber/matrix debonding at the crack tips and facilitate the diffusion of oxygen towards the oxidation-prone carbon fibers.[223,234] In contrast, the CNT/SiC composites in this study exhibited no embrittlement problem and abnormal oxidation occurred in the temperature range 700–800 °C (Fig. 6.4a). This can be explained by the crack-free microstructures of the CNT/SiC composites both in the as-synthesized (Fig. 6.3) and the annealed conditions (Fig. 6.4). Due to the small size and flexibility of the CNTs, the stress caused by the differences between the coefficients of thermal expansion of the CNTs and the SiC matrix would be too small to cause the formation of cracks in the CNT/matrix interface. In addition, the high degree of connectivity of the amorphous SiC network, owing to the presence of C as a network component, is expected to suppress the formation and propagation of the cracks within the matrix.[233]

Using a Veeco Dimension 3100 atomic force microscope (AFM), the elastic modulus (E) and fracture strength (σ_f) of individual CNT/SiC nanowires were measured by the three-point bending (Figure 6.5). Fig. 6.5a shows a 10-min-infiltrated CNT/SiC nanowire suspended over a trench before three-point bending. The nanowire was then directly indented at the center with either a silicon AFM tip or a diamond AFM tip until fracture (Fig. 6.5b). SEM imaging on the fractured CNT/SiC nanowire clearly shows that the SiC shell fractured first and then the CNT core was pulled out and/or broken with a shrinking tip (Fig. 6.5c). The applied bending load–deflection curve during the loading process is presented in Fig. 6.5d. The elastic modulus can be calculated from the initial linear portion of the loading curve using a method previously reported.[235,236] The obtained E value from Fig. 6.5d was 239.2 GPa and the average E value obtained from

four 10-min-infiltrated CNT/SiC nanowires was 234±18.9 GPa, which both are higher than the elastic modulus (~150 GPa) of amorphous SiC films.[237] The σ_f value of the nanowires can be calculated using equation 6.1

$$\sigma_f = \frac{FL}{2\pi r^3} \qquad\qquad 6.1$$

where F is the applied bending load when the nanowire cracks, L is the suspended length of the nanowire over the trench, and r is the radius of the nanowire. The σ_f value obtained from Fig. 6.5c was 18.2 GPa and the average σ_f value obtained from four 10-min-infiltrated nanowires was 20±6.4 GPa, which both approached the predicted maximum of $0.1E$.[238] The σ_f value of the 10-min-infiltrated CNT/SiC composite nanowires (50−60 nm in diameter) was about half of that obtained for a 21.5-nm-diameter crystalline SiC nanorod.[1]

The AFM three-point bending measurements showed that as the infiltration time increased from 10 to 30 min, the E value of the CNT/SiC nanowires decreased from 234±18.9 to 188±25.9 GPa and the σ_f value decreased from 20±6.4 to 6±1.2 GPa. This is because as the infiltration time increases, the SiC portion of the CNT/SiC nanowires increases significantly (see Fig. 6.3) and the mechanical properties of the CNT/SiC nanowires are therefore dominated by SiC which is brittle in nature and weaker than the CNTs. Nevertheless, the obtained σ_f values from the CNT/SiC nanowires are about an order of magnitude larger than the value of ~0.4−1 GPa obtained from bulk SiC crystals measured by either the three-point bending method or the four-point bending method,[239,240] revealing the remarkable reinforcement effect from the CNTs.

Besides the individual CNT/SiC sheets reported here, it is possible to incorporate aligned CNT arrays into 3-D preforms so that 3-D CNT/SiC composites with isotropic mechanical properties can be fabricated. Using long CNT sheets or ropes,[241,242] it is possible to fabricate near-net-shape products if the sheets or ropes are woven into the shape of the final component before matrix infiltration. Moreover, random CNT-reinforced SiC composites can also be fabricated if a sheet composed of random MWCNTs or single-walled CNTs is used as the deposition substrate. Lastly, our experiments showed that the CVI method can be extended to produce CNT composites from a variety of matrix materials including not only carbides but also borides and silicates.

6.3 SUMMARY

Exceptional-tough CNT/SiC composites have been fabricated by CVI technique. By using the CVI method, several of the fabrication steps such as dispersion, surface modification, and sintering, are no longer necessary, and therefore most of the manufacturing problems previously encountered in the fabrication of CNT composites can be readily overcome. Nanotube pullout and sequential breaking and slippage of the walls of the CNTs during failure were consistently observed for all fractured CNT/SiC samples. These energy absorbing mechanisms result in the fracture strength of the CNT/SiC composites about an order of magnitude higher than the bulk SiC. The CVI-fabricated CNT/SiC composites have a stronglybonded tube/matrix interface and an amorphous, crack-free SiC matrix, enabling the composites to withstand oxidization at 700–1600 °C in air.

CHAPTER 7

SUMMARY AND FUTURE SUGGESTIONS

7.1 SUMMARY OF MAIN RESULTS

The strong water molecule induced stiffening effect was observed for the first time in ZnO nanobelts by using an atomic force microscopy three-point bending test. Water molecule adsorption on the ZnO surface can attract surface Zn atoms to move outward and hence increase the surface stress of ZnO. Increasing surface stress associated with water adsorption is believed to be responsible for the experimentally observed enhancement of the elastic modulus of ZnO nanobelts with the increase of humidity. Significant thermal stability depression is found in the ZnO nanobelts as well. The thermal expansion coefficient of the ZnO nanobelt at 400 °C is 3.67×10^{-4}/K which is two orders of magnitude higher than that of the ZnO nanobelt at room temperature. The nanobelt may melt at ∼600 °C which is much lower than the melting point of the bulk ZnO. Both thermal stability depressions in the ZnO nanobelts were confirmed by *in-situ* TEM, AFM, and SEM.

A method for dispersing MWCNTs and graphene flakes has been developed by coupling HP and ultrasonication. SEM, TEM, and AFM observations reveal that excellent dispersion of MWCNTs and graphene has been achieved in ethanol and in epoxy within 2 h. The fabricated MWCNT/epoxy and graphene/epoxy composites exhibit simultaneous increases in the elastic modulus, fracture strength and fracture energy. The coupled HP and ultrasonication method should find more applications where the

structural uniqueness and exceptional properties of CNTs and graphene need to be fully utilized.

Exceptional-tough CNT/SiC composites have been fabricated by the CVI technique. Nanotube pullout and sequential breaking and slippage of the walls of the CNTs during failure occurred in all our fractured CNT/SiC samples. These energy absorbing mechanisms result in the fracture strength of the CNT/SiC composites about one order of magnitude higher than the bulk SiC.

7.2 SUGGESTIONS FOR FUTURE RESEARCH

The ZnO nanobelt may melt at ~600 °C which is much lower than the melting point of bulk ZnO. This research does not, however, discuss the effect of electron beam knocking-out. The electron beam radiation can knock out atoms and electrons when the material size is down to nanometers. The thickness of the ZnO nanobelt in the study is ~50 nm. Compare to the bulk materials, such a thickness is extremely small, the "knocking-out threshold" will be low as well. In fact, structural damage may be induced by using an accelerating energy of 97-120 kV in TEM observation. In our research, the voltage was set at 200 kV. The applied electron beam might distort the ZnO nanobelt at high temperature. The heating make the ZnO nanobelt accumulate enough energy, and further electron beam irradiation may led to the collapse of the entire nanostructure.

Although the mechanical performance of nanocomposites has been improved by dispersed CNTs and graphene sheets, the interfaces between a CNT/matrix and a graphene/matrix in reinforced nanocomposites have not been studied in detail. *In-situ* interface evolution resulting in effective load transfer during mechanical testing may shed

light on the mechanism of mechanical reinforcement in CNT and graphene reinforced nanocomposites. New mechanical characterization techniques beyond AFM and nanoindentation, such as *in-situ* TEM-mechanical device and *in-situ* SEM-mechanical device to unveil both structural change and mechanical properties should be addressed.

Combined hydrogen passivation and ultrasonication has been successfully applied to disperse MWCNTs and graphene sheets. The mechanism has also been discovered. Graphene sheets bought on the market are expensive, but if commercial graphite can be converted to graphene using the above-mentioned method, the cost could be reduced.

REFERENCES

1. E. W. Wong, P. E. Sheehan, and C. M. Lieber, "Nanobeam mechanics: elasticity, strength, and toughness of nanorods and nanotubes" *Science* **1997**, *277*, 1971-1975.

2. Y. Huang, X. F. Duan, Q. Q. Wei, and C. M. Lieber, "Directed assembly of one-dimensional nanostructures into functional networks" *Science* **2001**, *291*, 630-633.

3. X. D. Bai, P. X. Gao, Z. L. Wang, and E. G. Wang, "Dual-mode mechanical resonance of individual ZnO nanobelts" *Applied Physics Letters* **2003**, *82*, 4806-4808.

4. J. H. Song, X. Wang, E. Riedo, and Z. L. Wang, "Elastic property of vertically aligned nanowires" *Nano Letters* **2005**, *5*, 1954-1958.

5. U. Ozgur, Y. I. Alivov, C. Liu, A. Teke, M. A. Reshchikov, S. Dogan, V. Avrutin, S. J. Cho, and H. Morkoc, "A comprehensive review of ZnO materials and devices" *Journal of Applied Physics* **2005**, *98*, 041301.

6. Q. Wan, Q. H. Li, Y. J. Chen, T. H. Wang, X. L. He, J. P. Li, and C. L. Lin, "Fabrication and ethanol sensing characteristics of ZnO nanowire gas sensors" *Applied Physics Letters* **2004**, *84*, 3654-3656.

7. R. L. Hoffman, B. J. Norris, and J. F. Wager, "ZnO-based transparent thin-film transistors" *Applied Physics Letters* **2003**, *82*, 733-735.

8. Z. L. Wang and J. H. Song, "Piezoelectric nanogenerators based on zinc oxide nanowire arrays" *Science* **2006**, *312*, 242-246.

9. N. H. Tai, M. K. Yeh, and H. H. Liu, "Enhancement of the mechanical properties of carbon nano tube/phenolic composites using a carbon nanotube network as the reinforcement" *Carbon* **2004**, *42*, 2774-2777.

10. T. Ogasawara, Y. Ishida, T. Ishikawa, and R. Yokota, "Characterization of multi-walled carbon nanotube/phenylethynyl terminated polyimide composites" *Composites Part a-Applied Science and Manufacturing* **2004**, *35*, 67-74.

11. F. H. Gojny, M. H. G. Wichmann, U. Kopke, B. Fiedler, and K. Schulte, "Carbon nanotube-reinforced epoxy-compo sites: enhanced stiffness and fracture toughness at low nanotube content" *Composites Science and Technology* **2004**, *64*, 2363-2371.

107

12. Z. L. Wang, "Zinc oxide nanostructures: growth, properties and applications" *Journal of Physics-Condensed Matter* **2004**, *16*, R829-R858.

13. Z. L. Wang, "Functional oxide nanobelts: Materials, properties and potential applications in nanosystems and biotechnology" *Annual Review of Physical Chemistry* **2004**, *55*, 159-196.

14. P. X. Gao and Z. L. Wang, "Substrate atomic-termination-induced anisotropic growth of ZnO nanowires/nanorods by the VLS process" *Journal of Physical Chemistry B* **2004**, *108*, 7534-7537.

15. A. Marcu, L. Trupina, R. Zamani, J. Arbiol, C. Grigoriu, and J. R. Morante, "Catalyst size limitation in vapor-liquid-solid ZnO nanowire growth using pulsed laser deposition" *Thin Solid Films* **2012**, *520*, 4626-4631.

16. Q. X. Zhao, P. Klason, and M. Willander, "Growth of ZnO nanostructures by vapor-liquid-solid method" *Applied Physics a-Materials Science & Processing* **2007**, *88*, 27-30.

17. J. R. Morber, Y. Ding, M. S. Haluska, Y. Li, P. Liu, Z. L. Wang, and R. L. Snyder, "PLD-assisted VLS growth of aligned ferrite nanorods, nanowires, and nanobelts-synthesis, and properties" *Journal of Physical Chemistry B* **2006**, *110*, 21672-21679.

18. M. Kirkham, X. D. Wang, Z. L. Wang, and R. L. Snyder, "Solid Au nanoparticles as a catalyst for growing aligned ZnO nanowires: a new understanding of the vapour-liquid-solid process" *Nanotechnology* **2007**, *18*, 365304

19. G. Zhu, Y. S. Zhou, S. H. Wang, R. S. Yang, Y. Ding, X. Wang, Y. Bando, and Z. L. Wang, "Synthesis of vertically aligned ultra-long ZnO nanowires on heterogeneous substrates with catalyst at the root" *Nanotechnology* **2012**, *23*, 055604.

20. S. Y. Li, C. Y. Lee, and T. Y. Tseng, "Copper-catalyzed ZnO nanowires on silicon (100) grown by vapor-liquid-solid process" *Journal of Crystal Growth* **2003**, *247*, 357-362.

21. Y. Ding, P. X. Gao, and Z. L. Wang, "Catalyst-nanostructure interfacial lattice mismatch in determining the shape of VLS grown nanowires and nanobelts: A case of Sn/ZnO" *Journal of the American Chemical Society* **2004**, *126*, 2066-2072.

22. V. Engels, A. Rachamim, S. H. Dalal, S. M. L. Pfaendler, J. F. Geng, A. Berenguer-Murcia, A. J. Flewitt, and A. E. H. Wheatley, "Nanoparticulate PdZn as a novel catalyst for ZnO nanowire growth" *Nanoscale Research Letters* **2010**, *5*, 904-907.

23. T. J. Sun, J. S. Qiu, and C. H. Liang, "Controllable fabrication and photocatalytic activity of ZnO nanobelt arrays" *Journal of Physical Chemistry C* **2008**, *112*, 715-721.

24. Z. W. Pan, Z. R. Dai, and Z. L. Wang, "Nanobelts of semiconducting oxides" *Science* **2001**, *291*, 1947-1949.

25. A. Umar, S. H. Kim, Y. S. Lee, K. S. Nahm, and Y. B. Hahn, "Catalyst-free large-quantity synthesis of ZnO nanorods by a vapor-solid growth mechanism: Structural and optical properties" *Journal of Crystal Growth* **2005**, *282*, 131-136.

26. F. Yang, W. H. Liu, .W. Wang, J. Zheng, R. Y. Shi, H. Zhao, and H. Q. Yang, "Controllable low temperature vapor-solid growth and hexagonal disk enhanced field emission property of ZnO nanorod arrays and hexagonal nanodisk networks" *ACS Applied Materials & Interfaces* **2012**, *4*, 3852-3859.

27. J. Y. Li, Q. Zhang, H. Y. Peng, H. O. Everitt, L. C. Qin, and J. Liu, "Diameter-controlled vapor-solid epitaxial growth and properties of aligned ZnO nanowire arrays" *Journal of Physical Chemistry C* **2009**, *113*, 3950-3954.

28. A. Umar, Y. H. Im, and Y. B. Hahn, "Evolution of ZnO nanostructures on silicon substrate by vapor-solid mechanism: Structural and optical properties" *Journal of Electronic Materials* **2006**, *35*, 758-765.

29. S. Mandal, K. Sambasivarao, A. Dhar, and S. K. Ray, "Photoluminescence and electrical transport characteristics of ZnO nanorods grown by vapor-solid technique" *Journal of Applied Physics* **2009**, *106*, 024103.

30. L. C. Campos, M. Tonezzer, A. S. Ferlauto, V. Grillo, R. Magalhaes-Paniago, S. Oliveira, L. O. Ladeira, and R. G. Lacerda, "Vapor-solid-solid growth mechanism driven by epitaxial match between solid AuZn alloy catalyst particles and ZnO nanowires at low temperatures" *Advanced Materials* **2008**, *20*, 1499-1504.

31. B. Liu and H. C. Zeng, "Hydrothermal synthesis of ZnO nanorods in the diameter regime of 50 nm" *Journal of the American Chemical Society* **2003**, *125*, 4430-4431.

32. U. Pal and P. Santiago, "Controlling the morphology of ZnO nanostructures in a low-temperature hydrothermal process" *Journal of Physical Chemistry B* **2005**, *109*, 15317-15321.

33. K. H. Tam, C. K. Cheung, Y. H. Leung, A. B. Djurisic, C. C. Ling, C. D. Beling, S. Fung, W. M. Kwok, W. K. Chan, D. L. Phillips, L. Ding, and W. K. Ge, "Defects in ZnO nanorods prepared by a hydrothermal method" *Journal of Physical Chemistry B* **2006**, *110*, 20865-20871.

34. J. B. Liang, J. W. Liu, Q. Xie, S. Bai, W. C. Yu, and Y. T. Qian, "Hydrothermal growth and optical properties of doughnut-shaped ZnO microparticles" *Journal of Physical Chemistry B* **2005**, *109*, 9463-9467.

35. H. Zhang, D. Yang, Y. J. Ji, X. Y. Ma, J. Xu, and D. L. Que, "Low temperature synthesis of flowerlike ZnO nanostructures by cetyltrimethylammonium bromide-assisted hydrothermal process" *Journal of Physical Chemistry B* **2004**, *108*, 3955-3958.

36. B. Cheng and E. T. Samulski, "Hydrothermal synthesis of one-dimensional ZnO nanostructures with different aspect ratios" *Chemical Communications* **2004**, 986-987.

37. L. Li, S. S. Pan, X. C. Dou, Y. G. Zhu, X. H. Huang, Y. W. Yang, G. H. Li, and L. D. Zhang, "Direct electrodeposition of ZnO nanotube arrays in anodic alumina membranes" *Journal of Physical Chemistry C* **2007**, *111*, 7288-7291.

38. Y. W. Tang, L. J. Luo, Z. G. Chen, Y. Jiang, B. H. Li, Z. Y. Jia, and L. Xu, "Electrodeposition of ZnO nanotube arrays on TCO glass substrates" *Electrochemistry Communications* **2007**, *9*, 289-292.

39. L. F. Xu, Q. W. Chen, and D. S. Xu, "Hierarchical ZnO nanostructures obtained by electrodeposition" *Journal of Physical Chemistry C* **2007**, *111*, 11560-11565.

40. L. F. Xu, Y. Guo, Q. Liao, J. P. Zhang, and D. S. Xu, "Morphological control of ZnO nanostructures by electrodeposition" *Journal of Physical Chemistry B* **2005**, *109*, 13519-13522.

41. T. Pauporte, D. Lincot, B. Viana, and F. Pelle, "Toward laser emission of epitaxial nanorod arrays of ZnO grown by electrodeposition" *Applied Physics Letters* **2006**, *89*, 233112.

42. J. H. He, C. H. Ho, C. W. Wang, Y. Ding, L. J. Chen, and Z. L. Wang, "Growth of crossed ZnO nanorod networks induced by polar substrate surface" *Crystal Growth & Design* **2009**, *9*, 17-19.

43. L. L. Yang, Q. X. Zhao, M. Willander, and J. H. Yang, "Effective way to control the size of well-aligned ZnO nanorod arrays with two-step chemical bath deposition" *Journal of Crystal Growth* **2009**, *311*, 1046-1050.

44. Z. R. Dai, Z. W. Pan, and Z. L. Wang, "Novel nanostructures of functional oxides synthesized by thermal evaporation" *Advanced Functional Materials* **2003**, *13*, 9-24.

45. B. D. Yao, Y. F. Chan, and N. Wang, "Formation of ZnO nanostructures by a simple way of thermal evaporation" *Applied Physics Letters* **2002**, *81*, 757-759.

46. C. F. Lin, H. Lin, J. B. Li, and X. Li, "Electrodeposition preparation of ZnO nanobelt array films and application to dye-sensitized solar cells" *Journal of Alloys and Compounds* **2008**, *462*, 175-180.

47. Z. Zhang, S. J. Wang, T. Yu, and T. Wu, "Controlling the growth mechanism of ZnO nanowires by selecting catalysts" *Journal of Physical Chemistry C* **2007**, *111*, 17500-17505.

48. S. C. Lyu, Y. Zhang, H. Ruh, H. J. Lee, H. W. Shim, E. K. Suh, and C. J. Lee, "Low temperature growth and photoluminescence of well-aligned zinc oxide nanowires" *Chemical Physics Letters* **2002**, *363*, 134-138.

49. J. J. Liu, M. H. Yu, and W. L. Zhou, "Well-aligned Mn-doped ZnO nanowires synthesized by a chemical vapor deposition method" *Applied Physics Letters* **2005**, *87*, 172505.

50. P. X. Gao and Z. L. Wang, "Self-assembled nanowire-nanoribbon junction arrays of ZnO" *Journal of Physical Chemistry B* **2002**, *106*, 12653-12658.

51. Y. Qin, R. S. Yang, and Z. L. Wang, "Growth of horizonatal ZnO nanowire arrays on any substrate" *Journal of Physical Chemistry C* **2008**, *112*, 18734-18736.

52. L. S. Wang, X. Z. Zhang, S. Q. Zhao, G. Y. Zhou, Y. L. Zhou, and J. J. Qi, "Synthesis of well-aligned ZnO nanowires by simple physical vapor deposition on c-oriented ZnO thin films without catalysts or additives" *Applied Physics Letters* **2005**, *86*, 024108.

53. W. Lee, M. C. Jeong, and J. M. Myoung, "Catalyst-free growth of ZnO nanowires by metal-organic chemical vapour deposition (MOCVD) and thermal evaporation" *Acta Materialia* **2004**, *52*, 3949-3957.

54. S. Y. Bae, C. W. Na, J. H. Kang, and J. Park, "Comparative structure and optical properties of Ga-, In-, and Sn-doped ZnO nanowires synthesized via thermal evaporation" *Journal of Physical Chemistry B* **2005**, *109*, 2526-2531.

55. H. X. Li, M. X. Xia, G. Z. Dai, H. C. Yu, Q. L. Zhang, A. L. Pan, T. H. Wang, Y. G. Wang, and B. S. Zou, "Growth of oriented zinc oxide nanowire array into novel hierarchical structures in aqueous solutions" *Journal of Physical Chemistry C* **2008**, *112*, 17546-17553.

56. S. Xu, Y. Ding, Y. G. Wei, H. Fang, Y. Shen, A. K. Sood, D. L. Polla, and Z. L. Wang, "Patterned growth of horizontal ZnO nanowire arrays" *Journal of the American Chemical Society* **2009**, *131*, 6670-6671.

57. S. Xu, Y. Wei, M. Kirkham, J. Liu, W. Mai, D. Davidovic, R. L. Snyder, and Z. L. Wang, "Patterned growth of vertically aligned ZnO nanowire arrays on inorganic substrates at low temperature without catalyst" *Journal of the American Chemical Society* **2008**, *130*, 14958-14959.

58. P. X. Gao and Z. L. Wang, "High-yield synthesis of single-crystal nanosprings of ZnO" *Small* **2005**, *1*, 945-949.

59. Y. Ding, X. Y. Kong, and Z. L. Wang, "Doping and planar defects in the formation of single-crystal ZnO nanorings" *Physical Review B* **2004**, *70*, 235408.

60. W. L. Hughes and Z. L. Wang, "Controlled synthesis and manipulation of ZnO nanorings and nanobows" *Applied Physics Letters* **2005**, *86*, 043106.

61. S. H. Mousavi, H. Haratizadeh, and P. W. de Oliveira, "Growth and characterization of wurtzite ZnO nanocombs and nanosaws" *Materials Letters* **2012**, *70*, 86-88.

62. T. F. Xu, P. F. Ji, M. He, and J. Y. Li, "Growth and structure of pure ZnO micro/nanocombs" *Journal of Nanomaterials* **2012**, *2012*, 797935.

63. Y. Yang, B. K. Tay, X. W. Sun, J. Y. Sze, Z. J. Han, J. X. Wang, X. H. Zhang, Y. B. Li, and S. Zhang, "Quenching of surface-exciton emission from ZnO nanocombs by plasma immersion ion implantation" *Applied Physics Letters* **2007**, *91*, 071921.

64. G. Z. Shen, D. Chen, and C. J. Lee, "Hierarchical saw-like ZnO nanobelt/ZnS nanowire heterostructures induced by polar surfaces" *Journal of Physical Chemistry B* **2006**, *110*, 15689-15693.

65. T. Zhai, S. L. Xie, Y. F. Zhao, X. F. Sun, X. H. Lu, M. H. Yu, M. Xu, F. M. Xiao, and Y. X. Tong, "Controllable synthesis of hierarchical ZnO nanodisks for highly photocatalytic activity" *CrystEngComm* **2012**, *14*, 1850-1855.

66. C. K. Xu, K. K. Yang, L. W. Huang, and H. Wang, "Vertically aligned ZnO nanodisks and their uses in bulk heterojunction solar cells" *Journal of Renewable and Sustainable Energy* **2010**, *2*, 053101.

67. C. F. Zhang, F. Zhang, X. W. Sun, Y. Yang, J. Wang, and J. Xu, "Frequency-upconverted whispering-gallery-mode lasing in ZnO hexagonal nanodisks" *Optics Letters* **2009**, *34*, 3349-3351.

68. P. X. Gao and Z. L. Wang, "Nanopropeller arrays of zinc oxide" *Applied Physics Letters* **2004**, *84*, 2883-2885.

69. Y. Zhang, H. B. Jia, X. H. Luo, X. H. Chen, D. P. Yu, and R. M. Wang, "Synthesis, microstructure, and growth mechanism of dendrite ZnO nanowires" *Journal of Physical Chemistry B* **2003**, *107*, 8289-8293.

70. Y. Dai, Y. Zhang, and Z. L. Wang, "The octa-twin tetraleg ZnO nanostructures" *Solid State Communications* **2003**, *126*, 629-633.

71. G. R. Li, C. R. Dawa, Q. Bu, X. H. Lu, Z. H. Ke, H. E. Hong, F. L. Zheng, C. Z. Yao, G. K. Liu, and Y. X. Tong, "Electrochemical self-assembly of ZnO nanoporous structures" *Journal of Physical Chemistry C* **2007**, *111*, 1919-1923.

72. X. D. Wang, J. H. Song, and Z. L. Wang, "Single-crystal nanocastles of ZnO" *Chemical Physics Letters* **2006**, *424*, 86-90.

73. G. Z. Shen, Y. Bando, B. D. Liu, D. Golberg, and C. J. Lee, "Characterization and field-emission properties of vertically aligned ZnO nanonails and nanopencils fabricated by a modified thermal-evaporation process" *Advanced Functional Materials* **2006**, *16*, 410-416.

74. J. Y. Yang, Y. Lin, Y. M. Meng, and Y. H. Liu, "A two-step route to synthesize highly oriented ZnO nanotube arrays" *Ceramics International* **2012**, *38*, 4555-4559.

75. Z. F. Deng, Q. Rui, X. Yin, H. Q. Liu, and Y. Tian, "In vivo detection of superoxide anion in bean sprout based on ZnO nanodisks with facilitated activity for direct electron transfer of superoxide dismutase" *Analytical Chemistry* **2008**, *80*, 5839-5846.

76. K. Keem, H. Kim, G. T. Kim, J. S. Lee, B. Min, K. Cho, M. Y. Sung, and S. Kim, "Photocurrent in ZnO nanowires grown from Au electrodes" *Applied Physics Letters* **2004**, *84*, 4376-4378.

77. O. Harnack, C. Pacholski, H. Weller, A. Yasuda, and J. M. Wessels, "Rectifying behavior of electrically aligned ZnO nanorods" *Nano Letters* **2003**, *3*, 1097-1101.

78. H. Kind, H. Q. Yan, B. Messer, M. Law, and P. D. Yang, "Nanowire ultraviolet photodetectors and optical switches" *Advanced Materials* **2002**, *14*, 158-160.

79. H. Ohta, M. Kamiya, T. Kamaiya, M. Hirano, and H. Hosono, "UV-detector based on pn-heteroj unction diode composed of transparent oxide semiconductors, p-NiO/n-ZnO" *Thin Solid Films* **2003**, *445*, 317-321.

80. S. E. Ahn, J. S. Lee, H. Kim, S. Kim, B. H. Kang, K. H. Kim, and G. T. Kim, "Photoresponse of sol-gel-synthesized ZnO nanorods" *Applied Physics Letters* **2004**, *84*, 5022-5024.

81. Q. Wan, Q. H. Li, Y. J. Chen, T. H. Wang, X. L. He, X. G. Gao, and J. P. Li, "Positive temperature coefficient resistance and humidity sensing properties of Cd-doped ZnO nanowires" *Applied Physics Letters* **2004**, *84*, 3085-3087.

82. Q. H. Li, Q. Wan, Y. X. Liang, and T. H. Wang, "Electronic transport through individual ZnO nanowires" *Applied Physics Letters* **2004**, *84*, 4556-4558.

83. M. S. Arnold, P. Avouris, Z. W. Pan, and Z. L. Wang, "Field-effect transistors based on single semiconducting oxide nanobelts" *Journal of Physical Chemistry B* **2003**, *107*, 659-663.

84. C. H. Liu, W. C. Yiu, F. C. K. Au, J. X. Ding, C. S. Lee, and S. T. Lee, "Electrical properties of zinc oxide nanowires and intramolecular p-n junctions" *Applied Physics Letters* **2003**, *83*, 3168-3170.

85. W. I. Park, G. C. Yi, J. W. Kim, and S. M. Park, "Schottky nanocontacts on ZnO nanorod arrays" *Applied Physics Letters* **2003**, *82*, 4358-4360.

86. W. I. Park and G. C. Yi, "Electroluminescence in n-ZnO nanorod arrays vertically grown on p-GaN" *Advanced Materials* **2004**, *16*, 87-90.

87. G. Stan, C. V. Ciobanu, P. M. Parthangal, and R. F. Cook, "Diameter-dependent radial and tangential elastic moduli of ZnO nanowires" *Nano Letters* **2007**, *7*, 3691-3697.

88. M. H. Zhao, C. B. Jiang, S. X. Li, and S. X. Mao, "Probing nano-scale mechanical characteristics of individual semi-conducting nanobelts" *Materials Science and Engineering A-Structural Materials Properties Microstructure and Processing* **2005**, *409*, 223-226.

89. H. Ni and X. D. Li, "Young's modulus of ZnO nanobelts measured using atomic force microscopy and nanoindentation techniques" *Nanotechnology* **2006**, *17*, 3591-3597.

90. W. J. Mai and Z. L. Wang, "Quantifying the elastic deformation behavior of bridged nanobelts" *Applied Physics Letters* **2006**, *89*, 073112.

91. A. J. Kulkarni, M. Zhou, and F. J. Ke, "Orientation and size dependence of the elastic properties of zinc oxide nanobelts" *Nanotechnology* **2005**, *16*, 2749-2756.

92. L. X. Zhang and H. C. Huang, "Young's moduli of ZnO nanoplates: ab initio determinations" *Applied Physics Letters* **2006**, *89*, 183111.

93. C. Q. Chen, Y. Shi, Y. S. Zhang, J. Zhu, and Y. J. Yan, "Size dependence of Young's modulus in ZnO nanowires" *Physical Review Letters* **2006**, *96*, 075505.

94. M. H. Zhao, Z. Z. Ye, and S. X. Mao, "Photoinduced stiffening in ZnO nanobelts" *Physical Review Letters* **2009**, *102*, 045502.

95. J. F. Zang, L. H. Bao, R. A. Webb, and X. D. Li, "Electron beam irradiation stiffens zinc tin oxide nanowires" *Nano Letters* **2011**, *11*, 4885-4889.

96. J. F. Zang, Z. H. Xu, R. A. Webb, and X. D. Li, "Electrical self-healing of mechanically damaged zinc oxide nanobelts" *Nano Letters* **2011**, *11*, 241-244.

97. Y. C. Yang, G. F. Wang, and X. D. Li, "Water molecule-induced stiffening in ZnO nanobelts" *Nano Letters* **2012**, *11*, 2845-2848.

98. P. Puri and V. Yang, "Effect of particle size on melting of aluminum at nano scales" *Journal of Physical Chemistry C* **2007**, *111*, 11776-11783.

99. J. Eckert, J. C. Holzer, C. E. Krill, and W. L. Johnson, "Structural and thermodynamic properties of nanocrystalline FCC metals prepared by mechanical attrition" *Journal of Materials Research* **1992**, *7*, 1751-1761.

100. S. Alavi and D. L. Thompson, "Molecular dynamics simulations of the melting of aluminum nanoparticles" *Journal of Physical Chemistry A* **2006**, *110*, 1518-1523.

101. Y. Y. Wu and P. D. Yang, "Melting and welding semiconductor nanowires in nanotubes" *Advanced Materials* **2001**, *13*, 520-523.

102. L. Hui, B. L. Wang, J. L. Wang, and G. H. Wang, "Melting behavior of one-dimensional zirconium nanowire" *Journal of Chemical Physics* **2004**, *120*, 3431-3438.

103. C. Y. Pan, Z. J. Zhang, X. Su, Y. Zhao, and J. G. Liu, "Characterization of Fe nanorods grown directly from submicron-sized iron grains by thermal evaporation" *Physical Review B* **2004**, *70*, 233404.

104. D. Xie, M. P. Wang, and W. H. Qi, "A simplified model to calculate the surface-to-volume atomic ratio dependent cohesive energy of nanocrystals" *Journal of Physics-Condensed Matter* **2004**, *16*, L401-L405.

105. W. H. Qi, M. P. Wang, and G. Y. Xu, "The particle size dependence of cohesive energy of metallic nanoparticles" *Chemical Physics Letters* **2003**, *372*, 632-634.

106. W. H. Qi, M. P. Wang, and W. Y. Hu, "Calculation of the cohesive energy of metallic nanoparticles by the Lennard-Jones potential" *Materials Letters* **2004**, *58*, 1745-1749.

107. C. R. M. Wronski, "Size dependence of melting point of small particles of tin" *British Journal of Applied Physics* **1967**, *18*, 1731-1737.

108. G. Guisbiers and S. Pereira, "Theoretical investigation of size and shape effects on the melting temperature of ZnO nanostructures" *Nanotechnology* **2007**, *18*, 1-6.

109. C. C. Su and J. L. Chen, "Effects of geometric structure, orientation and size on structural stability and thermal behavior of zinc oxide nanowires" *Materials Research Bulletin* **2011**, *46*, 1686-1691.

110. M. Sano, A. Kamino, J. Okamura, and S. Shinkai, "Self-organization of PEO-graft-single-walled carbon nanotubes in solutions and Langmuir-Blodgett films" *Langmuir* **2001**, *17*, 5125-5128.

111. M. F. Islam, E. Rojas, D. M. Bergey, A. T. Johnson, and A. G. Yodh, "High weight fraction surfactant solubilization of single-wall carbon nanotubes in water" *Nano Letters* **2003**, *3*, 269-273.

112. J. A. Fagan, B. J. Landi, I. Mandelbaum, J. R. Simpson, V. Bajpai, B. J. Bauer, K. Migler, A. R. H. Walker, R. Raffaelle, and E. K. Hobbie, "Comparative measures of single-wall carbon nanotube dispersion" *Journal of Physical Chemistry B* **2006**, *110*, 23801-23805.

113. M. Zheng, A. Jagota, E. D. Semke, B. A. Diner, R. S. McLean, S. R. Lustig, R. E. Richardson, and N. G. Tassi, "DNA-assisted dispersion and separation of carbon nanotubes" *Nature Materials* **2003**, *2*, 338-342.

114. A. Stesmans, "Passivation of P-b0 and P-b1 interface defects in thermal (100) Si/SiO2 with molecular hydrogen" *Applied Physics Letters* **1996**, *68*, 2076-2078.

115. X. S. Zhou, T. B. Wu, K. L. Ding, B. J. Hu, M. Q. Hou, and B. X. Han, "Dispersion of graphene sheets in ionic liquid [bmim][PF6] stabilized by an ionic liquid polymer" *Chemical Communications* **2010**, *46*, 386-388.

116. D. Li, M. B. Muller, S. Gilje, R. B. Kaner, and G. G. Wallace, "Processable aqueous dispersions of graphene nanosheets" *Nature Nanotechnology* **2008**, *3*, 101-105.

117. M. Fang, K. G. Wang, H. B. Lu, Y. L. Yang, and S. Nutt, "Covalent polymer functionalization of graphene nanosheets and mechanical properties of composites" *Journal of Materials Chemistry* **2009**, *19*, 7098-7105.

118. S. C. Tjong, "Polymer nanocomposite bipolar plates reinforced with carbon nanotubes and graphite nanosheets" *Energy & Environmental Science* **2011**, *4*, 605-626.

119. K. M. F. Shahil and A. A. Balandin, "Graphene-multilayer graphene nanocomposites as highly efficient thermal interface materials" *Nano Letters* **2012**, *12*, 861-867.

120. T. Ramanathan, A. A. Abdala, S. Stankovich, D. A. Dikin, M. Herrera-Alonso, R. D. Piner, D. H. Adamson, H. C. Schniepp, X. Chen, R. S. Ruoff, S. T. Nguyen, I. A. Aksay, R. K. Prud'homme, and L. C. Brinson, "Functionalized graphene sheets for polymer nanocomposites" *Nature Nanotechnology* **2008**, *3*, 327-331.

121. T. Tsuji and K. Yamanaka, "Observation by ultrasonic atomic force microscopy of reversible displacement of subsurface dislocations in highly oriented pyrolytic graphite" *Nanotechnology* **2001**, *12*, 301-307.

122. A. J. Patil, J. L. Vickery, T. B. Scott, and S. Mann, "Aqueous stabilization and self-assembly of graphene sheets into layered bio-nanocomposites using DNA" *Advanced Materials* **2009**, *21*, 3159-3164.

123. X. Y. Zhang, A. C. Coleman, N. Katsonis, W. R. Browne, B. J. van Wees, and B. L. Feringa, "Dispersion of graphene in ethanol using a simple solvent exchange method" *Chemical Communications* **2010**, *46*, 7539-7541.

124. D. W. Boukhvalov and M. I. Katsnelson, "Chemical functionalization of graphene with defects" *Nano Letters* **2008**, *8*, 4373-4379.

125. Y. Si and E. T. Samulski, "Synthesis of water soluble graphene" *Nano Letters* **2008**, *8*, 1679-1682.

126. N. V. Medhekar, A. Ramasubramaniam, R. S. Ruoff, and V. B. Shenoy, "Hydrogen bond networks in graphene oxide composite paper: structure and mechanical properties" *ACS Nano* **2010**, *4*, 2300-2306.

127. H. Kim, A. A. Abdala, and C. W. Macosko, "Graphene/polymer nanocomposites" *Macromolecules* **2010**, *43*, 6515-6530.

128. J. Q. Broughton, C. A. Meli, P. Vashishta, and R. K. Kalia, "Direct atomistic simulation of quartz crystal oscillators: Bulk properties and nanoscale devices" *Physical Review B* **1997**, *56*, 611-618.

129. R. E. Miller and V. B. Shenoy, "Size-dependent elastic properties of nanosized structural elements" *Nanotechnology* **2000**, *11*, 139-147.

130. V. B. Shenoy, "Atomistic calculations of elastic properties of metallic fcc crystal surfaces" *Physical Review B* **2005**, *71*, 094104.

131. Y. Yan and M. M. Al-Jassim, "Structure and energetics of water adsorbed on the $ZnO\,(10\bar{1}0)$ surface" *Physical Review B* **2005**, *72*, 235406.

132. B. Meyer, H. Rabaa, and D. Marx, "Water adsorption on $ZnO\,(10\bar{1}0)$: from single molecules to partially dissociated monolayers" *Physical Chemistry Chemical Physics* **2006**, *8*, 1513-1520.

133. G. Kresse and J. Hafner, "Abinitio molecular-dynamics for liquid-metals" *Physical Review B* **1993**, *47*, 558-561.

134. G. Kresse and J. Furthmuller, "Efficient iterative schemes for ab initio total-energy calculations using a plane-wave basis set" *Physical Review B* **1996**, *54*, 11169-11186.

135. G. Kresse and D. Joubert, "From ultrasoft pseudopotentials to the projector augmented-wave method" *Physical Review B* **1999**, *59*, 1758-1775.

136. J. P. Perdew and Y. Wang, "Accurate and simple analytic representation of the electron-gas correlation-energy" *Physical Review B* **1992**, *45*, 13244-13249.

137. C. B. Duke, R. J. Meyer, A. Paton, and P. Mark, "Calculation of low-energy-electron-diffraction intensities from ZnO ($10\bar{1}0$) . II. Influence of calculational procedure, model potential and 2nd-layer structural distortions" *Physical Review B* **1978**, *18*, 4225-4240.

138. G. F. Wang and X. D. Li, "Size dependency of the elastic modulus of ZnO nanowires: Surface stress effect" *Applied Physics Letters* **2007**, *91*, 231912.

139. Y. Cui, Q. Q. Wei, H. K. Park, and C. M. Lieber, "Nanowire nanosensors for highly sensitive and selective detection of biological and chemical species" *Science* **2001**, *293*, 1289-1292.

140. M. D. Stoller, S. J. Park, Y. W. Zhu, J. H. An, and R. S. Ruoff, "Graphene-based ultracapacitors" *Nano Letters* **2008**, *8*, 3498-3502.

141. G. Guisbiers, M. Kazan, O. Van Overschelde, M. Wautelet, and S. Pereira, "Mechanical and thermal properties of metallic and semiconductive nanostructures" *Journal of Physical Chemistry C* **2008**, *112*, 4097-4103.

142. J. W. L. Yim, B. Xiang, and J. Q. Wu, "Sublimation of GeTe nanowires and evidence of its size effect studied by in situ TEM" *Journal of the American Chemical Society* **2009**, *131*, 14526-14530.

143. Y. Sato, T. Hirayama, and Y. Ikuhara, "Real-time direct observations of polarization reversal in a piezoelectric crystal: $Pb(Mg_{1/3}Nb_{2/3})O_3$-$PbTiO_3$ studied via *in situ* electrical biasing transmission electron microscopy" *Physical Review Letters* **2011**, *107*, 187601.

144. S. M. Chen, K. Kobayashi, Y. Miyata, N. Imazu, T. Saito, R. Kitaura, and H. Shinohara, "Morphology and melting behavior of ionic liquids inside single-walled carbon nanotubes" *Journal of the American Chemical Society* **2009**, *131*, 14850-14856.

145. S. Panda, Microelectronics and Optoelectronics Technology, University Science Press **2009**, P56.

146.   Q. Zhang, J. J. Qi, X. Li, and Y. Zhang, "Diameter-dependent internal gain in ZnO micro/nanowires under electron beam irradiation" *Nanoscale* **2011**, *3*, 3060-3063.

147.   C. Jagadish and S. Pearton, Zinc Oxide Bulk, Thin Films and Nanostructures: Processing, Properties, and Applications, Elsevier Ltd. **2006**, P12.

148.   M. A. Shandiz, "Effective coordination number model for the size dependency of physical properties of nanocrystals" *Journal of Physics: Condensed Matter* **2008**, *20*, 325237.

149.   H. J. Dai, J. H. Hafner, A. G. Rinzler, D. T. Colbert, and R. E. Smalley, "Nanotubes as nanoprobes in scanning probe microscopy" *Nature* **1996**, *384*, 147-150.

150.   H. Sugie, M. Tanemura, V. Filip, K. Iwata, K. Takahashi, and F. Okuyama, "Carbon nanotubes as electron source in an x-ray tube" *Applied Physics Letters* **2001**, *78*, 2578-2580.

151.   C. Liu, Y. Y. Fan, M. Liu, H. T. Cong, H. M. Cheng, and M. S. Dresselhaus, "Hydrogen storage in single-walled carbon nanotubes at room temperature" *Science* **1999**, *286*, 1127-1129.

152.   E. Frackowiak and F. Béguin, "Electrochemical storage of energy in carbon nanotubes and nanostructured carbons" *Carbon* **2002**, *40*, 1775-1787.

153.   S. J. Tans, M. H. Devoret, R. J. A. Groeneveld, and C. Dekker, "Electron-electron correlations in carbon nanotubes" *Nature* **1998**, *394*, 761-764.

154.   J. Wang, M. Musameh, and Y. Lin, "Solubilization of carbon nanotubes by nafion toward the preparation of amperometric biosensors" *Journal of the American Chemical Society* **2003**, *125*, 2408-2409.

155.   L. Vaisman, H. D. Wagner, and G. Marom, "The role of surfactants in dispersion of carbon nanotubes" *Advances in Colloid and Interface Science*, **2006**, *128*, 37-46.

156.   J. Hedberg, L. F. Dong, and J. Jiao, "Air flow technique for large scale dispersion and alignment of carbon nanotubes on various substrate" *Applied Physics Letters* **2005**, *86*, 143111.

157.   M. G. C. Kahn, S. Banerjee, and S. S. Wong, "Solubilization of oxidized single-walled carbon nanotubes in organic and aqueous solvents through organic derivatization" *Nano Letters* **2002**, *2*, 1215-1218.

158.   F. Pompeo and D. E. Resasco, "Water solubilization of single-walled carbon nanotubes by functionalization with glucosamine" *Nano Letters* **2002**, *2*, 369-373.

159.   M. F. Islam, E. Rojas, D. M. Bergey, A. T. Johnson, and A. G. Yodh, "High weight fraction surfactant solubilization of single-walled carbon nanotubes in water" *Nano Letters* **2003**, *3*, 269-273.

160.   M. Zhang, A. Jagota, E. D. Semke, B. A. Diner, R. S. Mclean, S. R. Lustig, R. E. Richardson, and N. G. Tassi, "DNA-assisted dispersion and separation of carbon nanotubes" *Nature Materials* **2003**, *2*, 338-342.

161.   M. M. Atalla, E. Tannenbaum, and E. J. Scheibner, "Stabilization of silicon surfaces by thermally grown oxides" *Bell System Technical Journal* **1959**, *38*, 749-783.

162.   E. H. Nicollian, "Surface passivation of semiconductors" *Journal of Vacuum Science and Technology* **1971**, *8*, S39-S49.

163.   J. R. Weber, A. Janotti, P. Rinke, and C. G. van de Walle, "Dangling-bond defects and hydrogen passivation in germanium" *Applied Physics Letters* **2007**, *91*, 142101.

164.   A. Nieto-Márquez, R. Romero, A. Romero, and J. L. Valverde, "Carbon nanospheres: synthesis, physicochemical properties and applications" *Journal of Materials Chemistry* **2011**, *21*, 1664-1672.

165.   F. Messina and M. Cannas, "Character of the reaction between molecular hydrogen and a silicon dangling bond in amorphous SiO_2" *Journal of Chemical Physics C* **2007**, *111*, 6663-6667.

166.   Z. W. Pan, S. S. Xie, B. H. Chang, C. Y. Wang, L. Lu, W. Liu, M. Y. Zhou, and W. Z. Li, "Very long carbon nanotubes" *Nature* **1998**, *394*, 631-632.

167.   Z. J. Gu, Y. C. Yang, K. Y. Li, X. Y. Tao, G. Eres, J. Y. Howe, L. T. Zhang, X. D. Li, and Z. W. Pan, "Aligned carbon nanotube-reinforced silicon carbide composites produced by chemical vapor infiltration" *Carbon* **2011**, *49*, 2475-2482.

168.   E. Harder, J. D. Eaves, A. Tokmakoff, and B. J. Berne, "Polarizable molecules in the vibrational spectroscopy of water" *Proceedings of the National Academy of Sciences of the United States of America* **2005**, *120*, 11611-11616.

169.   S. Paul and A. Chandra, "Hydrogen bond properties and dynamics of liquid-vapor interfaces methanol solutions" *Journal of Chemical Theory and Computation* **2005**, *1*, 1221-1231.

170.   T. I. T. Okpalugo, P. Papakonstantinou, H. Murphy, J. McLaughlin, and N. M. D. Brown, "High resolution XPS characterization of chemical functionalised MWCNTs and SWCNTs" *Carbon* **2005**, *43*, 153-161.

171.   A. Nikitin, H. Ogasawara, D. Mann, R. Denecke, Z. Zhang, H. Dai, K. Cho, and A. Nilsson, "Hydrogenation of single-walled carbon nanotubes" *Physical Review Letters* **2005**, *95*, 225507.

172.   J. S. Arellano, L. M. Molina, A. Rubio, M. J. Lopez, and J. A. Alonso, "Interaction of molecular and atomic hydrogen with (5,5) and (6,6) single-wall carbon nanotubes" *Journal of Chemical Physics* **2002**, *117*, 2281-2288.

173.   Y. Wang, J. Wu, and F. Wei, "A treatment method to give separated multi-walled carbon nanotubes with high purity, high crystallization and a large aspect ratio" *Carbon* **2003**, *41*, 2939-2948.

174.   H. D. Wagner, O. Lourie, Y. Feldman, and R. Tenne, "Stress-induced fragmentation of multiwall carbon nanotubes in a polymer matrix" *Applied Physics Letters* **1998**, *72*, 188-190.

175.   E. T. Thostenson, W. Z. Li, D. Z. Wang, Z. F. Ren, and T. W. Chou, "Carbon nanotube/carbon fiber hybrid multiscale composites" *Journal of Applied Physics* **2002**, *91*, 6034-6037.

176.   D. T. Morelli, J. P. Heremans, and G. A. Slack, "Estimation of the isotope effect on the lattice thermal conductivity of group IV and group III-V semiconductors" *Physics Review B* **2002**, *66*, 195304.

177.   K. Igamberdiev, S. Yuldashev, H. D. Cho, T. W. Kang, and A. Shashkov, "Thermal conductivity of ZnO nanowires embedded in poly(methyl methacrylate) matrix" *Applied Physics Express* **2011**, *4*, 015001.

178.   S. L. Ruan, P. Gao, X. G. Yang, and T. X. Yu, "Toughening high performance ultrahigh molecular weight polyethylene using multiwalled carbon nanotubes" *Polymer* **2003**, *44*, 5643-5654.

179.   X. D. Li, H. S. Gao, W. A. Scrivens, D. L. Fei, X. Y. Xu, M. A. Sutton, A. P. Reynolds, and M. L. Myrick, "Nanomechanical characterization of single-walled carbon nanotube reinforced epoxy composites" *Nanotechnology* **2004**, *15*, 1416-1423.

180.   X. Y. Gong, J. Liu, S. Baskaran, R. D. Voise, and J. S. Young, "Surfactant-assisted processing of carbon nanotube/polymer composites" *Chemistry of Materials* **2000**, *12*, 1049-1052.

181.   F. N. Xia, T. Mueller, Y. M. Lin, A. Valdes-Garcia, and P. Avouris, "Ultrafast graphene photodetector" *Nature Nanotechnology* **2009**, *4*, 839-843.

182.   A. K. Geim and K. S. Novoselov, "The rise of graphene" *Nature Materials* **2007**, *6*, 183-191.

183.   I. Meric, M. Y. Han, A. F. Young, B. Ozyilmaz, P. Kim, and K. L. Shepard, "Current saturation in zero-bandgap, top-gated graphene field-effect transistors" *Nature Nanotechnology* **2008**, *3*, 654-659.

184.   A. A. Balandin, S. Ghoshy, W. Z. Bao, I. Calizo, D. Teweldebrhan, F. Miao, and C. N. Lau, "Superior thermal conductivity of single-layer graphene" *Nano Letters* **2008**, *8*, 902-907.

185.   X. Huang, X. Y. Qi, F. Boey, and H. Zhang, "Graphene-based composites" *Chemical Society Reviews* **2012**, *41*, 666-686.

186.   C. G. Lee, X. D. Wei, J. W. Kysar, and J. Hone, "Measurement of the elastic properties and intrinsic strength of monolayer graphene" *Science* **2008**, *321*, 385-388.

187.   S. Stankovich, D. A. Dikin, G. H. B. Dommett, K. M. Kohlhaas, E. J. Zimney, E. A. Stach, R. D. Piner, S. T. Nguyen, and R. S. Ruoff, "Graphene-based composite materials" *Nature* **2006**, *442*, 282-286.

188.   N. Chawla and X. Deng, "Microstructure and mechanical behavior of porous sintered steels" *Materials Science and Engineering A* **2005**, *390*, 98-112.

189.   W. Choi and J. W. Lee, *"Graphene: Synthesis and Applications"* CRC Press. Boca Raton, FL. **2012**, P37.

190.   Y. C. Si and E. T. Samulski, "Synthesis of water soluble graphene" *Nano Letters* **2008**, *8*, 1679-1682.

191.   J. Lu, J. X. Yang, J. Z. Wang, A. Lim, S. Wang, and K. P. Loh, "One-pot synthesis of fluorescent carbon nanoribbons, nanoparticles, and graphene by the exfoliation of graphene in ionic liquids" *ACS Nano* **2009**, *3*, 2367-2375.

192.   X. H. An, T. Simmons, R. Shah, C. Wolfe, K. M. Lewis, M. Washington, S. K. Nayak, S. Talapatra, and S. Kar, "Stable aqueous dispersions of noncovalently functionalized graphene from graphite and their multifunctional high-performance applications" *Nano Letters* **2010**, *10*, 4295-4301.

193.   Y. C. Yang, Z. H. Xu, Z. W. Pan, and X. D. Li, "Hydrogen passivation induced dispersion of multi-walled carbon nanotubes" *Advanced Materials* **2012**, *24*, 881-885.

194.   M. A. Akhukov, A. Fasolino, Y. N. Gornostyrev, and M. I. Katsnelson, "Dangling bonds and magnetism of grain boundaries in graphene" *Physical Review B* **2012**, *85*, 115407.

195.   L. L. Song, X. H. Zheng, R. L. Wang, and Z. Zeng, "Dangling bond states, edge magnetism, and edge reconstruction in pristine and B/N-terminated zigzag graphene nanoribbons" *Journal of Physical Chemistry C* **2010**, *114*, 12145-12150.

196. H. Wang, Y. F. Wang, X. W. Cao, M. Feng, and G. X. Lan, "Vibrational properties of graphene and graphene layers" *Journal of Raman Spectroscopy* **2009**, *40*, 1791-1796.

197. A. C. Ferrari, J. C. Meyer, V. Scardaci, C. Casiraghi, M. Lazzeri, F. Mauri, S. Piscanec, D. Jiang, K. S. Novoselov, S. Roth, and A. K. Geim, "Raman spectrum of graphene and graphene layers" *Physical Review Letters* **2006**, *97*, 187401.

198. Z. H. Ni, H. M. Wang, J. Kasim, H. M. Fan, T. Yu, Y. H. Wu, Y. P. Feng, and Z. X. Shen, "Graphene thickness determination using reflection and contrast spectroscopy" *Nano Letters* **2007**, *7*, 2758-2763.

199. W. C. Oliver and G. M. Pharr, "An improved technique for determining hardness and elastic modulus using load and displacement sensing indentation experiments" *Journal of Materials Research* **1992**, *7*, 1564-1583.

200. J. Liang, L. Zhang, Y. Wang, Y. Ma, T. Guo, and Y. Chen, "Molecular-level dispersion of graphene into poly(vinyl alcohol) and effective reinforcement of their nanocomposites" *Advanced. Functional Materials* **2009**, *19*, 2297-2302.

201. J. A. King, D. R. Klimek, I. Miskioglu, and G. M. Odegard, "Mechanical properties of graphene nanoplatelet/epoxy composites" *Journal of Applied. Polymer Science* **2013**, *128*, 4217-4223.

202. W. E. Mahmoud, "Morphology and physical properties of poly(ethylene oxide) loaded graphene nanocomposites prepared by two different techniques" *European Polymer Journal* **2011**, *47*, 1534-1540.

203. J. C. Halpin, and J. L. Kardos, "Halpin-Tsai equations-review" *Polymer Engineering and Science* **1976**, *16*, 344-352.

204. B. Das, K. E. Prasad, U. Ramamurty, and C. N. R. Rao, "Nano-indentation studies on polymer matrix composites reinforced by few-layer graphene" *Nanotechnology* **2009**, *20*, 125705.

205. A. Yasmin, J. J. Luo, and I. M. Daniel, "Processing of expanded graphite reinforced polymer nanocomposites" *Composite Science and Technology* **2006**, *66*, 1182-1189.

206. T. Kuillaa, S. Bhadrab, D. Yaoa, N. H. Kimc, S. Bosed, and J. H. Lee, "Recent advances in graphene based polymer composites" *Progress in Polymer Science* **2010**, *35*, 1350-1375.

207. S. Vadukumpully, J. Paul, N. Mahanta, and S. Valiyaveettil, "Flexible conductive graphene/poly(vinyl chloride) composite thin films with high mechanical strength and thermal stability" *Carbon* **2011**, *49*, 198-205.

208.   X. L. Wang, H. Bai, Z. Y. Yao, A. R. Liu, and G. Q. Shi, "Electrically conductive and mechanically strong biomimetic chitosan/reduced graphene oxide composite films" *Journal of Materials Chemistry* **2010**, *20*, 9032-9036.

209.   S. Sundararajan, B. Bhushan, T. Namazu, and Y. Isono, "Mechanical property measurements of nanoscale structures using an atomic force microscope" *Ultramicroscopy* **2002**, *91*, 111-118.

210.   M. A. Rafiee, J. Rafiee, I. Srivastava, Z. Wang, H. Song, Z. Z. Yu, and N. Koratkar, "Fracture and fatigue in graphene nanocomposites" *Small* **2010**, *6*, 179-183.

211.   J. Cho, A. R. Boccaccini, and M. S. P. Shaffer, "Ceramic matrix composites containing carbon nanotubes" *Journal of Materials Science* **2009**, *44*, 1934-1951.

212.   R. Z. Ma, J. Wu, B. Q. Wei, J. Liang, and D. H. Wu, "Processing and properties of carbon nanotubes-nano-SiC ceramic" *Journal of Materials Science* **1998**, *33*, 5243-5246.

213.   G. D. Zhan, J. D. Kuntz, J. L. Wan, and A. K. Mukherjee, "Single-wall carbon nanotubes as attractive toughening agents in alumina-based nanocomposites" *Nature Materials* **2003**, *2*, 38-42.

214.   A. Peigney, "Composite materials: Tougher ceramics with nanotubes" *Nature Materials* **2003**, *2*, 15-16.

215.   X. T. Wang, N. P. Padture, and H. Tanaka, "Contact-damage-resistant ceramic/single-wall carbon nanotubes and ceramic/graphite composites" *Nature Materials* **2004**, *3*, 539-544.

216.   B. W. Sheldon and W. A. Curtin, "Nanoceramic composites: Tough to test" *Nature Materials* **2004**, *3*, 505-506.

217.   C. Balázsi, B. Fényi, N. Hegman, Z. Kövér, F. Wéber, Z. Vértesy, Z. Kónya, I. Kiricsi, L. P. Biró, and P. Arató, "Development of CNT/Si_3N_4 composites with improved mechanical and electrical properties" *Composites Part B: Engineering* **2006**, *37*, 418-424.

218.   S. Q. Guo, R. Sivakumar, H. Kitazawa, and Y. Kagawa, "Electrical properties of Silica-based nanocomposites with multiwall carbon nanotubes" *Journal of American Ceramic Society* **2007**, *90*, 1667-1670.

219.   P. M. Ajayan and J. M. Tour, "Materials science-Nanotube composites" *Nature* **2007**, *447*, 1066-1068.

220.   H. G. Chae and S. Kumar, "Materials science-Making strong fibers" *Science* **2008**, *319*, 908-909.

221. R. Naslain, "Design, preparation and properties of non-oxide CMCs for application in engines and nuclear reactors: an overview" *Composites Science and Technology* **2004**, *64*, 155-170.

222. T. M. Besmann, B. W. Sheldon, R. A. Lowden, and D. P. Stinton, "Vapor-phase fabrication and properties of continuous-filament ceramic composites" *Science* **1991**, *253*, 1104-1109.

223. F. Lamouroux, G. Camus, and J. Thebault, "Kinetics and mechanisms of oxidation of 2D woven C/SiC composites. 1. Experimental approach" *Journal of American Ceramic Society* **1994**, *77*, 2049-2057.

224. Y. D. Xu, L. T. Zhang, L. F. Cheng, and D. T. Yan, "Microstructure and mechanical properties of three-dimensional carbon/silicon carbide composites fabricated by chemical vapor infiltration" *Carbon* **1998**, *36*, 1051-1056.

225. G. Eres, A. A. Puretzky, D. B. Geohegan, and H. Cui. "In situ control of the catalyst efficiency in chemical vapor deposition of vertically aligned carbon nanotubes on predeposited metal catalyst films" *Applied Physics Letters* **2004**, *84*, 1759-1761.

226. D. P. Stinton, D. M. Hembree, K. L. More, B. W. Sheldon, T. M. Besmann, M. H. Headinger, and R. F. Davis, "Matrix characterization of fiber-reinforced SiC matrix composites fabricated by chemical-vapor infiltration" *Journal of Materials Science* **1995**, *30*, 4279-4285.

227. H. Araki, T. Noda, F. Abe, and H. Suzuki, "Interfacial structural of chemical vapor infiltration carbon fiber/SiC composite" *Journal of Materials Science Letters* **1992**, *11*, 1582-1584.

228. J. C. Charlier and J. P. Michenaud, "Energetics of multilayered carbon tubules" *Physics Review Letters* **1993**, *70*, 1858-1861.

229. A. N. Kolmogorov and V. H. Crespi, "Smoothest bearings: Interlayer sliding in multiwalled carbon nanotubes" *Physics Review Letters* **2000**, *85*, 4727-4730.

230. M. F. Yu, O. Lourie, M. J. Dyer, K. Moloni, T. F. Kelly, and R. S. Ruoff, "Strength and breaking mechanism of multiwalled carbon nanotubes under tensile load" *Science* **2000**, *287*, 637-640.

231. J. Cumings and A. Zettl, "Low-friction nanoscale linear bearing realized from multiwall carbon nanotubes" *Science* **2000**, *289*, 602-604.

232. A. Kis, K. Jensen, S. Aloni, W. Mickelson, and A. Zettl, "Interlayer forces and ultralow sliding friction in multiwalled carbon nanotubes" *Physics Review Letters* **2006**, *97*, 025501.

233.	P. Baldus, M. Jansen, and D. Sporn, "Ceramic fibers for matrix composites in high-temperature engine applications" *Science* **1999**, *285*, 699-703.

234.	L. Filipuzzi, G. Camus, R. Naslain, and R. J. Thebault, "Oxidation mechanisms and kinetics of 1D-SiC/C/SiC composite-materials. 1. An experimental approach" *Journal of American Ceramic Society* **1994**, *77*, 459-466.

235.	H. Ni, X. D. Li, and H. S. Gao, "Elastic modulus of amorphous SiO_2 nanowires" *Applied Physics Letters* **2006**, *88*, 043108.

236.	Q. H. Xiong, N. Duarte, S. Tadigadapa, and P. C. Eklund, "Force-deflection spectroscopy: A new method to determine the Young's modulus of nanofilaments" *Nano Letters* **2006**, *6*, 1904-1909.

237.	M. T. Kim and J. Lee, "Characterization of amorphous SiC:H films deposited from hexamethyldisilazane" *Thin Solid Films* **1997**, *303*, 173-179.

238.	N. H. MacMillan, "Theoretical strength of solids" *Journal of Materials Science* **1972**, *7*, 239.

239.	Y. W. Kim, K. Ando, and M. C. Chu, "Crack-healing behavior of liquid-phase-sintered silicon carbide ceramics" *Journal of American Ceramic Society* **2003**, *86*, 465-470.

240.	N. Matsunaga, K. Nakahama, Y. Hirata, and S. Sameshima, "Enhancement of strength of SiC by heat-treatment in air" *Journal of Ceramics Processing Research* **2009**, *10*, 319-324.

241.	M. Zhang, S. L. Fang, A. A. Zakhidov, S. B. Lee, A. E. Aliev, C. D. Williams, K. R. Atkinson, and R. H. Baughman, "Strong, transparent, multifunctional carbon nanotube sheets" *Science* **2005**, *309*, 1215-1219.

242.	M. Zhang, K. R. Atkinson, and R. H. Baughman, "Multifunctional carbon nanotube yarns by downsizing an ancient technology" *Science* **2004**, *306*, 1358-1361.